Mesures ultrasonores et de transport dans le semimétal de Weyl NbP

par

Marianne Ward

Mémoire présenté au Département de physique en vue de l'obtention du grade de maître ès sciences (M.Sc.)

FACULTÉ DES SCIENCES

UNIVERSITÉ DE SHERBROOKE

Sherbrooke, Québec, Canada, [avril 2023]

Ultrasound and Transport Measurements in the Weyl Semimetal NbP

by

Marianne Ward

Thesis presented to the Department of Physics for the degree of Master of Science (M.Sc.)

FACULTY OF SCIENCE

UNIVERSITÉ DE SHERBROOKE

Sherbrooke, Québec, Canada, [April 2023]

avril 2023

Le jury a accepté le mémoire de Marianne Ward dans sa version finale.

Membres du jury

Professeur Jeffrey Quilliam
Directeur de recherche
Département de physique

Professeur Stefanos Kourtis
Membre interne
Département de physique

Professeur Mathieu Juan
Président-rapporteur
Département de physique

April 2023

The jury has accepted the thesis of Marianne Ward in its final version.

Members of the Jury

Professor Jeffrey Quilliam
Research Supervisor
Département de physique

Professor Stefanos Kourtis
Internal Member
Département de physique

Professor Mathieu Juan
Chair-Rapporteur
Département de physique

Résumé

Ces dernières années, les physiciens ont découvert que la structure électronique topologique des matériaux peut avoir des conséquences dramatiques sur leurs propriétés. Dans une nouvelle variété de matériaux topologiques appelés semimétaux de Weyl, les électrons se comportent comme des particules relativistes sans masse. Ces matériaux sont en quelque sorte l'équivalent tridimensionnel du graphène. De nombreux effets magnéto-électriques intéressants, qui pourraient éventuellement s'appliquer aux technologies quantiques, ont été prédits dans les semi-métaux de Weyl et sont encore étudiés aujourd'hui. Des expériences théoriques et préliminaires ont démontré qu'il est possible de sonder la nature topologique de ces matériaux en mesurant la vitesse à laquelle les ondes acoustiques se déplacent à travers le matériau. Cette technique de recherche permet de sonder le volume de l'échantillon et d'éviter certaines erreurs associées aux mesures de conductivité électrique. Dans ce projet, nous explorons expérimentalement comment l'application d'un champ magnétique modifie la vitesse et l'absorption du son dans le semi-métal de Weyl NbP. Nous montrerons comment les champs magnétiques appliqués ont un effet anisotrope sur la vitesse du son et nous comparerons avec les résultats précédents sur le matériau isostructural TaAs. Contrairement à ce qui a été observé dans le TaAs, nos mesures ne montrent pas de preuves significatives de l'anomalie chirale. Les mesures de vitesse du son présentent également des oscillations quantiques qui nous permettent de caractériser la surface de Fermi du matériau. Nous avons également effectué des mesures de transport sur le même matériel, le NbP, comme mesure complémentaire des oscillations quantiques.

MOTS CLÉS: Semimétaux de Weyl, messures ultrasonores, mesures de transport, vitesse du son, anomalie de Chiral

Abstract

In recent years, physicists have discovered that the topological electronic structure of materials can have dramatic consequences on their properties. In a new variety of topological materials called Weyl semimetals, electrons behave as massless relativistic particles. These materials are in some sense a 3-dimensional equivalent to graphene. Many interesting magneto-electric effects, that could possibly be applicable to quantum technologies, have been predicted in Weyl semimetals and are still studied today. Theoretical and preliminary experiments have demonstrated that it is possible to probe the topological nature of these materials by measuring the speed at which acoustic waves travel through the material. This research technique allows us to probe the volume of the sample and to avoid certain errors associated with electrical conductivity measurements. In this project, we explore experimentally how the application of a magnetic field modifies the speed and absorption of sound in the Weyl semimetal NbP. We will show how applied magnetic fields have an anisotropic effect on the sound velocity and compare with previous results on the isostructural material TaAs. In contrast to what was observed in TaAs, our measurements do not show significant evidence of the chiral anomaly. The sound velocity measurements also exhibit quantum oscillations that allow us to characterize the Fermi surface of the material. We have also carried out transport measurements on the same material NbP as a complementary measurement of quantum oscillations.

KEYWORDS: Weyl semimetals, Ultrasound, Transport, Sound velocity, Chiral anomaly

Acknowledgements

I would like to thank Professor Jeffrey Quilliam for supporting and guiding me throughout my research. This thesis would not have been possible without his help.

I would also like to thank Jordan Baglo for his assistance over the past two years. His support with all of my data collection and our many discussions allowed me to obtain beautiful results throughout my degree.

I would also like to thank Quentin Barthélemy for helping me with my data collection. Thank you to Professor Haidong Zhou at the University of Tennessee, Knoxville for fabricating all of the samples I used during my research.

I would especially like to thank my parents for all of their support throughout my academic career. Finally, I would like to thank my cats, Anakin, Padmé, and Kenai, for all of their emotional support during the many long days spent in the lab and writing my thesis.

Contents

List of Figures

List of Tables

Chapter 1

Introduction

The topic of topological insulators has been a very popular area of research for the past 10 years. Topological insulators show potential for many applications such as field-effect transistors, photodetectors, spintronic devices, the switching of magnetic memory, as well as many other applications [1–4]. Topology refers to the study of shapes and their arrangement in space [5] and in the case of topological materials it concerns the "shape" of the wavefunctions of the electronic band structure. Topological insulators have inverted bulk band structures that topologically give rise to metallic surface states[6]. These surface states have a Dirac cone-type dispersion located inside the bulk energy gap [6] with a spin and a momentum that are perpendicular to each other [6]. These metallic surface states are protected by the topology of the band structure. Small perturbations of the system can be expected to modify certain material properties, but the metallic surface states are robust against small perturbations as they are a consequence of a topological invariant that cannot be altered without a significant modification of the electronic structure. To use a playful analogy, the subtly perturbed band structure of a topological insulator remains a topological insulator, just as a doughnut continuously deformed into a coffee cup remains topologically equivalent to the original doughnut. A strong, discontinuous deformation of a doughnut is required to make a sphere, which is not topologically equivalent to the original doughnut [7]. Similarly, a strong discontinuous perturbation that requires a closing of the

gap in the bulk of a topological insulator is required to make it into a topologically trivial insulator and do away with the metallic surface states.

More recently it has been discovered that certain types of materials, known as Weyl semimetals, also exhibit topologically protected metallic states in the *bulk* of the material, as well as novel topologically protected surface states. It is this class of materials that is explored in this thesis.

1.1 Weyl semimetals

Weyl fermions were first predicted by Hermann Weyl in 1929 when he demonstrated the existence of massless fermions in the Dirac equation [8]. It is only recently that Weyl fermions have been discovered in quantum materials [6] where they exist as low-energy excitations of so-called Weyl semimetals. In Weyl semimetals, the band structure disperses linearly in three-dimensional momentum space through points called the Weyl nodes [6]. Weyl semimetals have similar band structures to those of topological insulators. The spin-orbit coupling (SOC) opens up a gap after there is a band inversion [6]. However, unlike in topological insulators, the conduction band and the valence band cross at the Weyl nodes in Weyl semimetals[6].

The search for topological invariants in metals requires an evaluation of the Berry curvature, an analog of the magnetic field defined in reciprocal space [9]. In Weyl semimetals, the Berry curvature becomes singular at the Weyl nodes. The Weyl nodes act as monopoles in momentum space with a fixed chirality, acting like a source of positive chirality or as a sink with a negative chirality of the Berry curvature [6]. Integrating the Berry curvature over a Fermi surface surrounding a Weyl node gives a topological invariant known as the Chern number that takes on values ± 1, corresponding to the two possible chiralities [9]. Weyl semimetals require either the breaking of time-reversal symmetry (TRS) or the breaking of the lattice inversion symmetry [6]. Like in the surface states of a topological insulator,

the linear dispersion at the Weyl nodes in the bulk of the material is topologically protected.

Moreover, Weyl semimetals exhibit their own novel surface states. On 2D surface planes of the material, the Fermi surface (FS) exhibits an unclosed line that starts from one Weyl node with a certain chirality, and ends with the second Weyl node with opposite chirality [6]. This line is called a Fermi arc. The Fermi arc of Weyl semimetals is fundamentally different from what is typically seen in topological insulators, regular insulators or metals, all of which have closed Fermi surfaces.
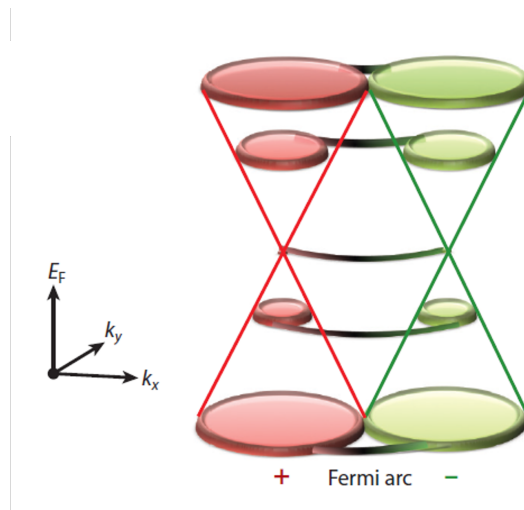
FIGURE 1.1: A pair of Weyl cones with the Fermi energy equal to 0. The pink colour represents positive chirality and the green colour represents negative chirality. A Fermi arc appears at the top and the bottom to connect the pair of Fermi pockets. [6]

1.2 The chiral anomaly

The chiral anomaly consists of the breaking of classical chiral symmetry in a quantum theory [10, 11]. The chiral anomaly is associated with the Weyl fermion quasi-particles, which are massless fermions that carry a definite chirality [12].

In order to measure the chiral anomaly in solid state systems, it is necessary to create a perturbation that couples differently to the two Weyl fermions that are of opposite chiralities [12]. This is naturally realized in applying parallel magnetic

and electric fields to a Weyl semimetal, while the separation of the Weyl cones in momentum space ensures reduced scattering between them. Weyl semimetals are ideal candidates for searching for and studying the chiral anomaly since they are bulk crystals with low energy excitations that satisfy the Weyl equation [12]. The Weyl equation is used to describe Weyl fermions and can come in two forms: the right-handed form and the left-handed form. Each form has a different solution which represent the different possible chiralities. The right-handed form can be derived as follows:

$$\sigma^\mu \partial_\mu \psi = 0$$

where

$$\sigma^\mu = (\sigma^0 \; \sigma^1 \; \sigma^2 \; \sigma^3) = (I_2 \; \sigma_x \; \sigma_y \; \sigma_z)$$

We can then expand the equation:

$$I_2 \frac{1}{c} \frac{\partial \psi}{\partial t} + \sigma_x \frac{\partial \psi}{\partial x} + \sigma_y \frac{\partial \psi}{\partial y} + \sigma_z \frac{\partial \psi}{\partial z} = 0$$

where c is the speed of light (for a real massless particle in a vacuum) or the Fermi velocity of a Weyl fermion in a Weyl semimetal. I_2 is the 2×2 identity matrix for $\mu = 0$, ψ is the wavefunction and σ^μ are the Pauli matrices.

Meanwhile, the left-handed form is given by:

$$\bar{\sigma}^\mu \partial_\mu \psi = 0$$

where

$$\bar{\sigma}^\mu = (I_2 - \sigma_x - \sigma_y - \sigma_z)$$

With a linear dispersion relation in each of the three momentum space directions travelling away from the Weyl node, the conduction band and valence band touch discretely at the Weyl nodes in both situations [12]. Due to the nontrivial topological character of Weyl semimetals, Weyl fermions with opposing chiralities are expected to be separated in momentum space. This enables the pumping of electrons between the opposing chirality Weyl cones that are separated in momentum

space by a parallel magnetic and electric field [12]. This goes against chiral charge conservation. To put it another way, an analogue of the chiral anomaly results from the fact that the number of particles with left and right chirality are conserved separately [12].

The chiral anomaly also serves as a transport signature for Weyl fermions that are in a Weyl semimetal phase. In particular, there is predicted to be a drop in resistance when an electric field is applied parallel to the magnetic field in Weyl semimetals, known as a negative longitudinal magnetoresistance (NLMR).

To depict what is happening, we can consider a cross-section of the Weyl node dispersion in reciprocal space along the k_z direction with two Weyl nodes of opposite chirality ($\chi = +1$ and $\chi = -1$) for $\mathbf{E}=\mathbf{B}=0$ (Figure 1.2a) [13]. The electrons fill the states up to the chemical potential (μ) with right-moving electrons (red circles) and left-moving electrons (blue circles). The Fermi surface will be displaced along k_z when an electric field $\mathbf{E} = E_{\hat{z}}$ is applied to a metal or semimetal. When looking at a Weyl semimetal with the chemical potential located exactly at the Weyl node, there will be a Fermi point instead of a Fermi surface [13]. For any case, the chemical potential will be pushed lower for the right-moving electrons and higher for the left-moving electrons. This leads to a higher number of left-moving electrons and a positive current will be induced (Figure 1.2b). To limit this current, intra-valley scattering (i.e. scattering between left- and right-moving states around the same Weyl node) can occur [13].
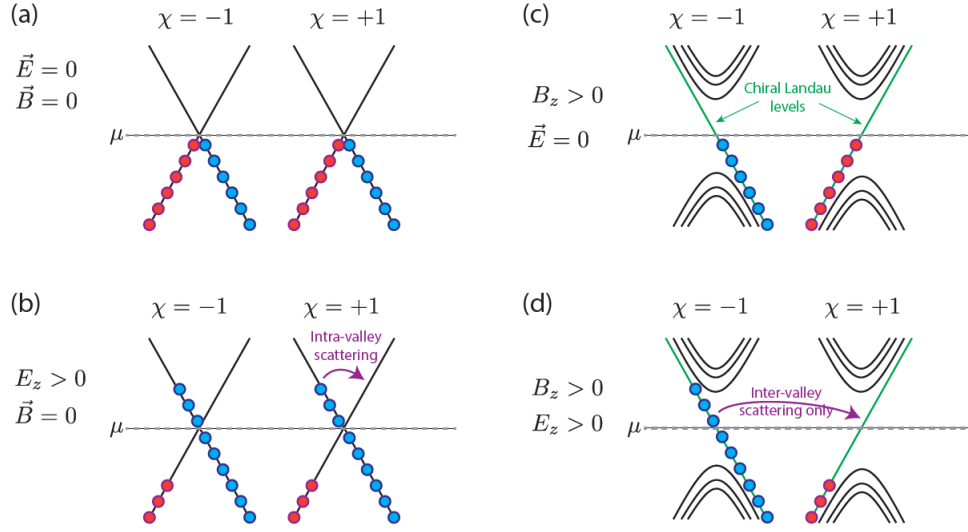
FIGURE 1.2: Schematic of the chiral anomaly in Weyl semimetals that leads to a negative longitudinal magnetoresistance.

When a large magnetic field is applied to the system, the dispersion will be broken into different Landau levels. Most of these levels will be approximately parabolic. However each node will retain one linearly dispersing "chiral Landau level" (green lines in Figure 1.2c). The slope of the chiral Landau level (Fermi velocity) is related to the chirality of the node. In other words, the nodes with right-moving electrons will have a positive chirality and the nodes with left-moving electrons will have negative chirality.

When an electric field is applied in the same direction as the magnetic field, charge pumping will occur from one node to another of opposite chirality (Figure 1.2d). This leads to there being more left-moving electrons than right-moving electrons, and there will therefore be the generation of a current. This time there will be no intra-valley scattering process to limit the flow of current. This is because each node will have only left- or right-moving electrons. There will however be other inter-valley scattering processes that will limit the current and will lead to a non-zero resistivity. It is expected that the inter-valley scattering time will be much larger than the intra-valley scattering time, $\tau_{\text{inter}} > \tau_{\text{intra}}$. This means that for large magnetic fields, $\mathbf{B} \parallel \mathbf{E}$, that is along the direction of the applied voltage, the

resistance of the sample can be expected to be much smaller than when there is no magnetic field. This leads to the negative longitudinal magnetoresistance [14].

This effect does not occur when the magnetic field is perpendicular to the electric field. This is because when $\mathbf{B} \parallel \hat{y}$, for example, k_z will no longer be a good quantum number and the chiral Landau levels will not uniquely have left- or right-moving electrons along the z-axis.

1.2.1   Classes of Weyl semimetals

Weyl semimetals can be separated into two main groups. The first one is the Type-I Weyl semimetals which respect the Lorentz symmetry and the second group is the Type-II Weyl semimetals which do not. In the following sections we will further discuss the differences between both of these families of materials.

1.2.1.1   Type-I Weyl semimetals

In type-I Weyl semimetals, the Dirac cone has both positive and negative dispersion in all directions pointing away from the Weyl nodes. In other words, there is not a significant tilting of the Dirac cone. If the Fermi level is aligned with the Weyl node, the Fermi surface becomes a collection of points, where each point is associated with one Weyl node, and the Fermi surface does not need to cross bands anywhere else. Slight misalignment of the Fermi level leads to small Fermi pockets, each of which surrounds one Weyl node. A larger misalignment leads to more complex surfaces. The type-I Weyl semimetals include the TaAs family which comprises four different materials: TaAs, TaP, NbAs and NbP [6].

The nontrivial Berry phases of the Weyl semimetals and their linear dispersion in principle allow for the detection of the chiral anomaly. While the simplest possible Weyl semimetals could theoretically exhibit just one pair of Weyl nodes, in practice the band structure is more complicated and existing materials exhibit a large number of Weyl nodes [15] The type-I Weyl semimetals in the TaAs family have

two types of Weyl nodes, W1 and W2. These points exist at different momentum positions and energies [6]. Because semimetals have a low inherent charge-carrier density, even tiny changes in the Fermi energy (E_F), brought on by doping and defects, can cause a large shift in the Fermi surface topology [6]. Even in a situation where we have an ideal crystal, the Fermi energy will not necessarily cross the Weyl nodes. Therefore it is necessary to have knowledge of E_F and the resulting Fermi surface topology to link a negative magnetoresistance (MR) to the chiral anomaly[6]. The chiral anomaly has been predicted to be found in TaAs, TaP and NbP. In these semimetals, electron and hole pockets coexist near the nodal ring positions in the Fermi surface [6].

The Fermi arcs' energy dispersion and shape is sensitive to the surface of the structure. It has been shown that the surfaces that are terminated by cations (Ta, Nb) and anions (As, P) have very different Fermi surfaces. An -As or -P terminated surface's typical Fermi surface is made up of spoon- and bowtie-shaped patches (Figure 1.3) [6]. The projections of the W2-type Weyl nodes are connected together by two pieces of Fermi arcs that appear at the top of the spoon-like region. Both of the arcs demonstrate opposite spin texture. The length of the respective Fermi arcs and the separation of these W2 Weyl nodes with opposite chirality are proportional to the strength of the spin orbit coupling (SOC) [6]. The strength of the SOC is in decreasing order for TaAs, TaP, NbAs and NbP. The *p*-orbit dangling bond states of As or P are responsible for the bowtie-like region of the Fermi surface.
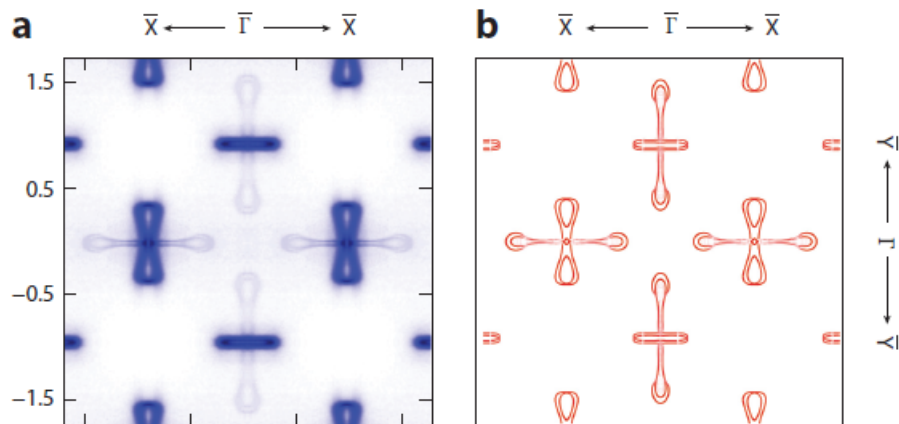
FIGURE 1.3: Shape of Fermi arcs of type-I semimetals. [6]

1.2.1.2 Type-II Weyl semimetals
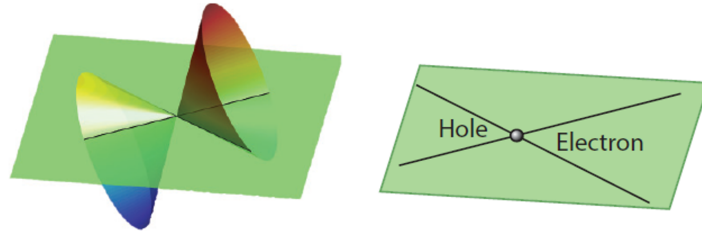
FIGURE 1.4: Strong tilting can be seen in the Weyl cone of type-II Weyl semimetals. [6]

In type-II Weyl semimetals, the Weyl cones show strong tilting. Due to this tilting, the Weyl point is the contact point between the electron pocket and the hole pocket located in the Fermi surface (Figure 1.4). Type-I Weyl semimetals are expected to exhibit the chiral anomaly for all directions [6] but this is not the case for type-II Weyl semimetals. They only show signs of the chiral anomaly when the magnetic direction is normal to a momentum plane that shows a point-like Fermi surface by intersecting the Weyl node [6], otherwise the chiral anomaly disappears. The first theoretically predicted material of this family of Weyl semimetals was that of the layered transition-metal dichalcogenide WTe_2. Another material in this family is $MoTe_2$. Both WTe_2 and $MoTe_2$ show large transverse magnetoresistance [6].

1.2.2 The TaAs family

As previously mentioned, TaAs, TaP, NbAs and NbP are all from the same family of Weyl semimetals. They all have similar crystal structures with the same crystal symmetry. This gives them similar physical properties. However, they are not completely identical and slight differences make each material unique. All four crystals have a body-centred-tetragonal structure, with space group $I4_1md(109)$, but with different lattice parameters. These parameters can be found in Table 1.1. Each crystal has a similar band structure with slight variations. Here I will concentrate on the band structure that has been calculated using first-principles

calculations by Lee *et al.* [16]. Although the results of these calculations might be expected to miss certain details of the real materials, they seem to be largely successful and moreover, provide a clear comparison between the different materials in this family.
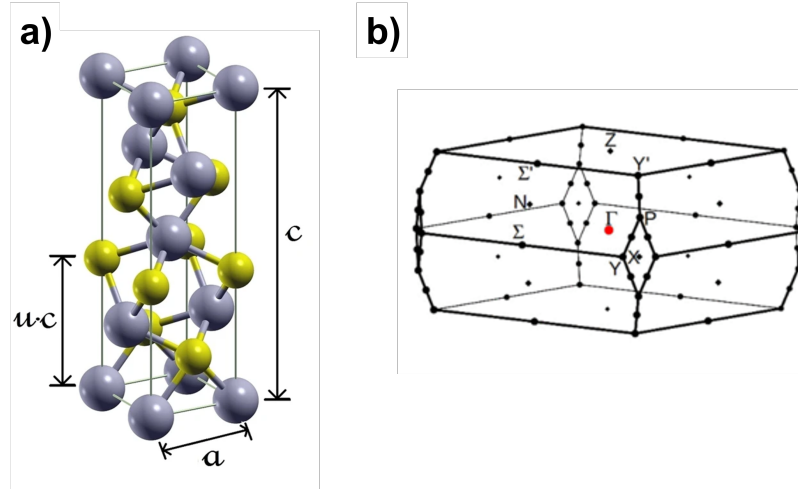
FIGURE 1.5: **a)**The conventional unit cell of TaAs, TaP, NbAs and NbP. The blue atoms are the Ta/Nb atoms and the yellow atoms are the As/P atoms.[17] **b)**The primitive Brillouin zone of the crystals. [16]

	TaAs	TaP	NbAs	NbP
$a(\mathring{A})$	3.437	3.318	3.452	3.334
$c(\mathring{A})$	11.656	11.363	11.679	11.376
u/c	0.333	0.334	0.333	0.334

TABLE 1.1: The experimental lattice parameters of the TaAs family [16]

The band structures of these four Weyl semimetals are characterized by the d orbitals of the Ta and Nb atoms, and the p orbitals of As and P are similar to each other when we are near the Fermi energy [16]. When there is no spin-orbit coupling, the valence bands and the conduction bands cross each other and form closed rings that are bounded together on the $k_x = 0$ and $k_y = 0$ planes [16]. Away from these mirror planes, no accidental band crossings occur. In adding spin-orbit coupling the nodal rings disappear. This leads to the valence band and conduction band being completely gapped along high symmetry lines. The gap

gets smaller when Ta atoms are replaced by Nb atoms (Figure 1.6) indicating a weaker spin-orbit coupling in NbAs and NbP than in TaAs and TaP [16]. When the nodal rings disappear Weyl nodes are left behind.
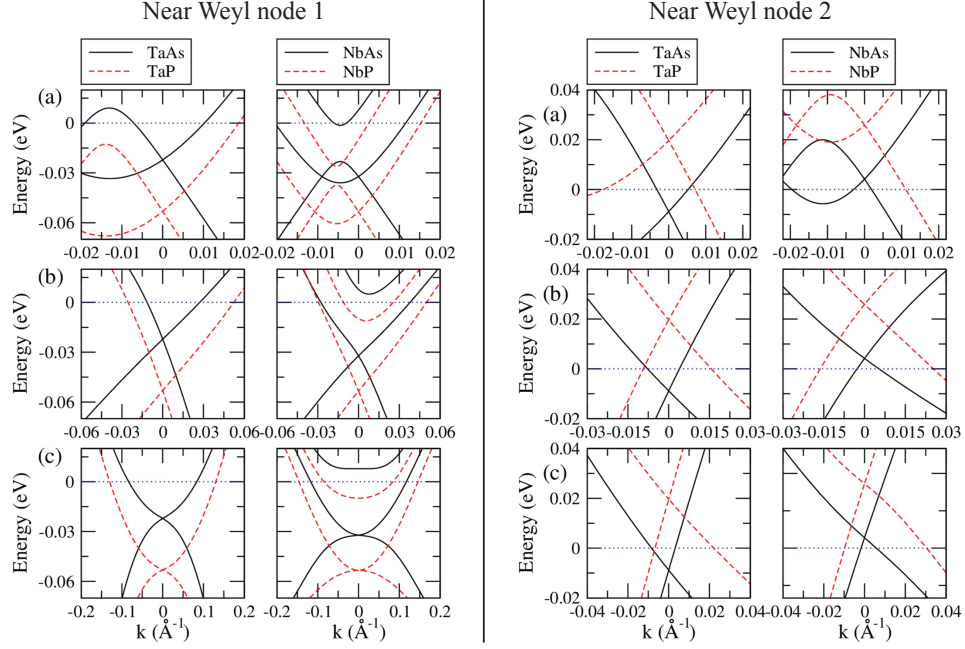
FIGURE 1.6: **LEFT** Band inversion around the W_1 node along **a)**k_x, **b)** k_y and **c)** k_z for TaAs, TaP, NbAs and NbP. **RIGHT** Band inversion around the W_2 node along **a)** k_x, **b)** k_y and **c)** k_z. Adapted from [16]

Not only are there differences in the band structure and the density of states of these crystals, but there are also variations when it comes to the Fermi surfaces. First let us observe the Fermi surface of TaAs. TaAs has the simplest Fermi surface out of all of the materials discussed in this section. Its Fermi surface is formed of both electron and hole pockets. The W1 and W2 points are both below the Fermi energy and the W2 point is closest to the Fermi energy [16]. Compared to the Fermi surface of W2, the Fermi surface of W1 exhibits a considerable degree of anisotropy along k_z and has a larger Fermi surface. Each of the S_{W1} and S_{W2} both encircle a Weyl node. The hole pocket however, does not enclose any Weyl nodes and is therefore topologically trivial. It can be expected to manifest properties of a regular semimetal. The Fermi surface of TaAs can be seen in Figure 1.7.
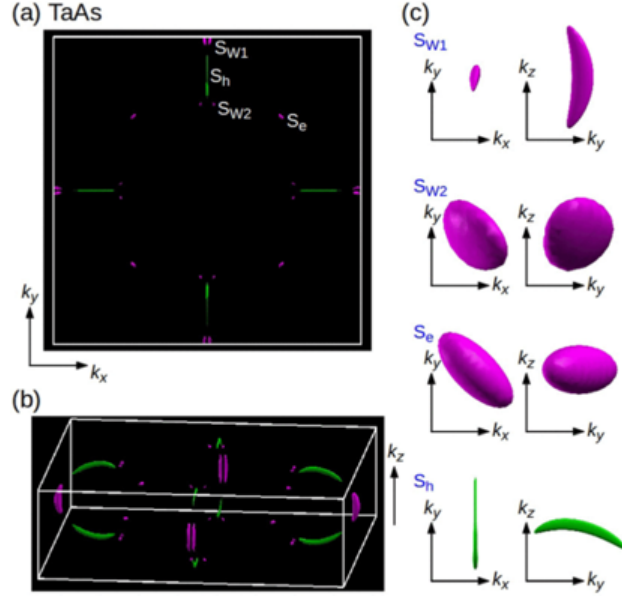
FIGURE 1.7: **a)**Top view and **b)** bird's eye view of the Fermi surfaces of TaAs. **c)**Detailed plots of each individual Fermi surface in TaAs. [16]

The next material we will consider from the Type-I Weyl family is TaP. TaP has a similar Fermi surface to TaAs, however the energy of the W1 point is below the Fermi energy and the energy of the W2 point is above the Fermi energy [16]. A hole pocket encloses TaP's W2 point. TaP also has much larger Fermi surfaces than TaAs. The Fermi surfaces also enclose more than one Weyl node. The electron and hole pockets take the shape of a crescent that is more distributed along the k_z direction. Figure 1.8 shows the Fermi surface of TaP.
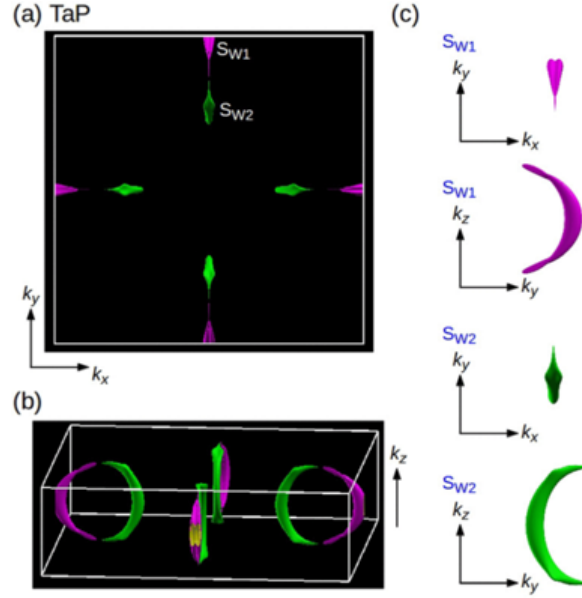
FIGURE 1.8: **a)**Top view and **b)** bird's eye view of the Fermi surfaces of TaP. **c)**Detailed plots of each individual Fermi surface in TaP. [16]

The next material to be discussed is NbAs. The materials containing Nb are more complex with Fermi surfaces within other surfaces. For NbAs, the energy of the W1 is below the Fermi energy and the energy of the W2 node is above the Fermi energy [16]. There are three types of hole-like Fermi surfaces that can be found in NbAs. The first type traverses the $k_z = 0$ plane and encompasses four W2 nodes. The second type resembles the crescents seen in TaP elongated in the k_x and k_y direction. Figure 1.9 does not show the third type because the Fermi energy passes via two spin-split valence bands, which obscure the inner surface within the outer surface. There is also an electron pocket hidden inside the bigger Fermi surface near the W1 node.
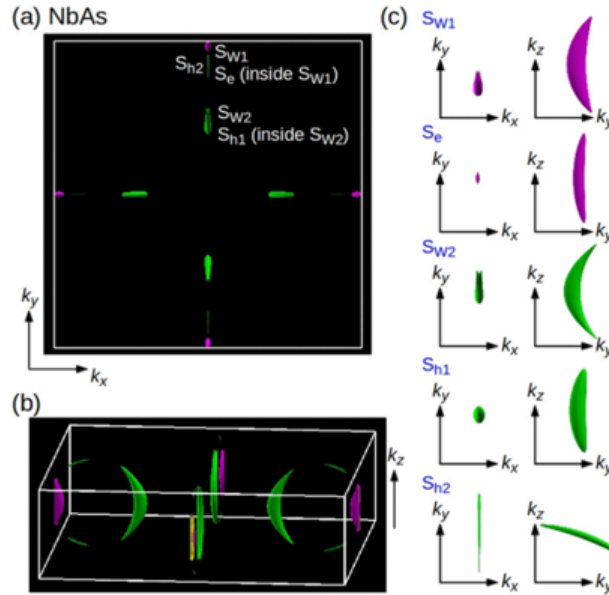
FIGURE 1.9: **a)**Top view and **b)** bird's eye view of the Fermi surfaces of NbAs. **c)**Detailed plots of each individual Fermi surface in NbAs. [16]

The last material in this Weyl family, and the main subject of this thesis, is NbP. Like TaP and NbAs, the energy of the W1 node in NbP is located below the Fermi energy and the energy of the W2 node is located above the Fermi energy [16]. NbP has four crescent shaped Fermi surfaces in the first Brillouin zone. Each of these surfaces contains one more surface inside of it. Each of the outer surfaces contains one pair of W2 nodes. One of the crescent-shaped Fermi surfaces resembles the shape of a half ring. It becomes thinner as it deviates from the W1 node. This Fermi surface contains two additional electron-like Fermi surfaces inside, S_{e1} and S_{e2}[16]. The S_{e1} surface contains one W1 node. The S_{e2} Fermi surface is very small compared to the other surfaces. The Fermi surface of NbP can be seen in Figure 1.10.
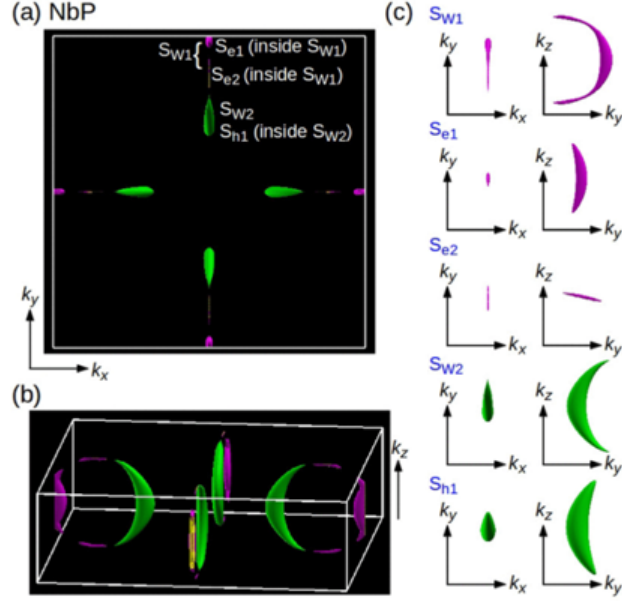
FIGURE 1.10: **a)**Top view and **b)** bird's eye view of the Fermi surfaces of NbP. **c)**Detailed plots of each individual Fermi surface in NbP. [16]

1.3 Quantum oscillations

The application of strong magnetic fields to conducting materials can have a number of interesting effects, but one of the most striking is that of quantum oscillations. In addition to being an exciting macroscopic manifestation of quantum mechanics, these oscillations provide a sensitive probe of the structure of the Fermi surface of a material.

1.3.1 Semi-classical treatment

The velocity of electrons is given by the group velocity which is given by:

$$\boldsymbol{v}(\boldsymbol{k}) = \frac{\partial \omega}{\partial k} = \frac{1}{\hbar}\frac{\partial \boldsymbol{\epsilon}_n(\boldsymbol{k})}{\partial \boldsymbol{k}} \tag{1.1}$$

where $\epsilon_n(k)$ is the energy of band n. This can also be written as:

$$\boldsymbol{v}(\boldsymbol{k}) = \frac{1}{\hbar}\nabla_{\boldsymbol{k}}\boldsymbol{\epsilon}(\boldsymbol{k}) \tag{1.2}$$

In classical mechanics, the rate of change of momentum is given by the force. For this case, the force is given by the Lorentz force. We therefore have:

$$\frac{\partial \boldsymbol{p}}{\partial t} = \hbar \frac{\partial \boldsymbol{k}}{\partial t} = \boldsymbol{F} = q\boldsymbol{v} \times \boldsymbol{B} \tag{1.3}$$

where $q = -e$ is the charge of the particle and $\boldsymbol{B}$ is the magnetic field. The cross-product leads to $\boldsymbol{v}$ and $\boldsymbol{B}$ being perpendicular to $\partial \boldsymbol{k}/\partial t$. By including Equation 1.2 we obtain:

$$\frac{\partial \boldsymbol{k}}{\partial t} = -\frac{e}{\hbar^2} \nabla_k \epsilon(\boldsymbol{k}) \times \boldsymbol{B} \tag{1.4}$$

Because $\partial \boldsymbol{k}/\partial t$ must be perpendicular to $\nabla_k \epsilon$, we have that $\boldsymbol{k}$ is moving in time to follow a path at constant energy. This means that the electrons follow orbits in $\boldsymbol{k}$-space along paths of constant energy. Because $\partial \boldsymbol{k}/\partial t$ must also be perpendicular to $\boldsymbol{B}$, we will have orbits with constant energy that follow a path perpendicular to the magnetic field. Therefore, electrons located at the Fermi surface follows orbits around slices of the Fermi surface perpendicular to the applied magnetic field.

From this, it is possible to show that the time necessary for an electron to complete such an orbit in $\boldsymbol{k}$-space, τ_c, is given by:

$$\tau_c = \frac{\hbar^2}{eB^2} \frac{\partial \mathcal{A}(\epsilon, k_{\parallel})}{\partial \epsilon} \tag{1.5}$$

where $k_{\parallel}$ is the position of the orbit in $\boldsymbol{k}$-space along the direction parallel to the magnetic field, ϵ is the energy of the band (Figure 1.11), and $\mathcal{A}(\epsilon, k_{\parallel})$ is the area of the orbit. The energy at the Fermi level will be what is relevant to the measured quantities.

The cyclotron frequency, ω_c, is given by $\omega_c = \frac{2\pi}{\tau_c}$. It can also be written as:

$$\omega_c = \frac{eB}{m^*_{CR}} \tag{1.6}$$

where the cyclotron mass is given by:

$$m^*_{CR} = \frac{\hbar^2}{2\pi} \frac{\partial \mathcal{A}(\epsilon, k_\parallel)}{\partial \epsilon} \tag{1.7}$$

In simple cases, the cyclotron mass is simply the effective mass, m*, where the effective mass is constant and isotropic.
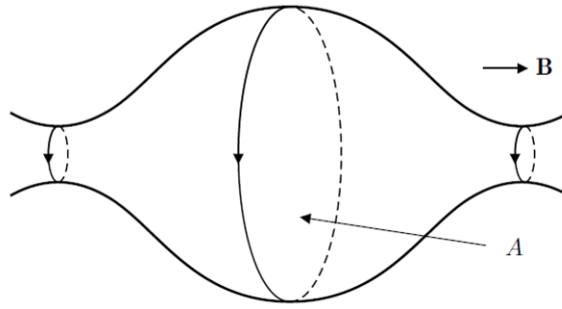
FIGURE 1.11: Schematic of a hypothetical Fermi surface. The different orbits perpendicular to the field direction are possible at different positions $k_\parallel$ along the direction of the magnetic field and different areas $A(E, k_\parallel)$. [18]

1.3.2 Quantum mechanical treatment and Landau levels

When looking at the quantum mechanical treatment, the electrons can be considered as free electrons, but with an effective mass m^*. Note that this is the case for simple metallic systems and not for Weyl semimetals. Ignoring the spin of the electrons, we can include the interaction with a magnetic field in the Hamiltonian by using Peierl's substitution:

$$\mathcal{H} = \frac{(\boldsymbol{p} - q\boldsymbol{A})}{2m^*} \tag{1.8}$$

where $\boldsymbol{A}$ is the vector potential [19, 20]. We can use the Landau gauge and write $\boldsymbol{A} = (0, B_x, 0)$, giving a magnetic field $\boldsymbol{B} = B\hat{z}$. The Schrödinger equation can be

written as:

$$\mathcal{H}\psi = -\frac{\hbar^2}{2m^*}\left[\frac{\partial}{\partial x^2} + \frac{\partial}{\partial z^2} + \left(\frac{\partial}{\partial y} - \frac{eB}{i\hbar}x\right)^2\right]\psi = \epsilon\psi \tag{1.9}$$

From this, the variables can be separated using a solution of the form:

$$\psi(x, y, z) = e^{i(k_y y + k_z z)}\phi(x)$$

The Schrödinger equation then becomes:

$$-\frac{\hbar^2}{2m^*}\left[-k_y^2 - k_z^2 + \frac{\partial^2}{\partial x^2} - \frac{2eBxk_y}{\hbar} - \left(\frac{eBx}{\hbar}\right)^2\right]\psi = \epsilon\psi \tag{1.10}$$

where,

$$x_c = -\frac{\hbar k_y}{eB} \qquad \omega_c = \frac{eB}{m^*}$$

Equation 1.10 can be simplified to:

$$\frac{\hbar^2 k_z^2}{2m^*}\psi + \left[\frac{p_x^2}{2m^*} + \frac{1}{2}m^*\omega_c^2(x - x_c)^2\right]\psi = \epsilon\psi \tag{1.11}$$

The term seen in the square brackets is simply a one-dimensional harmonic oscillator with energy levels $\hbar\omega_c(\nu + 1/2)$ with $\nu = 0, 1, ...$ The possible energies are therefore:

$$\epsilon_{k_z,\nu} = \frac{\hbar^2 k_z^2}{2m^*} + \hbar\omega_c\left(\nu + \frac{1}{2}\right) \tag{1.12}$$

The different values of ν correspond to the different Landau levels. We must add the dispersion along the z direction described by the quantum number k_z to the energy levels.

Each Landau level in the system is now highly degenerate. The level degeneracy n_B depends on the number of values of x_c that one can choose. This will depend on the dimensions of the sample (L_x and L_y), the magnetic field B, and needs to

be multiplied by a factor of 2 to take into consideration the two possible values of the spin. This gives:

$$n_B = \frac{2L_x L_y e B}{h} \tag{1.13}$$

This can be rewritten as:

$$n_B = \frac{\Phi}{\Phi_0} \tag{1.14}$$

where $\Phi = BL_x L_y$ is the magnetic flux through the sample and $\Phi_0 = h/2e$ is the flux quantum. The number of electrons in a sample, n, is generally constant, but as the magnetic field is increased, n_B also increases. This is because there are more and more states available within each level. Therefore, as the magnetic field increases, the Fermi level will, at certain values of field, drop from one Landau level to the next as more space becomes available for the electrons in the lower Landau levels. This switching from one Landau level to another leads to oscillations as a function of inverse field $1/B$ in various measurable quantities. Many measurable quantities will vary sinusoidally with the filling fraction of the Landau levels n/n_B. In other words, a quantity may be maximal when the Fermi level is equal to a Landau level, and minimal when in between Landau levels. This hypothetical quantity f would then vary as:

$$f(B) \propto \cos\left(\frac{2\pi n}{n_B}\right) = \cos\left(\frac{2\pi n h}{BL_x L_y 2eB}\right) \tag{1.15}$$

Which gives oscillations in $1/B$ with a frequency given by $\frac{nh}{2eBL_x L_y}$. These can include quantities such as resistivity (the Shubnikov-de Haas effect) and magnetization (the de Haas-van Alphen effect). It can also include sound velocity and many other quantities. They are universally known as quantum oscillations.

In the case of the Shubnikov-de Haas (SdH) effect, the resistivity is related to the scattering rate. The scattering rate is typically proportional to the density of states (the number of states available into which the electrons can scatter), and the density of states depends critically on the filling factor n/n_B being high when the Fermi energy is matched to a Landau level and being lower when in between

Landau levels. Therefore, oscillations of resistivity occur as a function of $1/B$ with a frequency of F which is measured in Tesla.

1.3.3 Information provided by quantum oscillations

There are many different pieces of information that can be extracted from quantum oscillations. However, it is necessary to do a bit of analysis to obtain this information.

By taking the Fourier transform of quantum oscillations, different peaks will indicate the various quantum oscillation frequencies. These frequencies contain important information regarding the cross-sectional area of the Fermi surfaces. The Fourier transform can also be used to obtain information on the phase of the quantum oscillations, ϕ, of the sample. This can be done using a method called the 2D phase-frequency analysis [21]. This method consists of multiplying the Fourier transform by a phase-factor and plotting the real part of this function using a contour plot.

$$K(\phi, \nu) = Re F(\nu) e^{i\phi} \tag{1.16}$$

The various peaks observed in the contour plot give information on the phase factor of the sample.

Using what is known as the thermal damping factor (R_T), it is possible to extract the effective mass of the sample. This is done by observing the quantum oscillations at various temperatures and plotting out the height of the oscillation peak as a function of the temperature. The height of the peak should follow the following form [22]:

$$R_T = \frac{\alpha T m^*}{H \sinh \frac{\alpha T m^*}{H}} \tag{1.17}$$

where T is the temperature, m^* is the effective mass, H is the magnetic field of the peak, $\alpha = \frac{2\pi^2 k_B m_0}{eh} \approx 14.69$ T/K, and m_0 is the mass of an electron.

By fitting the thermal damping factor to the data, it is possible to extract the value of the effective mass.

Using the effective mass, it is possible to find the Dingle temperature, T_D of the sample. This is done using the Dingle damping factor [22]:

$$R_D = \exp \frac{-\alpha T_D m^*}{H} \tag{1.18}$$

Once the Dingle temperature is obtained, it can be used to estimate the transport scattering rate, $1/\tau$ of the sample:

$$\omega_c \tau = \frac{eB}{m^*} \left(\frac{\hbar}{2\pi k_B T_D} \right) \tag{1.19}$$

1.3.4   Phase factors

For Shubnikov-de Haas oscillations, that is quantum oscillations of the resistivity, the oscillating component can be expressed [23] with

$$\Delta \sigma_{xx} \propto \cos \left[2\pi \left(\frac{F}{B} - \gamma - \frac{1}{2} + \beta \right) \right]$$

The first phase factor γ depends on the topology of the Fermi surface. For largely 2-dimensional dispersion, $\gamma = 0$. For 3-dimensional systems, $\gamma = \pm 1/8$, the sign depending on the curvature of the Fermi surface in the direction parallel to the magnetic field. Therefore maximal and minimal cross-sections of the Fermi surface are expected to give opposite signs of γ. The additional phase factor β is given by

$$\beta = \frac{\Phi_B}{2\pi}$$

where Φ_B is the Berry phase, expressed by

$$\Phi_B = \oint_\Gamma \vec{\Omega}(\vec{k}) d\vec{k}$$

where the line integral is performed around the Γ-orbit (where Γ is the index that refers to a particular orbit) in $\vec{k}$-space and

$$\vec{\Omega}(\vec{k}) = i \int d\vec{r} u_{\vec{k}}^*(\vec{r}) \nabla_{\vec{k}} u_{\vec{k}}(\vec{r})$$

$u(\vec{r})$ is the Bloch function and the integral is performed over a unit cell [24].

Therefore, if γ is known, the phase of quantum oscillations allows for the determination of the Berry phase of a particular Fermi surface pocket. For instance, in measurements of graphene, the phase of quantum oscillations gave $\beta = 1/2$ ($\Phi_B = \pi$), resulting from the presence of Dirac quasi-particles [25].

In measurements of graphite [21] oscillations from multiple Fermi surfaces were studied with de Haas-van Alphen measurements and varying phase factors were obtained. This was done with a phase analysis method that consisted of identifying peaks in a contour plot of the $\Re[e^{i\phi}\tilde{f}(F)]$ vs. frequency F and phase ϕ. Here $\tilde{f}(F)$ is the Fourier transform of the measured quantity as a function of $1/B$, be it magnetization, resistivity or sound velocity. The de Haas-van Alphen (magnetization) measurements present an additional phase factor μ which is $+1$ for electrons and -1 for holes.

In previous sound velocity measurements on TaAs, the phase factor from a trivial hole pocket and a topological (Weyl) electron pocket were compared and a phase difference of π was observed [26]. While the value of γ was not necessarily well understood, the phase difference of π could be attributed to a difference in Berry phase : $\Delta\beta = 1/2$ or $\Delta\Phi_B = \pi$, suggesting $\Phi_B = 0$ for the trivial hole pocket and $\Phi_B = \pi$ for the Weyl pocket.

Several previous works have attempted to extract the Berry phase from quantum oscillations in NbP using de Haas-van Alphen (dHvA) measurements [27] and Shubnikov-de Haas (SdH) measurements [28–30]. The results are quite inconsistent. For example, for a frequency of 31 T, several different values of $\Phi_B/2\pi$ are found: 0.54 [27] (topological), 0 [30] (trivial) and 0.3 or 0.13, depending on the field range used for fitting [29]. These inconsistent results demonstrate how challenging such an analysis can be.

1.4 Quantum oscillations and Fermi arcs

In addition to closed Fermi surfaces in the bulk, it is also important to consider how surface Fermi arcs contribute to quantum oscillations. Following the work of Potter *et al.* [31], it is possible to do a semiclassical analysis of Weyl semimetals to demonstrate the behaviour of the Fermi arcs in such materials. They consider the simplest possible case, that of a single pair of Weyl nodes with opposite chirality ± 1 positioned at $\mathbf{k} = \pm k_W$ and with a magnetic field B along the y direction. In an infinite system, Landau level (LL) bands that disperse only along the field direction are generated under applied magnetic field[31]. It is found that Weyl nodes of opposite chirality are decoupled for $k_W l_B \gg 1$[31] with $l_B = \frac{1}{\sqrt{eB}}$ as the magnetic length. As was discussed in Section 1.2 and illustrated in Figure 1.2, the spectrum of Landau levels includes gapped bands with energies $\epsilon_n^\pm(k_y) \approx \pm \nu \mathrm{sgn}(n)\sqrt{2|n|l_B^{-2} + k_y^2}$ with n=1,2,... and gapless modes (so-called chiral Landau levels) with energies $\epsilon_0^\pm(k_y) = \pm \nu k_y$ where the $\pm$ labels the chirality of the nodes[31].

Next, they consider a Weyl semimetal slab that is infinite in the $\hat{\mathbf{x}}$- and the $\hat{\mathbf{z}}$-directions but with a finite thickness L along $\hat{\mathbf{y}}$ (though it is considered to be thick enough that tunneling between surface states on opposite surfaces can be neglected). In a semiclassical description, an electron at k_z in the Fermi arc of the top surface follows a path along the arc towards the Weyl node with a negative chirality[31]. This is determined from:

$$\partial_t \boldsymbol{k} = -e\boldsymbol{v_k} \times \boldsymbol{B} = e\nu B\hat{\boldsymbol{t}_k} \tag{1.20}$$

The velocity v on the Fermi arc taken to be independent of $\mathbf{k}$. $\hat{\mathbf{t}}_k$ is the unit vector tangent to the arc. When the electron approaches the negative bulk Weyl node, the energy gap to the bulk bands vanishes [31], a semiclassical single-band description no longer works and the electron is transferred from the surface arc into the bulk [31]. The gapless bulk chiral Landau level transports the electron from the Fermi arc on the top surface to the Fermi arc on the bottom surface [31].

Upon arriving at the bottom of the sample, the electron continues its orbit along the Fermi arc toward the positive Weyl node, where it then passes through the upwards moving chiral bulk LL, returning to the top-surface (Figure 1.12). This allows the electron to complete an orbit, albeit a complicated orbit in a hybrid of momentum space and real space.
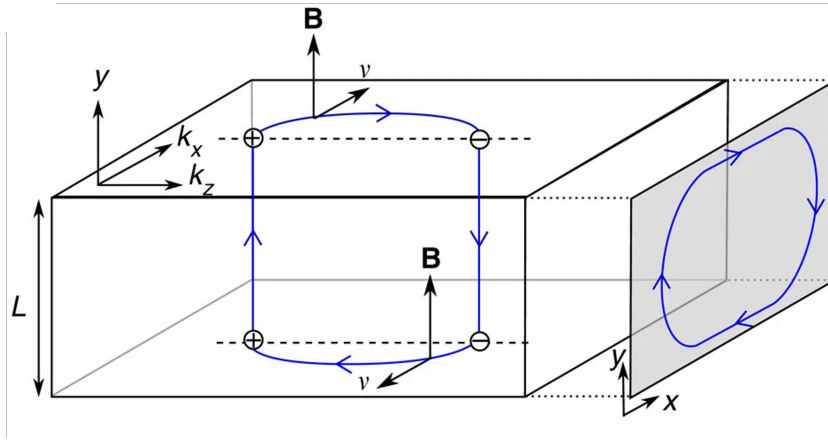
FIGURE 1.12: The semiclassical orbit of an electron moving along the Fermi arc from one Weyl node to the other Weyl node of opposite chirality[31]

Potter *et al.* obtain the following quantum energy levels for these orbits:

$$\epsilon_n = \frac{\pi\nu(n+\gamma)}{L + k_0 l_B^2} \tag{1.21}$$

where zero energy corresponds to the Weyl nodes. The magnetic orbits involving Fermi arcs can be distinguished from conventional bulk quantum oscillations by the dependence of the slab thickness, L [31].

A possible observation of quantum oscillations originating from surface states of the Weyl semimetal TaAs was obtained by Nair *et al.* using transport measurements at very high magnetic fields [32].

Chapter 2

Sound Velocity

2.1 Physical Concepts

The anisotropies present in a crystalline solid make sound propagation more complicated than in a homogeneous medium like a liquid or a gas. Various physical concepts must first be understood, including the strain, stress and elasticity tensors, as well as Christoffel's equation, the crystalline equivalent of the wave equation. These concepts will be discussed in detail in the following sections.

2.1.1 Strain

When an elastic deformation occurs, a volume element located at $\boldsymbol{R}$ will be shifted to $\boldsymbol{R'} = \boldsymbol{R} + \boldsymbol{u}(\boldsymbol{R}, t)$ where $\boldsymbol{u}(\boldsymbol{R}, t)$ is the displacement vector. This deformation can both be space dependent and time dependent [33]. If $\boldsymbol{u}$ does not depend on $\boldsymbol{R}$ then we only have a translation and not a deformation. If we look at a second point close to $\boldsymbol{R}$ and that is denoted as $\boldsymbol{R} + \boldsymbol{dR}$, this point will shift to $\boldsymbol{R'} + \boldsymbol{dR'}$ and we will have $\boldsymbol{dR'} = \boldsymbol{dR} + \boldsymbol{du}$. These vectors can be seen in Figure 2.1.
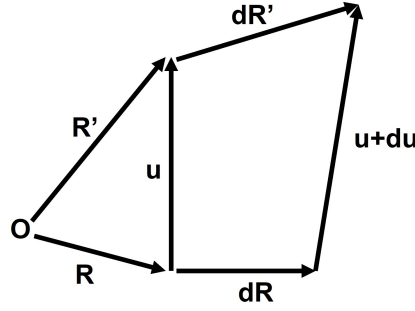
FIGURE 2.1: The displacement vectors when a material is under strain. Adapted from ref. [33].

When we have deformations, $\boldsymbol{u}$ is dependent on the position. We can express $\boldsymbol{dR'}$ with:

$$v_{ij} = \frac{\partial u_i}{\partial R_j}, \quad i.e. \quad dR'_i = dR_i + \sum_j v_{ij} dR_j \tag{2.1}$$

Here $v_{ij} = \frac{\partial u_i}{\partial R_j}$ is a component of the deformation tensor [33]. This quantity is zero for a homogeneous displacement of the material. We have a homogeneous deformation if v_{ij} is not position dependent.

A drawback of the deformation tensor is that it is also non-zero for homogeneous rotations of the crystal, which do not contribute to its energy [34]. The deformation tensor can be decomposed into a symmetric part, which gives pure *strain*, and an anti-symmetric part which represents rotations.

Elements of the symmetric strain tensor are therefore expressed as

$$s_{ij} = \frac{1}{2}(v_{ij} + v_{ji}) = \frac{1}{2}\left(\frac{\partial u_i}{\partial R_j} + \frac{\partial u_j}{\partial R_i}\right) \tag{2.2}$$

The anti-symmetric rotation tensor is conversely given by

$$\Omega_{ij} = \frac{1}{2}(v_{ij} - v_{ji}) = \frac{1}{2}\left(\frac{\partial u_i}{\partial R_j} - \frac{\partial u_j}{\partial R_i}\right) \tag{2.3}$$

The importance of the strain tensor can be understood by considering how the length of a vector within the material changes as a deformation is applied. The

difference in length between dR' and dR is given by

$$dR' \cdot dR' - dR \cdot dR = \sum_{\alpha\beta} 2\eta_{\alpha\beta} dR^\alpha dR^\beta$$

where

$$\eta_{ij} = \frac{1}{2} \left(v_{ij} + v_{ji} + \sum_\alpha v_{\alpha i} v_{\alpha j} \right) \tag{2.4}$$

For infinitesimal deformations (that is $v_{ij} \ll 1$), $\eta_{ij} = s_{ij}$ becomes the strain tensor. Usually, the small deformations are enough for a description of sound waves and many of their properties [33]. Hence, in the limit of small deformations, length changes within the material depend only on the symmetric part of the deformation tensor, the strain. If $s_{ij} = 0$, the deformation is a pure rotational and does not change any length elements.

2.1.2 Stress

There is not only a strain tensor that has to be taken into consideration when doing sound velocity measurements, it is also necessary to look at the stress tensor. When we have a solid with no deformations at the equilibrium state, the resultant forces on a volume element will be zero [33]. When there is strain within a material, there are forces that will be created which will try to return the body to equilibrium. These internal forces that occur when the solid is deformed are called internal stresses. When doing a continuum approximation, the molecular forces have a short range which leads to the following expression for a volume element of a deformable body:

$$\int F_i dV = \int \sum_k \frac{\partial \tau_{ik}}{\partial R_k} dV = \int \sum_k \tau_{ik} df_k \tag{2.5}$$

where $\boldsymbol{F}dV$ is the force on a volume element dV, τ_{ik} is an element of the stress tensor and df_k is a component of the surface element vector $d\boldsymbol{f}$ [33]. These internal stresses do not consider various homogeneous external forces such as gravity, external pressure, magnetic volume force, etc.

2.1.3 Christoffel's Equation

In condensed matter physics it is important to be able to relate the stiffness tensor with the sound velocities of solids. The stiffness tensor is used to characterize a materials behaviour when it is under stress in the elastic regime [35]. The stiffness tensor is either represented by a 4-tensor in 3D space with 81 components, or by a symmetric 6×6 matrix. The 21 components of the matrix elements of the matrix are the elastic constants [35]. Since sound waves induce elastic deformations, the stiffness tensor contains information about how the sound waves behave, notably their velocity [35]. In turn, it is possible to obtain information on the elastic constants by virtue of sound velocity measurements.

The stiffness tensor $\boldsymbol{C}$ is an important property when analyzing materials. It can relate strains and stresses through Hooke's law in the elastic regime:

$$\tau_{ij} = \sum_{mn} C_{ijmn} s_{mn} \tag{2.6}$$

where τ is the stress tensor and s is the strain tensor. The sum in equation 2.6 runs over the three Cartesian coordinates. When expanding this equation, we obtain:

$$\begin{pmatrix} \tau_1 \\ \tau_2 \\ \tau_3 \\ \tau_4 \\ \tau_5 \\ \tau_6 \end{pmatrix} = \begin{pmatrix} C_{11} & C_{12} & C_{13} & C_{14} & C_{15} & C_{16} \\ C_{21} & C_{22} & C_{23} & C_{24} & C_{25} & C_{26} \\ C_{31} & C_{32} & C_{33} & C_{34} & C_{35} & C_{36} \\ C_{41} & C_{42} & C_{43} & C_{44} & C_{45} & C_{46} \\ C_{51} & C_{52} & C_{53} & C_{54} & C_{55} & C_{56} \\ C_{61} & C_{62} & C_{63} & C_{64} & C_{65} & C_{66} \end{pmatrix} \begin{pmatrix} s_1 \\ s_2 \\ s_3 \\ 2s_4 \\ 2s_5 \\ 2s_6 \end{pmatrix} \tag{2.7}$$

Equation 2.7 is written out using the Voigt notation which is defined as:

$$\begin{aligned} 1 &\to xx & 4 &\to yz \\ 2 &\to yy & 5 &\to xz \\ 3 &\to zz & 6 &\to xy \end{aligned} \tag{2.8}$$

The factors of 2 in the strain tensor of equation 2.7 are there to take care of the double counting and to ensure that equation 2.7 corresponds to equation 2.6 [35].

The stiffness tensor contains not only information about the static deformations, but also about the elastic waves that are traveling through the material [35]. It is possible to obtain the dispersion relation of these waves by solving the Christofell equation:

$$\sum_{ij}[M_{ij} - \rho\omega^2\delta_{ij}]P_j = 0 \tag{2.9}$$

for a monochromatic plane wave with wave vector $\boldsymbol{q}$, frequency ω and polarization $\hat{\boldsymbol{P}}$ in a material with density ρ. The Christoffel matrix $\boldsymbol{M}$ is defined as:

$$M_{ij} = \sum_{mn} q_n C_{imnj} q_m \tag{2.10}$$

This equation is a simple eigenvalue problem that can be solved for arbitrary $\boldsymbol{q}$ [35]. The result will give a set of three frequencies and polarization for each value of $\boldsymbol{q}$. Given that $\boldsymbol{M}$ is real and symmetric, the eigenvalues will be real and the vectors $\{\hat{\boldsymbol{P}}_n\}$ make up an orthogonal basis. The requirement that $\boldsymbol{C}$ be positive ensures that ω^2 is real and positive [35].

2.1.3.1   Elastic Constant for Tetragonal Systems

Since niobium phosphide (NbP) is a tetragonal crystal, we will want to find the elastic tensor for a tetragonal system. We will first start by reducing the number of independent elastic constants in the tensor. From equation 2.7 we can see that the elastic constant tensor $\boldsymbol{C}$ contains 36 independent elastic constants. This can be further reduced to 21 elastic constants by using the laws of thermodynamics.

Starting from the first law of thermodynamics, we have:

$$dU = \delta Q + \delta W \tag{2.11}$$

where dU is the change of the internal energy of the system, δW is the work done on the system, and δQ is the heat flow into the system [36]. Here, δ indicates an infinitesimal change and d indicates a differential. When we have reversible processes, the second law of thermodynamics gives:

$$\delta Q = TdS \tag{2.12}$$

which gives:

$$dU = TdS + \delta W \tag{2.13}$$

where S is the entropy and T is the temperature.

In adiabatic systems, there is no heat exchange between the system and the surrounding environment. Therefore, $\delta Q = 0$ and $dS = 0$. This gives us $dU = \delta W$ and δW is given by

$$\delta W = \sum_{kl} \tau_{kl} ds_{kl} \tag{2.14}$$

Using $dU = \delta W$ and equation 2.14, we obtain:

$$dU = \sum_{kl} \tau_{kl} ds_{kl} \tag{2.15}$$

which leads us to:

$$\tau_{kl} = \left(\frac{\partial U}{\partial s_{kl}} \right)_s \tag{2.16}$$

By combining equation 2.6 and equation 2.16 we obtain:

$$C^S_{klmn} = \left(\frac{\partial \tau_k l}{\partial s_{mn}} \right)_S = \left(\frac{\partial^2 U}{\partial s_{kl} \partial s_{mn}} \right)_S = \left(\frac{\partial^2 U}{\partial s_{mn} \partial s_{kl}} \right)_S = C^S_{mnkl} \tag{2.17}$$

Equation 2.17 indicates that components in the elastic tensor are given by $C_{mn} = C_{nm}$. This allows us to rewrite equation 2.7 as:

$$
\begin{pmatrix} \tau_1 \\ \tau_2 \\ \tau_3 \\ \tau_4 \\ \tau_5 \\ \tau_6 \end{pmatrix} = \begin{pmatrix} C_{11} & C_{12} & C_{13} & C_{14} & C_{15} & C_{16} \\ C_{12} & C_{22} & C_{23} & C_{24} & C_{25} & C_{26} \\ C_{13} & C_{23} & C_{33} & C_{34} & C_{35} & C_{36} \\ C_{14} & C_{24} & C_{34} & C_{44} & C_{45} & C_{46} \\ C_{15} & C_{25} & C_{35} & C_{45} & C_{55} & C_{56} \\ C_{16} & C_{26} & C_{36} & C_{46} & C_{56} & C_{66} \end{pmatrix} \begin{pmatrix} s_1 \\ s_2 \\ s_3 \\ 2s_4 \\ 2s_5 \\ 2s_6 \end{pmatrix} \tag{2.18}
$$

There are therefore only 21 independent elastic constants in the elastic matrix. This is the elastic matrix for a triclinic crystal which is the crystal structure with the lowest symmetry. Tetragonal crystals have a higher symmetry and therefore have fewer independent elastic constants [36].

For the tetragonal system of niobium phosphide, we have mirror planes or equivalently for the present argument, two-fold rotation axes perpendicular to the x_3 axis [36]. This indicates that if the subscript 1 or 2 appears an odd number of times, the corresponding elastic constant is zero [36]. For example, $C_{16} = C_{1112}$ is zero. Applying this to our result in equation 2.18, we get the following for the elastic constant matrix:

$$
\boldsymbol{C} = \begin{pmatrix} C_{11} & C_{12} & C_{13} & 0 & 0 & 0 \\ C_{12} & C_{11} & C_{13} & 0 & 0 & 0 \\ C_{13} & C_{13} & C_{33} & 0 & 0 & 0 \\ 0 & 0 & 0 & C_{44} & 0 & 0 \\ 0 & 0 & 0 & 0 & C_{44} & 0 \\ 0 & 0 & 0 & 0 & 0 & C_{66} \end{pmatrix} \tag{2.19}
$$

The final matrix for the tetragonal system of NbP only has 6 independent elastic constants.

2.1.3.2 Resolution of Christoffel's equation for our system

It is possible to solve Christoffel's equation for a tetragonal system with sound waves propagating in the [110] direction. As previously stated, Christoffel's equation is given by:

$$\sum_{ij} \left[M_{ij} - \rho \omega^2 \delta_{ij} \right] P_j = 0$$

The frequencies can be found by solving the eigenvalue problem determined by:

$$\det \left[M_{ij} - \rho \omega^2 \delta_{ij} \right] = 0$$

The polarization vectors of the corresponding modes are given by the eigenvectors of the matrix M_{ij}. For a tetragonal system with sound waves propagating along the [110] direction we have the following wavevector:

$$\vec{q} = \frac{q}{\sqrt{2}}(1, 1, 0)$$

The Christoffel matrix is therefore given by:

$$M_{ij} = \sum_{mn} q_n C_{imnj} q_j = \frac{q^2}{2} \left[C_{i11j} + C_{i22j} + C_{i21j} + C_{i12j} \right]$$

Given the structure of the elasticity tensor this can be written as

$$\mathbf{M} = \frac{q^2}{2} \begin{pmatrix} C_{11} + C_{66} & C_{12} + C_{66} & 0 \\ C_{12} + C_{66} & C_{11} + C_{66} & 0 \\ 0 & 0 & 2C_{44} \end{pmatrix}$$

From this it is possible to find the following eigenvectors: a longitudinal polarization $\vec{P}_L \propto (1, 1, 0)$; a transverse in-plane polarization $\vec{P}_{T_p} \propto (1, -1, 0)$; and a transverse out-of-plane polarization $\vec{P}_{T_z} = (0, 0, 1)$. From the Christoffel equation, we can find the frequencies of the three modes as well as their velocities using

$v_i = \omega_i/q$. The mode velocities are given by:

$$v_L = \sqrt{\frac{2C_{66} + C_{11} + C_{12}}{2\rho}}$$

$$v_{Tp} = \sqrt{\frac{C_{11} - C_{12}}{2\rho}}$$

$$v_{Tz} = \sqrt{\frac{C_{44}}{\rho}}$$

For the measurements shown in the next chapters, data was collected with the mode having polarization in the $\hat{z}$ direction and with a sound velocity given by $v_{T_z} = \sqrt{C_{44}/\rho}$

Chapter 3

Sound Velocity Measurements

When candidate Weyl semimetals such as TaAs and NbP were discovered, one of the first results investigated by researchers was a measurement of the chiral anomaly, which is expected to create a drop in resistivity when the magnetic field and electric field are parallel. This is known as the Negative Longitudinal Magnetoresistance (NLMR). Many high-profile papers were quickly published exhibiting such an effect in a particular range of magnetic fields [12, 37–39]. It was however quickly discovered that the measured effect depends highly on the sample, sample geometry and the way in which the contacts are applied to the sample [40]. It is understood that the NLMR can be caused by the current jetting effect or a highly non-uniform distribution of current within the sample [41, 42]. These experimental limitations call into question the accuracy of the NLMR measurement and therefore the observation of the chiral anomaly.

Ramshaw *et al.* have attempted to better prepare samples and contacts to measure TaAs for example by using a Focused Ion Beam (FIB) to shape the sample and then deposit contacts in order to achieve samples with high aspect ratios and avoid point-like contacts [42]. This process has some drawbacks, including the presence of superconductivity in an amorphous surface layer of Ta created by the FIB processing.

The primary aim of the sound velocity measurements carried out in this project was to provide an alternative measure of the magnetoresistance of Weyl semimetals which will not be sensitive to current jetting effects. Since the materials in the TaAs family are piezoelectric, certain kinds of strain induce a dielectric polarization. This is the case for the strain waves associated with a measurement of the C_{44} mode which induces a polarization along the direction of the sound-wave propagation, in our case [110] [26]. In the absence of conduction electrons, this ionic polarization leads to an additional restoring force that increases the elastic constant and therefore the sound velocity. However, in a conductor, the conduction electrons can screen the dielectric polarization and reduce this effect, thereby lowering the sound velocity [43, 44]. Qualitatively speaking, the higher the conductivity, σ, the lower the sound velocity. Hence, sound velocity measurements can, in principle, provide a measurement of the AC conductivity of a material at the measurement frequency. Indeed, Laliberté *et al.* found tentative evidence of a chiral anomaly in TaAs with sound velocity measurements where a decrease in sound velocity (indicative of an increase in conductivity) was seen when the magnetic field was oriented parallel to the sound wave propagation direction (as compared to measurements with $\vec{q} \perp \vec{B}$) [26]. It is therefore important to try and reproduce these results in other Weyl semimetals such as NbP.

3.1   Sample Preparation

All measurements were done on NbP samples. Our samples were fabricated by Haidong Zhou and members of his research group at the University of Tennessee, Knoxville. The sample used for ultrasound measurements had a house-like shape with dimensions in the *a*-, *b*-, and *c*-axis: 2.76mm, 2.89mm and 3.11mm respectively. A schematic of the sample dimensions can be seen in Figure 3.1.
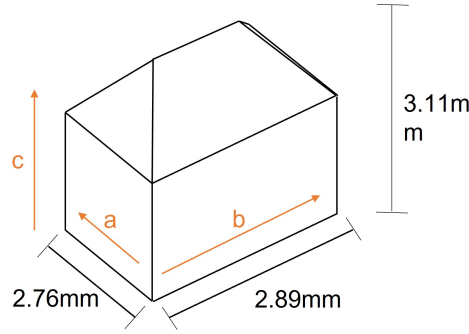
FIGURE 3.1: Schematic of the NbP ultrasound sample.

Due to the Fermi surfaces of NbP, measurements were taken with the current in the [110] direction. This was done in order to have an equal contribution from the various Fermi surfaces and to reduce the number of waveforms (quantum oscillations) being added together in the frequency vs. magnetic field plots. For example, if the magnetic field and the wavevector are along the b-axis ([010]), certain Fermi surfaces will have a smaller cross-section perpendicular to the field than others (Figure 3.2a and Figure 3.2b). Similarly, if the wavevector is along the b-axis with the field along the a-axis, we will once again have different contributions from the Fermi surfaces (Figure 3.2c and d). The waveforms in the final results will be added together, making these orientations useless for observing certain phenomena such as the chiral anomaly.

This is why we would want a configuration like the one seen in Figures 3.2e and 3.2f. This gives the same oscillations in every Fermi surface whether the field is perpendicular or parallel to the direction of the sound-wave propagation. This means that any measured anisotropies (i.e. changes in sound velocity between $\vec{B} \parallel [110]$ and $\vec{B} \parallel [1\bar{1}0]$) could be attributed to the chiral anomaly or other novel sources of anisotropy in the crystal's properties. This is the same measurement set-up that was employed in previous acoustic measurements of the related Weyl semimetal TaAs [26].

In order to prepare the sample to have this orientation, two corners opposite of each other were polished in order to have two flat surfaces parallel to each other. This must be precisely done to ensure that the current properly passes through the sample. A transducer was then glued using silicon glue on one of the flat
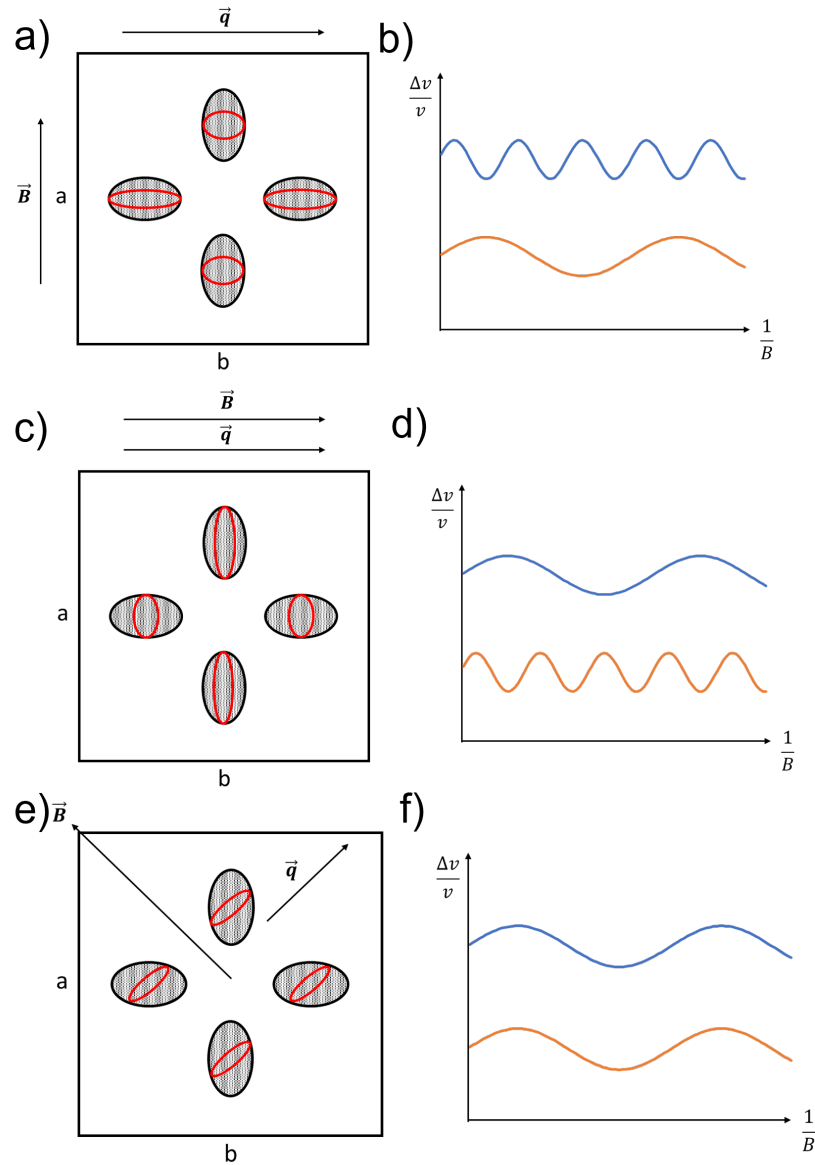
FIGURE 3.2: a) Simple schematic of the Fermi surfaces with the magnetic field parallel to the current. The red ovals are the contributions of the Fermi surface to the wave forms. b) The plot of the different oscillations when the field is parallel to the current. c) The Fermi surface contributions when the field is perpendicular to the current. d) The sound velocity vs the inverse magnetic field when the field is perpendicular to the current. e) The contributions when the field is parallel to the current in the (110) direction. f) The corresponding oscillations for the field and current in the (110) direction.

surfaces allowing the current to propagate in the [110] direction (Figure 3.3). Only one transverse transducer was glued onto the sample in order to take reflectance measurements. A thin gold wire was attached to each contact of the transducer using silver paint. The sample is then glued down to the probe's sample holder using silicone glue. Each wire is soldered onto their designated pin on the sample

holder using indium (it has a lower melting point which allows us to solder the wires without melting them).

The transducer was oriented so that the polarization of the sound waves was along the z-axis. As discussed in the previous chapter, this gives access to an acoustic mode that probes uniquely the C_{44} element of the elasticity tensor.
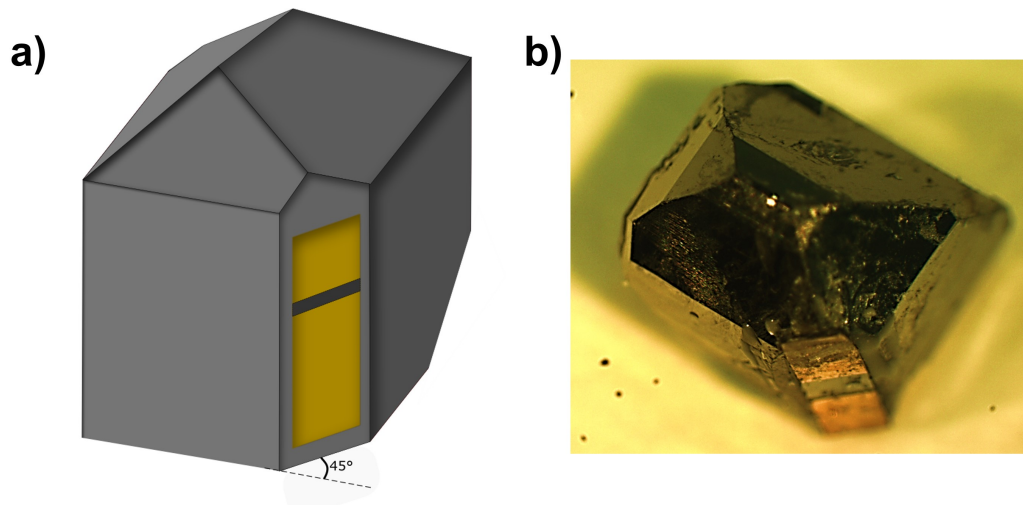
FIGURE 3.3: **a)**Schematic of the NbP sample prepared for ultrasound measurements. The visible polished flat surface has a transducer glued to it. There is another polished surface opposite of the visible one. **b)**Picture of the sample used for ultrasound measurements.

3.2   Experimental setup

3.2.1   Cryogenic apparatus

Measurements are done using a variable temperature insert (VTI) inside of a ^{4}He cryostat. This device allows us to take measurements at very low temperatures (down to roughly 2 K) with the help of liquid helium (LHe). Liquid nitrogen (LN$_2$) is also employed to fill a reservoir surrounding the liquid helium space which helps to precool the system and reduce the evaporation rate of the LHe. It is more effective to employ the cold gas evaporating from liquid helium and utilise its enthalpy for chilling the experiment for measurements above 5 K than it would be to use the main ^{4}He bath [45]. Helium flows from the main ^{4}He bath through a

capillary into the probe space of the VTI which is otherwise isolated by a vacuum space. Pumping on the VTI space ensures a continual flow of helium into the VTI. The flow rate, and therefore cooling power and temperature of the experiment can be controlled with the help of a needle valve. An automated system controls both the needle valve position (with a stepper motor) and applies an appropriate amount of heat to control the temperature of a resistive thermometer which is measured using a resistance bridge and temperature controller [45]. This design allows for low helium consumption, fast cooling and warm-up times and excellent temperature stability.

In practice, our sample is loaded into a probe, that includes an automated rotator, thermometer and necessary coaxial cables. This probe is contained within a hermetically sealed tube in which a small amount of helium gas is injected. The tube is then inserted into the VTI.

Surrounding the VTI and thermalized to 4.2 K in the main He-bath is a superconducting magnet in principle capable of producing magnetic fields up to 16 T (18 T if one pumps on the cryostat to further lower the magnet's temperature). In practice, we have maintained magnetic fields under 15 T in order to avoid possible quenches of the magnet that can occur when approaching the upper limit.

3.2.2 Ultrasound spectrometer
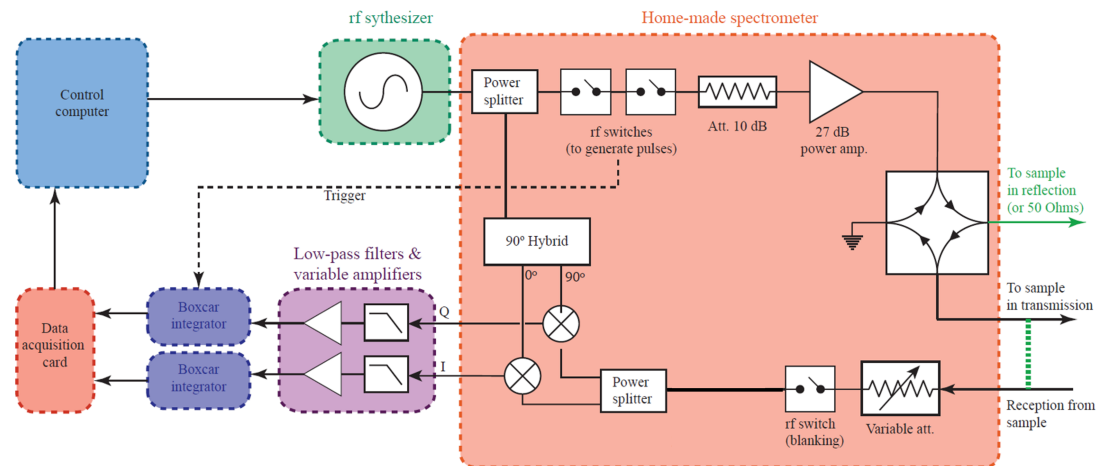
FIGURE 3.4: Ultrasound spectrometer schematic.

There are many components to an ultrasound spectrometer that are necessary for collecting data as illustrated in the schematic of Figure 3.4. First, an rf synthesizer is used to produce a continuous sine wave. This establishes the carrier phase and frequency. The signal is then split into two channels using a power splitter. One of the channels passes through rf switches that turn the power on and then off with the aim of generating mostly square pulses typically $\sim$ 150ns long. The pulses are then attenuated by 10 dB and amplified by 27 dB, giving a total amplification of 17 dB.
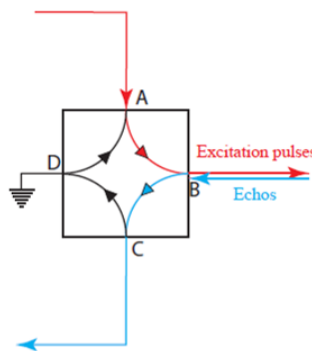
FIGURE 3.5: Hybrid junction used for ultrasound measurements.

The pulses then make their way through a hybrid junction. The excitation pulses make their way through port A of the junction, and exit through port B without affecting port C. The echoes then enter port B and exit through port C towards the receiver without having an effect of port A. This is a form of "duplexer" or "transmit-receive circuit".

Once the pulses pass through the hybrid junction, more attenuation and amplitude adjustments must be made to obtain an ideal signal amplitude to work with.

The next step is that of phase and quadrature detection. The echoes need to be mixed with the synthesizer carrier-wave with two different phases. The echoes pass through the power splitter, and the carrier wave is further split, and one of the channels is dephased by 90°. In other words, we are left with a $\cos{(\omega t)}$ on one line (in-phase) and a $\sin{(\omega t)}$ on the other line (quadrature). The mixers therefore

multiply two voltages together. Consequently, if the input signal is given by:

$$f(t)\cos(\omega t + \phi)$$

where ω is the carrier frequency, ϕ is the phase with respect to the synthesizer, and $f(t)$ is the modulation (the shape of the echo), we get the following after the mixers:

$$I(t) = f(t)\cos(\omega t + \phi)\cos(\omega t) \quad \text{and} \quad Q(t) = f(t)\cos(\omega t + \phi)\sin(\omega t) \quad (3.1)$$

on the two channels I (in-phase) and Q (quadrature). We can see that this result in a high-frequency signal at 2ω (which is filtered by the subsequent low-pass filters) and a slowly varying (on the span of μs) envelope $f(t)$ which switches from one channel to the other, depends on the phase.

There is still some further optimal amplification of these two signals, after the low-pass filters. Then the signals are fed into the boxcar integrators which integrate the signal over a window of time. This window of time is usually selected over one echo. The echo that is chosen must show a nice clear signal and should not overlap other echos. The integrated signals are then averaged over a certain number of pulses. They are then sent to the data acquisition card which is read out by the LabView program.

Since the phase of the signal is given by:

$$\phi = \frac{\omega x}{v}$$

it is easy to determine that:

$$\frac{d\phi}{\phi} = \frac{d\omega}{\omega} - \frac{dv}{v}$$

assuming that x (the length of the sample) does not have large variations. Therefore, if the phase is fixed, relative changes in frequency will be equal to relative

changes in velocity. We then have:

$$\frac{d\omega}{\omega} = \frac{dv}{v} \qquad\qquad (3.2)$$

In order to fix the phase, we measure at a series of frequencies (typically 3 to 5 frequencies) and look at the magnitude of the Q (quadrature) channel which will be proportional to $\sin(\phi)$. If we start at $\phi \simeq 0$ and we do not vary the frequency too much, we should obtain a linear relationship, i.e.

$$Q \propto (\omega - \omega_0)$$

where ω_0 is the frequency at which the phase is nulled. Doing a linear fit of these points allows us to determine ω_0. With a feedback loop we can carry out this procedure with our measured frequencies centred around ω_0, and saving the value of ω_0 in a table. Since this is always the frequency at which the phase is equal to zero, relative changes in frequency will follow relative changes in sound velocity. As long as the sound velocity does not change too rapidly, it is possible to track the zero-phase condition and obtain a measurement of the relative change of velocity. In practice, this often allows us to obtain a precision of 10^{-6} on the sound velocity. This is a result of the fact that we are doing an interferometry measurement comparing the phase of the synthesizer to the phase of the resulting echoes.

The signal amplitude $I(\omega_0)$ is also saved in order to look at how changes in the magnetic field or temperature lead to an attenuation of sound within the material.

3.3   Results

In this section, I will present our sound velocity results on NbP, beginning with a rough determination of the absolute sound velocity, and then moving on to more precise measurements of relative changes in sound velocity as a function of temperature and magnetic field. In order to obtain a full analysis of the quantum

oscillations and possible indications of a chiral anomaly, as measured by sound velocity, it was necessary to take measurements with the magnetic field oriented both in the *ab*-plane (varying the azimuthal angle ϕ) and out-of-plane (varying the polar angle θ).

3.3.1 Absolute Velocity Calculation

The pulsed-echo ultrasonic interferometer can be used to determine relative or fractional changes in velocity of the acoustic waves through the sample, that is $\Delta v/v$. As mentioned previously, this can be done by adjusting the frequency in order to maintain a constant phase of a specific echo. Relative changes in frequency are equal to relative changes in velocity, $\Delta\omega/\omega = \Delta v/v$. In practice, these relative changes are usually quite small at low temperatures.

To obtain the absolute velocity v of the sound waves, for example to compare with theoretical values calculated with density functional theory, one must measure the position in time of the first echo, or else measure the time difference between echos.

The theoretical value of the velocity of the acoustic waves is given by:

$$v_{44} = \sqrt{\frac{C_{44}}{\rho}} \tag{3.3}$$

where C_{44} is the elastic constant of NbP and ρ is the density of NbP. From [46], we expect that C_{44}=111.9 GPa and we also know that ρ=6.52 g·cm^{-3}. Plugging this into 3.3, we obtain:

$$v_{44} = \sqrt{\frac{11.19 \times 10^9 \text{ g} \cdot \text{cm}^{-1}\text{s}^{-2}}{6.52 \text{ g} \cdot \text{cm}^{-3}}} \tag{3.4}$$

$$v_{44} = 4.14 \text{ km/s}$$

Now we must find the experimental value. This can be found using the following equation:

$$v_{44} = \frac{2L}{\frac{1}{\Delta f_a} - \frac{1}{\Delta f_b}} = \frac{2L}{\Delta t} \tag{3.5}$$

where L is the length of the sample and Δt is measured using the technique explained above. We know that $L=(4.00 \pm 0.04) \times 10^{-3}$ m and from observing a specific echo we find that $\Delta t=(2.1 \pm 0.2) \times 10^{-6}$ s.

We can therefore find the value of v_{44}.

$$v_{44} = \frac{2(4.00 \times 10^{-3} \text{ m})}{2.1 \times 10^{-6} \text{ s}} \tag{3.6}$$

$$v_{44} = (3.81 \pm 0.4) \text{ km/s}$$

The experimental value obtained for the velocity of the acoustic waves is given by 3.81 km/s. This gives us an error of 7.97%. Taking into consideration the uncertainty caused by the difficulty to locate the exact position of the echo, our answer is very close to the theoretical value calculated above.

While our measurements of the absolute value of the sound velocity is not precise, we can obtain extremely precise measurements of the relative changes $\Delta v/v$ using the phase-nulling feedback method described above. In the rest of the thesis, we will just present relative changes, $\Delta v/v$, as a function of field and temperature.

3.3.2   In-Plane Measurements
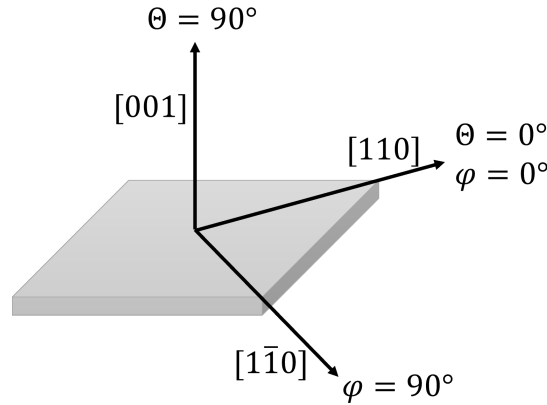
FIGURE 3.6: Definition of the various orientations of the sample. The gray prism represents the ab-plane. θ represents the angle definitions in-plane and φ represents the angle definitions out-of-plane.

In-plane measurements are done with the magnetic field rotating within the *ab*-plane. Measurements at [110] are labeled as $\phi = 0°$ and measurements at [1$\bar{1}$0] are labeled as $\phi = 90°$. A schematic of the angle definitions that we have adopted can be seen in Figure 3.6.

3.3.2.1   Angle Sweeps

When gluing the sample to the rotator probe, it is possible to have a misalignment of several degrees. In order to obtain the true orientation of the sample in the ultrasound probe, angle sweep measurements must be taken at a fixed magnetic field. We expect these results to show a symmetry about certain crystallographic orientations. For instance one these points of high symmetry is expected at $\phi = 45°$ in the rotator's convention (when $\vec{q}$ and $\vec{B}$ are expected to be parallel). Locating this point will help determine the true alignment of the sample in the probe. These measurements were taken with a magnetic field of 2 T because this is where some of the large changes can be observed. These measurements can be seen in Figure 3.7. The symmetry point determined by finding the maximum of the curve and indicated by the red arrow is located at 52.1°. This value is expected to be 45° in the rotator's coordinates. This tells us that the true angle at which the field

is aligned with [110] is given by 7.1°. This value allows us to determine which orientation to position our sample in for the next measurements.
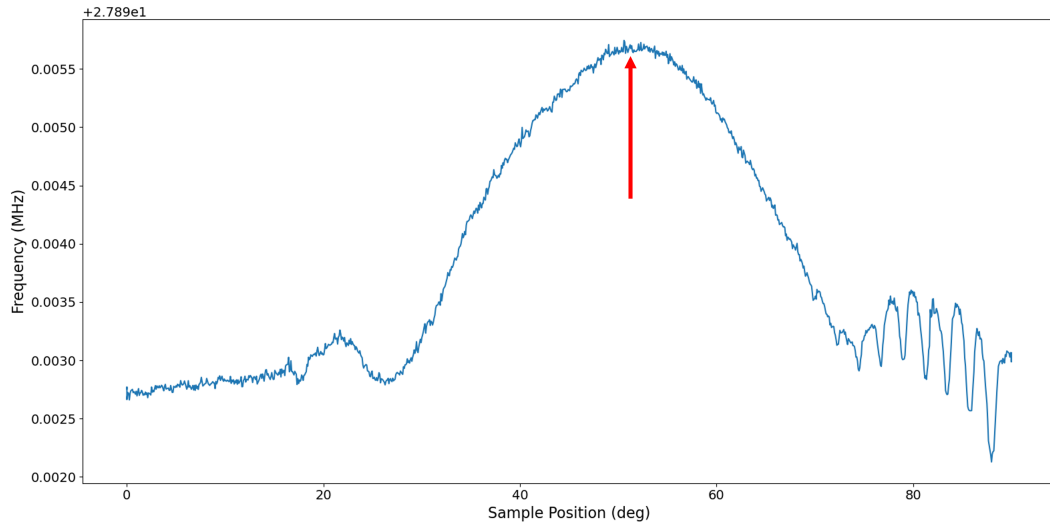
FIGURE 3.7: The variation of the frequency as a function of the angle of the sample for measurements with the magnetic field in-plane. The red arrow indicates the symmetry point of the data. Oscillations at 70° and above are likely artefacts resulting from heating of the sample caused by the movement of the rotator.

3.3.2.2   Field Sweeps

Since the primary goal of this project is to explore the effects of magnetic field, as a method of searching for the chiral anomaly and exploring quantum oscillations, we have performed field sweep measurements at various angles. We expect in-plane measurements to be particularly important for showing evidence of the chiral anomaly, which would reduce the symmetry from 4-fold to 2-fold. Field sweep measurements at various angles allow us to observe how quantum oscillations change at different orientations of the sample, thereby mapping out the Fermi surfaces of the material. Multiple measurements were taken at each angle to ensure repeatability. Data was collected with the magnetic field sweeping up from 0 T to 14 T and with the field sweeping down from 14 T to 0 T. These curves were then averaged to take into consideration the hysteresis that occurs between increasing and decreasing magnetic field. The raw data collected for measurements of the variation of the magnetic field can be seen in Figure 3.8.
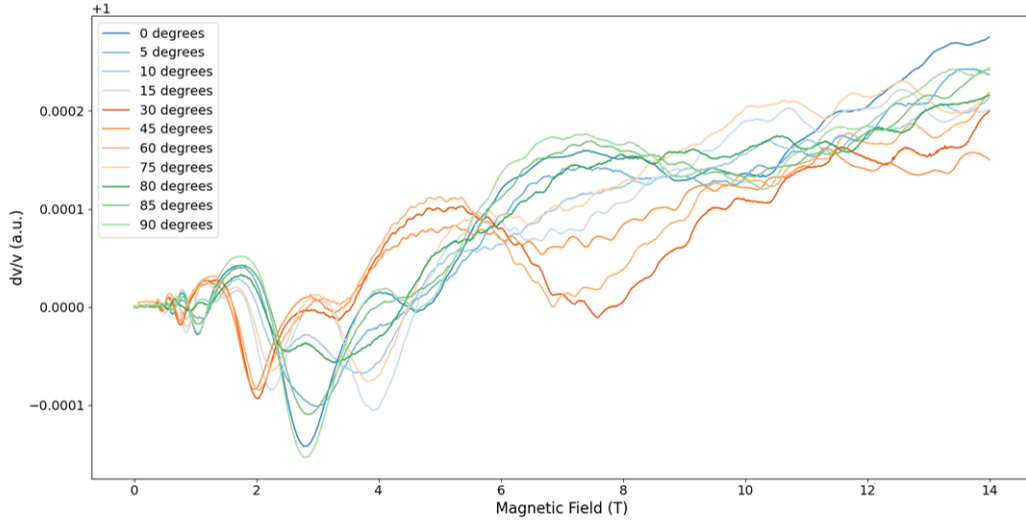
FIGURE 3.8: Variation of the relative change in velocity as a function of the magnetic field for measurements taken in-plane.

As it can be seen, many pairs of curves have similar shapes. For example the 0° and 90° are similar, 5° and 85° curves have similar quantum oscillations, the 10° and 80° curves are similar, the 15° and 75° curves are similar, and the 30° and 60° curves have the same oscillations. This indicates a symmetry about 45° as is normally expected for a tetragonal structure.[1] However, the chiral anomaly is thought to break the tetragonal C_4 symmetry of the lattice in applied magnetic and electric fields, reducing it to a 2-fold symmetry. Therefore we would expect to see a difference between the curves at 0° and 90°. A comparison of the data collected at both 0° and 90° can be seen in Figure 3.9. As can be seen, the difference between both curves is very small and is not enough to say it is caused by the chiral anomaly.

Therefore, these measurements, in contrast to those carried out by Laliberté *et al.* [26] on TaAs, show no clear evidence of the chiral anomaly. We cannot prove that it does not exist in NbP as it may simply appear as a difference that is too small to observe in our measurements. Multiple measurements were taken at each angle to show that this difference was reproducible (Figure A.1 in Appendix A). There could be several possible explanations for this discrepancy. First it may be that having Weyl nodes of opposite chirality enclosed within the same Fermi surface in

---

[1]Recall that we have corrected the angle for misalignment of the rotator's coordinates.

NbP does away entirely with the chiral anomaly. Alternatively, the differences in electronic structure and sample purity between TaAs and NbP may simply lead to a different magnitude of the chiral anomaly as seen by sound velocity. The effect was already quite small in TaAs (of the order of 1 part in 10^4). If material details reduced its effect by an order of magnitude in NbP, it would be imperceptible in our data.
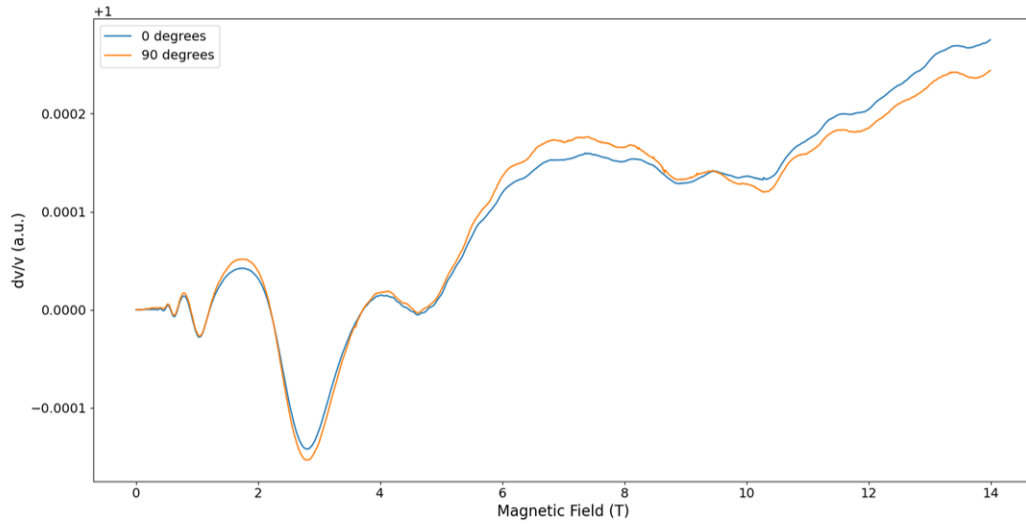
FIGURE 3.9: Comparison between the measurements taken at 0° and 90°

The most evident feature of the data is the presence of oscillations. Once the raw data is collected it is then plotted as a function of the inverse magnetic field (Figure 3.10). From this figure we can see clean oscillations with equal distances between them (i.e. a well defined periodicity). This demonstrates clearly that these are quantum oscillations, not unlike Shubnikov-de Haas (SdH) or de Haas-van Alphen (dHvA) oscillations. These plots allow us to extract the oscillation frequencies of the sample that correspond to different Fermi surfaces.
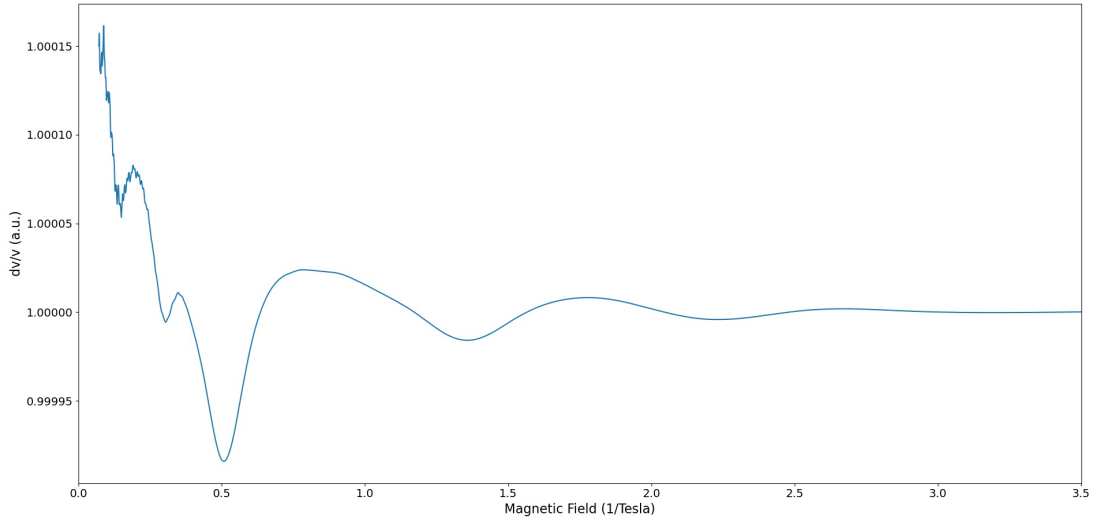
FIGURE 3.10: The changes of sound velocity as a function of the inverse magnetic field.

In order to obtain the various quantum oscillation frequencies of NbP that are visible for in-plane ultrasound measurements, we take a fast Fourier transform (FFT) of the data seen in Figure 3.10. A Fourier transform is performed on each data set to see how the oscillation frequencies change at various orientations of the sample. When looking at Figure 3.11, we can see that there is a symmetry of the data around 45° which is expected for tetragonal structures. Moreover, we are not aware of a reason to expect the chiral anomaly to affect the frequency of quantum oscillations, which simply results from the cross-sectional area of the Fermi surface. It can also be noted that this symmetry is an indicator of the excellent alignment of the sample, since a small out-of-plane alignment should give rise to a noticeable change in oscillation frequency. Peaks can also be seen at higher frequencies in Figure A.2 in Appendix A.
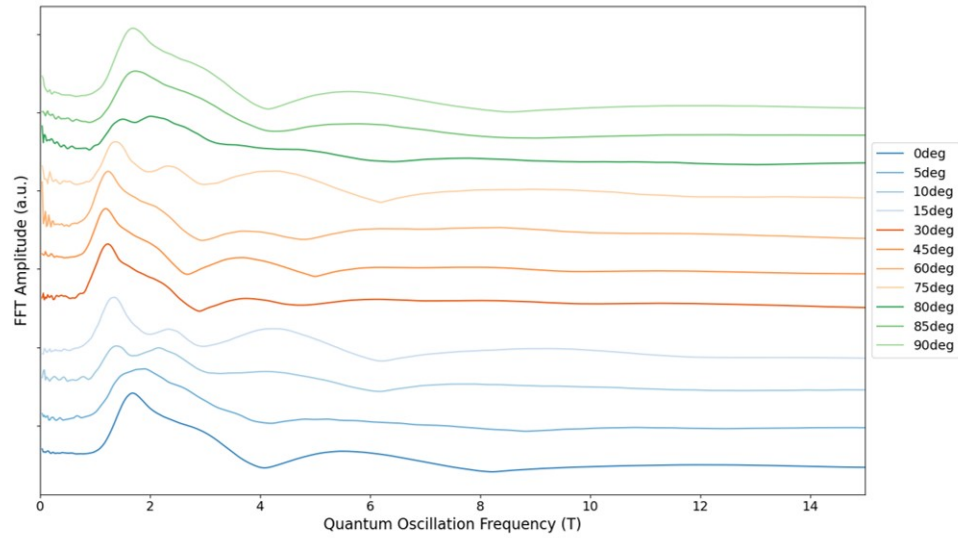
FIGURE 3.11: Evolution of the quantum oscillation frequencies at various orientations of NbP for in-plane measurements at lower oscillation frequencies. The curves are staggered for ease of viewing.

Figure 3.12 shows a closer look at the Fourier transform of the measurements taken at 0° and 90°. Both curves have the same oscillation frequencies with very similar FFT amplitudes. This, once again, further emphasizes that more measurements must be done on NbP to try to observe signs of the chiral anomaly. This is not an indication that the chiral anomaly is not present in niobium phosphide. It simply indicates that NbP's complex electronic structure creates many contributions to the sound velocity measurements that could be overwhelming the expected chiral anomaly results.
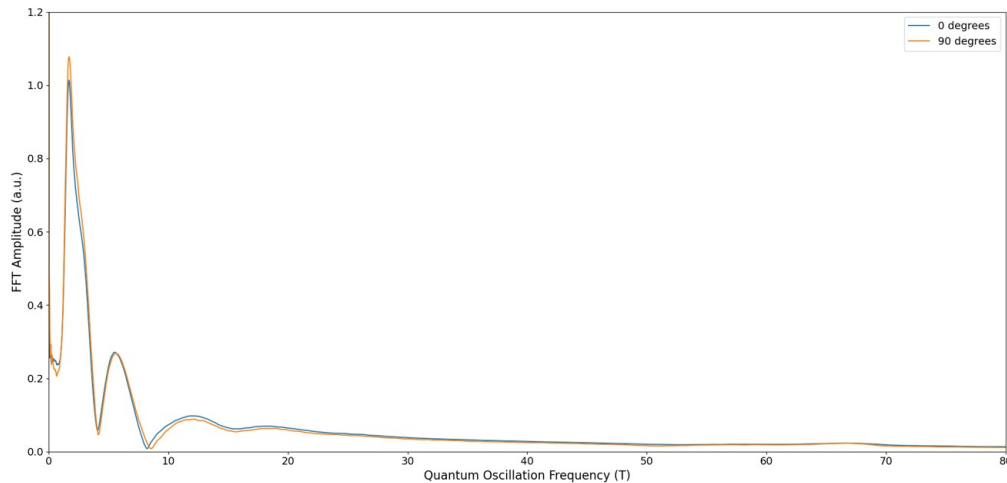
FIGURE 3.12: Comparison of the fast Fourier transform taken at 0° and 90°.
Both results are very similar.

3.3.2.3   Frequency dependence

All the previous data collections were done at a frequency around 24 MHz which is
the fundamental resonant frequency (or first harmonic) of the transducer. Nomi-
nally, the transducers should have a resonant frequency of 30 MHz, but when glued
to the sample and loaded with wires attached with silver epoxy, the resonant fre-
quency is often somewhat reduced. Our primary measurements were done at the
first harmonic because it gave the strongest signal and the clearest echoes. It was
also possible to see echoes at the third harmonic of the transducer (86 MHz). By
taking measurements at this frequency, we are able to compare the results obtained
at both harmonics and check the frequency dependence of our measurement. If
they are both consistent with each other, this is a good indication that the results
obtained are valid and fully representative of intrinsic physics within the sample.
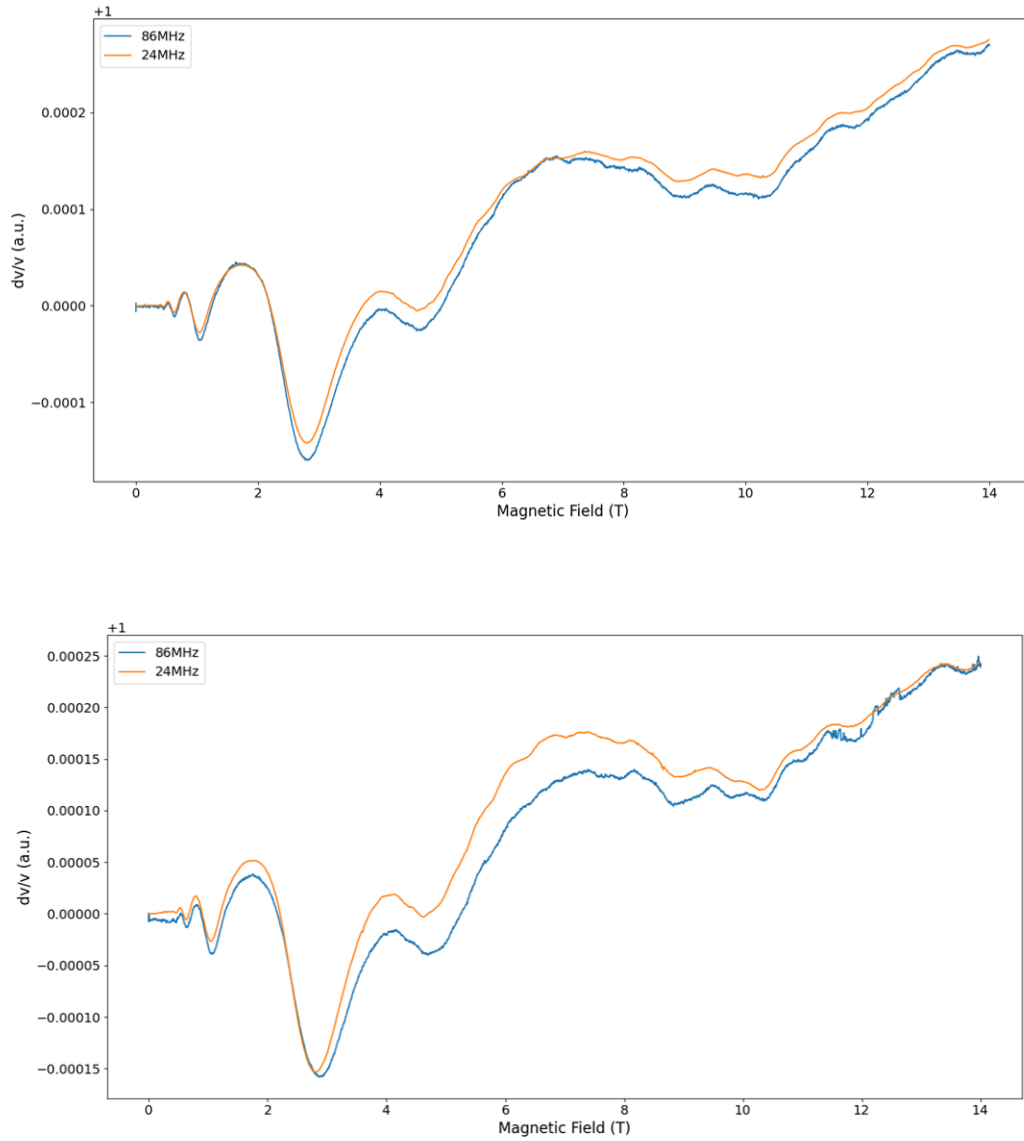
FIGURE 3.13: Comparison of the first harmonic and third harmonic resonant frequencies of NbP in ultrasound measurements.**Top**: Data collected with the magnetic field at $0°$ with regards to the current. **Bottom**: Data collected with the magnetic field at $90°$ from the current.

From Figure 3.13 we can see that the results obtained at both frequencies are comparable. They both have the same quantum oscillations at the same position and generally look very similar. There does appear to be a slight difference in magnitude between the results at these two frequencies, but nothing that would suggest major problems with interpretation of our data.

Since the results obtained at both frequencies are comparable, we can be confident that our results are valid, that the transducers are well placed and that we have

selected isolated echos free of interference problems. Echoes could also be seen around 120 MHz, however the signal to noise was too small to obtain clear results.

3.3.2.4 Temperature dependence

Magnetic field sweeps were done on the sample at various temperatures ranging from 2 K to 20 K. These field sweeps allow us to observe how the quantum oscillations change as the temperature increases. These measurements were performed at three different orientations of the sample (0°, 45° and 90°).
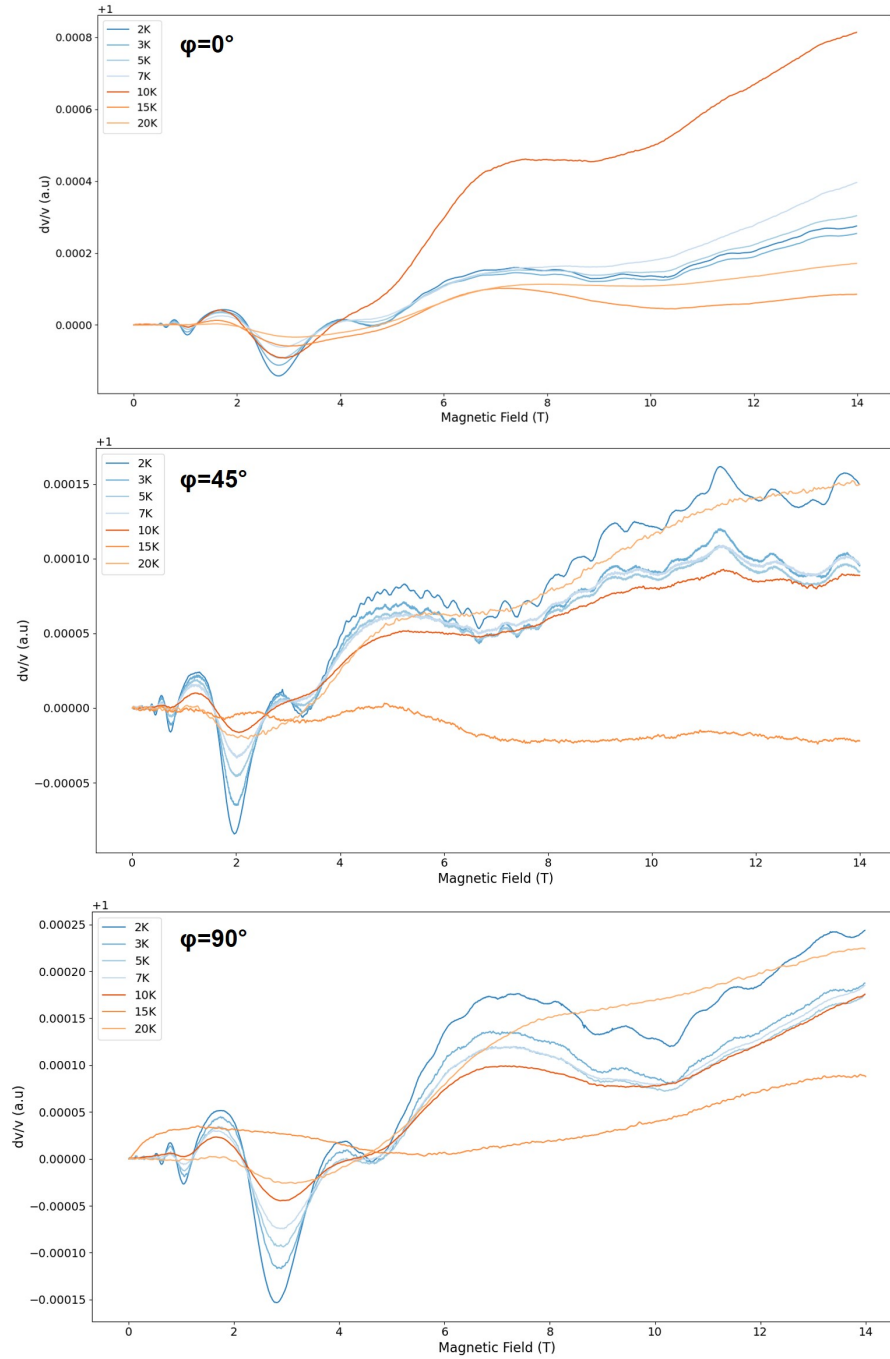
FIGURE 3.14: Variation of frequency as a function of the magnetic field at different temperatures. **Top**: Measurements taken with the field parallel to the current. **Middle**: Data collected with the magnetic field at 45° from the current. **Bottom**: Data collected with the magnetic field perpendicular to the current.

As expected, we can see from Figure 3.14 that the amplitude of the oscillations decreases as the temperature is increased, which is qualitatively consistent with the thermal damping factor in the Lifshitz-Kosevitch formalism [22]. However,

when looking at the measurements taken at 0°, we can see that the measurements at 10 K are not entirely consistent with the rest of the data. This once again occurs at 15 K and 20 K for the measurements taken at 45° and 90°. When collecting the data, we discovered that it was very difficult to obtain clean results at higher temperatures due to a degradation in the signal. It often took many attempts for measurements above 10 K before obtaining usable results. We can therefore deduce that the data collected at higher temperatures might not be completely accurate. The likely cause of this problem is that the overall sound velocity varies much more significantly as a function of temperature than as a function of magnetic field. This can lead to significant phase changes and even shifting of echo positions that make it difficult to maintain the same spectrometer settings for all temperatures. To obtain better results, we would likely have to optimize the spectrometer parameters (in particular the choice of initial frequency and the position of the boxcar integrators) at each temperature before launching a field sweep. This would be quite a laborious process and was not seen as a priority for this project.

In practice, this appears to lead to a strong change in background as the temperature is increased. A Fourier transform can nonetheless be applied to the data collected at each temperature in an attempt to observe whether the oscillation frequencies change with an increase in temperature and in particular to observe changes in amplitude of the oscillations.
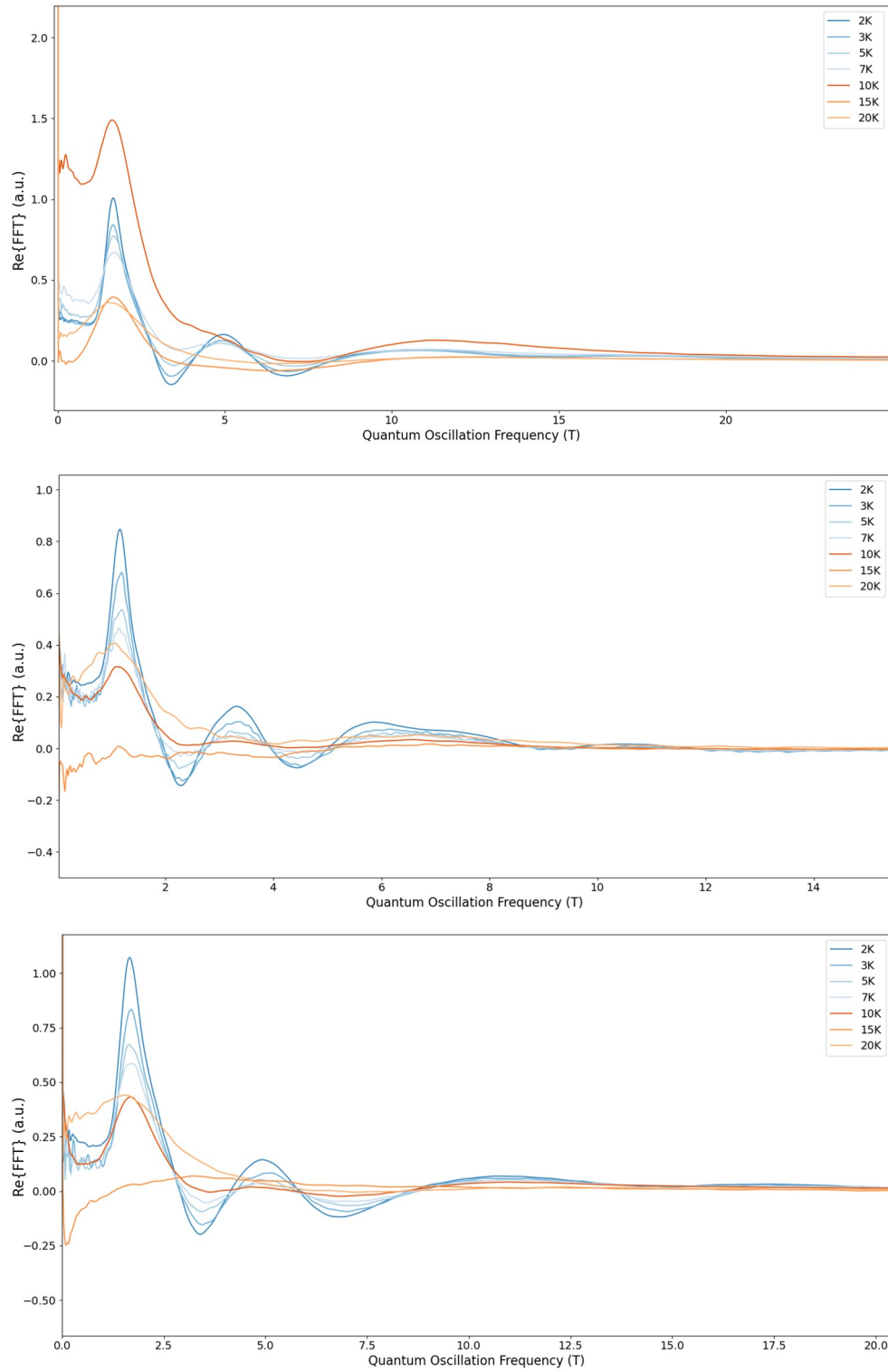
FIGURE 3.15: The variation of the oscillation frequencies as a function of the temperature after a Fourier transform when: **Top** the magnetic field is parallel to the current. **Middle** the magnetic field is at 45° from the current. **Bottom** the magnetic field is perpendicular to the current.

We once again see that the oscillations decrease in amplitude as the temperature increases. The same discrepancies occur as in Figure 3.14. The amplitudes of the oscillations in Figure 3.15 can in principle be used to determine the effective mass of the sample. However, I was unsuccessful in extracting the effective mass from the temperature dependence of the ultrasound data. Again this is likely because there is a significant change in background and data quality as the temperature is increased, making it very difficult to precisely follow the oscillation amplitude in temperature. This change in background can be seen in Figure 3.14.

3.3.3 Out-of-Plane Measurements

In-plane measurements are the ideal approach to look for the chiral anomaly, since we can probe the configurations where $\vec{q} \perp \vec{B}$ and $\vec{q} \parallel \vec{B}$ with the field along crystallographically equivalent directions. On the other hand, in order to best characterize the quantum oscillations in NbP, it is important to study the significant anisotropy between in-plane and out-of-plane magnetic fields. Indeed, previous sound velocity measurements in TaAs [26] showed a sensitivity to different types of pockets depending on whether the field was oriented parallel or perpendicular to the *c*-axis. More precisely, oscillations from a trivial hole pocket were particularly evident in the data when the field was in the plane, whereas a topological Weyl pocket gave rise to the dominant signal as the field was rotated out of the plane.

Out-of-plane measurements were done with the magnetic field rotating out of the *ab*-plane. Measurements at [110] are labeled as $\theta = 0°$ and measurements at [001] are labeled as $\theta = 90°$. A schematic of the angle definitions can be seen in Figure 3.6.

3.3.3.1 Angle Sweeps

Once again, angle sweeps were taken to correctly identify the sample orientation by looking for points of high symmetry. First an angle sweep from 100° to 0° was taken

in hopes of finding a high symmetry point, but no symmetry point was visible. When observing the angle sweep we noticed that a large dip in frequency occurred around 0° which could be an indication of a high symmetry point. Another angle sweep was then performed from -10° to 5° and it was found that the symmetry point was located at -1°. This point corresponds to the point where the sample is positioned at [001]. For consistency with our previous data, the symmetry point corresponds to 90° since it perpendicular to the plane, and therefore perpendicular to the current. The true value of absolute zero is therefore taken as 89° when the field is positioned at [110]. Note that at 14 T (Figure 3.16a) this point corresponds to a minimum, but at 9.8 T (Figure 3.16b) it gives a maximum.
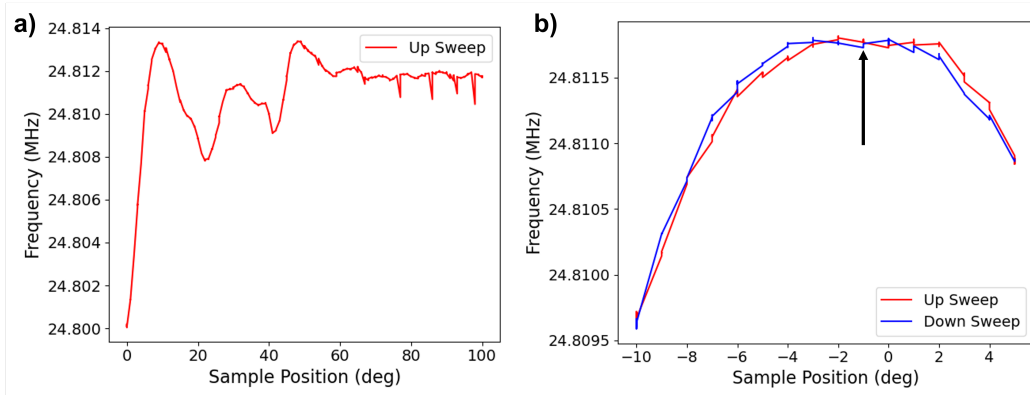
FIGURE 3.16: **a**): Frequency as a function of the sample position from 100° to 0° at 2K with a magnetic field at 14T. **b**): Frequency as a function of the sample position from -10° to 5° at 2K with a magnetic field at 9.8T. The arrow corresponds to the position of the symmetry point. Recall that changes in the measurement frequency (with constant phase) are proportional to changes in sound velocity.

3.3.3.2 Field Sweeps

Following the same procedure as was mentioned in Section 3.3.2.2 we can obtain clear data when measuring changes in velocity as a function of the magnetic field for different sample positions rotating out of the plane. Figure 3.17 shows the quantum oscillations visible at different sample positions. We can see that the shape of the curve obtained at 0° (parallel to the current) resembles the curves obtained for our previous in-plane measurements. This indicates that the symmetry point found in our angle sweeps was correct.
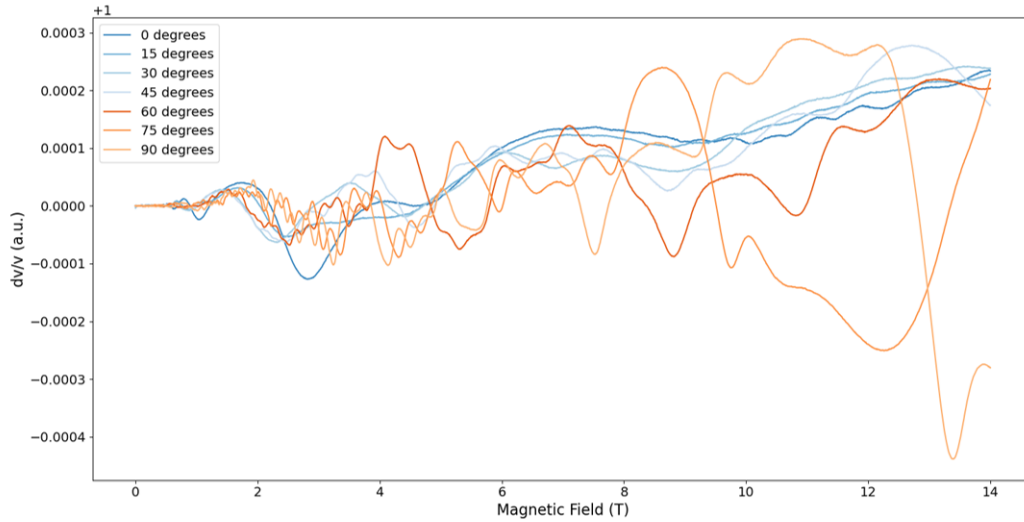
FIGURE 3.17: The relative change in velocity as a function of the magnetic field as the NbP sample is rotated out-of-plane.

When taking a closer look at the data collected in the [110] direction (0°) and [001] direction (90°) we can see that there is a very big difference between the two curves (Figure 3.18). We can see that there are many more quantum oscillations visible with the field out-of-plane than in-plane. We can see that the oscillations also have a much larger amplitude for measurements out-of-plane than those in-plane. This large difference between both curves is the reason why the project focused on in-plane measurements. The symmetry seen in-plane and the less complex data makes it easier to observe different phenomena that could occur such as the chiral anomaly.
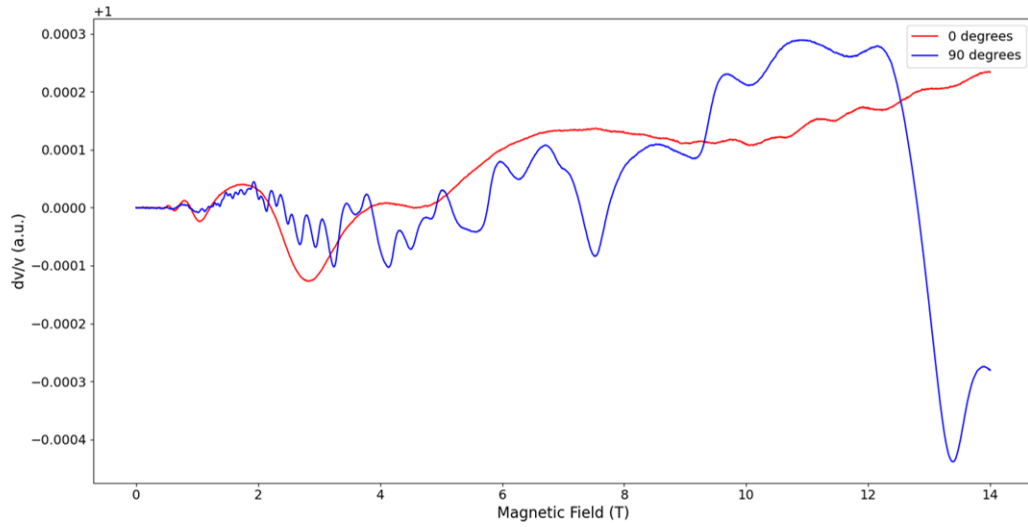
FIGURE 3.18: Comparison between field sweeps taken at 0° and 90°

The Fourier transform is then taken to determine the different oscillation frequencies that are visible. Because of the many quantum oscillations visible in Figure 3.17, it is expected that the Fourier transform show many more peaks when the sample is rotated out-of-plane. This is what we observe in Figure 3.19.
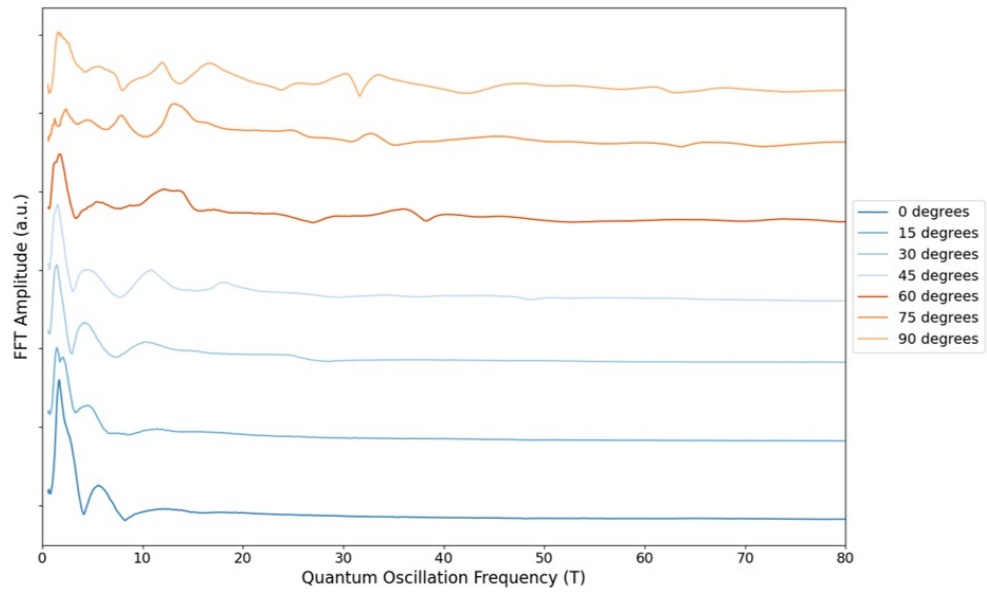
FIGURE 3.19: Evolution of the quantum oscillation frequencies of NbP as the magnetic field is rotating out-of-plane. The curves are shifted for ease of viewing.

For measurements close to the plane (below 30°), only low oscillation frequencies are visible. The closer we get to [001], the more oscillation frequencies are visible and the more complex the results become. There is no visible symmetry seen within the results collected with the field rotating out-of-plane unlike what was seen for the in-plane results. This is normal given the anisotropy of a tetragonal system. Evidently, as we rotate the field towards the c-axis, our measurement becomes sensitive to additional Fermi surfaces that are not seen for in-plane measurements, leading to a more complicated Fourier transform.

3.3.3.3   Temperature dependence

Again, field sweeps were done at different temperatures to see if the out-of-plane measurements behaved similarly to the in-plane measurements. Only three different temperature measurements were taken due to time constraints. The measurements were all taken with the magnetic field pointed in the [001] direction. from Figure 3.20, we can see that the amplitude of the oscillations decreases as the temperature increases like what was seen for in-plane measurements. It can also be seen that the smaller amplitude and higher frequency oscillations start to disappear at 10 K, and we are mostly left with the larger amplitude, lower frequency oscillations. This implies a higher effective mass for the high-frequency oscillations.
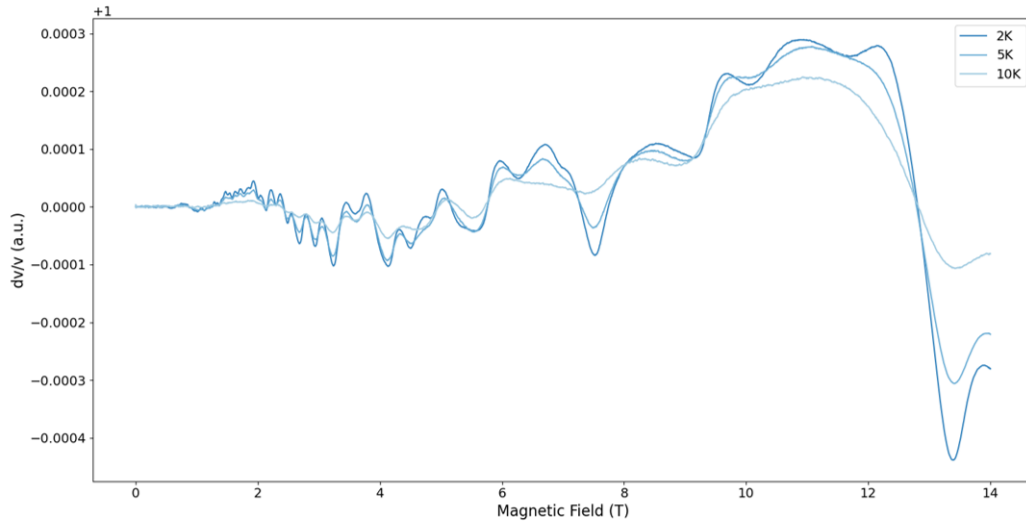
FIGURE 3.20: d

irection]Relative changes in sound velocity as a function of the magnetic field at different temperatures with the magnetic field oriented in the [001] direction.

When taking the Fourier transform of the temperature measurements (Figure 3.21), we see the same decrease in amplitude of the peaks that was seen for the in-plane measurements. It can also be seen that the oscillations above 40 T seem to completely disappear once at 10 K. From these results, we can predict that most of the oscillations would flatten out and disappear at temperatures above 20 K.
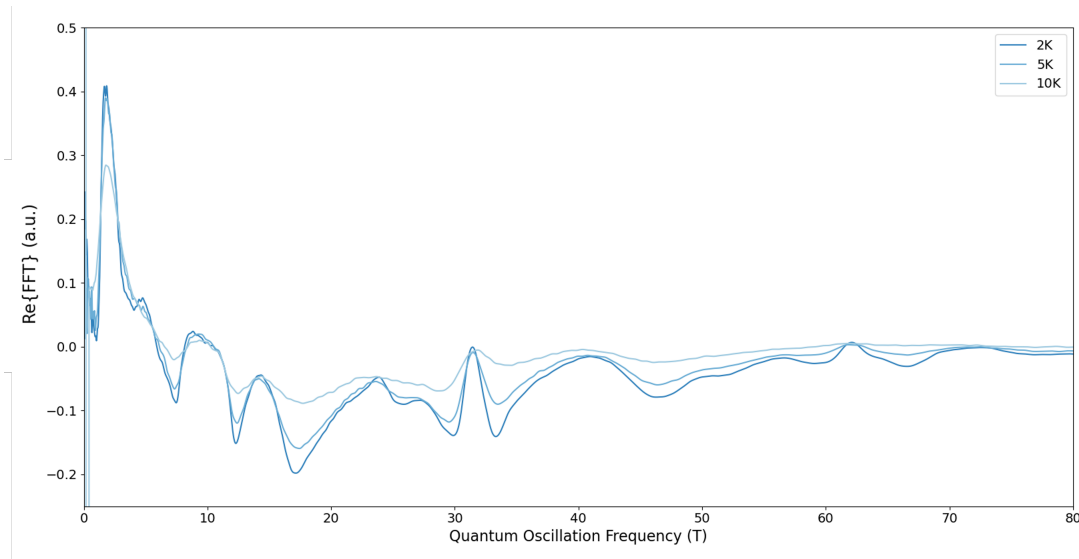
FIGURE 3.21: The variation of the oscillation frequencies as a function of the temperature after a Fourier transform with the magnetic field in the [001] direction

Effective mass calculations were not performed for the out-of-plane measurements due to only having data points at three different temperatures which is not enough points to fit equation 1.17 to the data.

3.3.4   Comparison with other ultrasound measurements

The sound velocity and attenuation of NbP has previously been measured by Schindler *et al.* [47]. While they have measured multiple acoustic modes and looked at particularly high magnetic fields (up to about 37 T) they have not done a full study as a function of field angle and have only considered $\vec{B}//\hat{c}$. Another difference to note between their work and ours is that the direction of sound wave propagation in their measurements is along [100] whereas for us it is always along [110]. However, a magnetic field applied along [001] does not break the tetragonal symmetry of the sample and therefore all measurements with polarization along [001] and sound propagation at any angle in the *ab*-plane should be related to the C_{44} element of the elasticity tensor and give rise to the same results. When the field is applied along a different direction, it can break the tetragonal symmetry of the system and lead to an anisotropy as a function of $\vec{q}$.
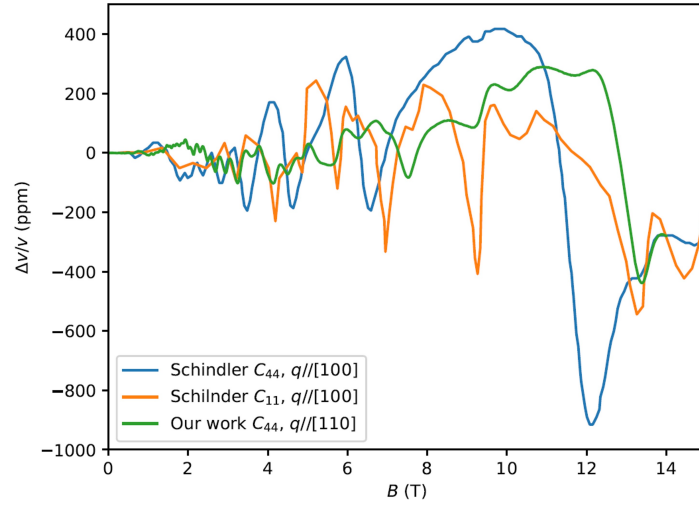
FIGURE 3.22: Comparison between our sound velocity data and digitized data of Schindler *et al.* [47] for $\vec{B}//[001]$.

In Figure 3.22 we show a comparison of our results (using mode C_{44} with $\vec{B}//\hat{c}$) with two of their curves (for the modes C_{11} and C_{44}), digitized to the best of our ability. As can be seen, the agreement is surprisingly poor. Of course this is particularly surprising when we are using the same mode C_{44}. We cannot attribute this difference to a mistake in our mode selection as a mistake in transducer polarization would likely select the mode C_{11} and this does not provide any better agreement.

We can also compare the oscillation frequencies extracted from our respective measurements, although it should be noted that Schindler *et al.* used Landau fan diagrams to determine the oscillation frequency whereas we used a Fourier transform. Nonetheless, we have found several frequencies that are equal, within the error bars, to frequencies found by Schindler *et al.* Other frequencies appear to be quite different, especially our lowest frequency of 1.5(1) T, which can be compared with their lowest frequency of 0.9(1) T, which they attribute to the β_2 orbit.

Both groups have carried out important consistency checks. Schindler *et al.* have obtained similar frequencies with multiple acoustic modes. Meanwhile, we have

obtained consistent results between different measurement frequencies and different echos. Thus there is little reason to assume that experimental errors are giving rise to the observed differences. Despite the discovery of some frequencies in common, it seems likely that the observed discrepancies can be attributed to a strong sample dependence.

TABLE 3.1: Comparison of quantum oscillation frequencies obtained for $\vec{B}//[001]$ ($\theta = 90°$) from our sound velocity measurements, and those of Schindler *et al.* [47].

Our work F (T)	Schindler F (T)
1.5(1)	0.9(1)
6.3(9)	6.81(7)
12.0(2)	14.74(4)
16.6(7)	
30.7(2)	30.89(5)
33.2(4)	31.7(5)
47.0(8)	42(1)
61.2(4)	
67.8(6)	

3.3.5 Association of frequencies with Fermi pockets

Since this is not the first experimental study of quantum oscillations in NbP, we can draw on other research groups' previous results in order to identify the various Fermi pockets that give rise to our observed oscillations. In order to give ourselves the best chance of comparing with other works, we first plot our Fourier transforms is such a way as to extract the most possible frequencies. For out-of-plane rotations we have achieved this by multiplying the FFT amplitude by the frequency. As can be seen in Figs. 3.23 and 3.24, this reveals a number of higher frequencies that have comparatively small amplitudes, but should nonetheless be taken into account.
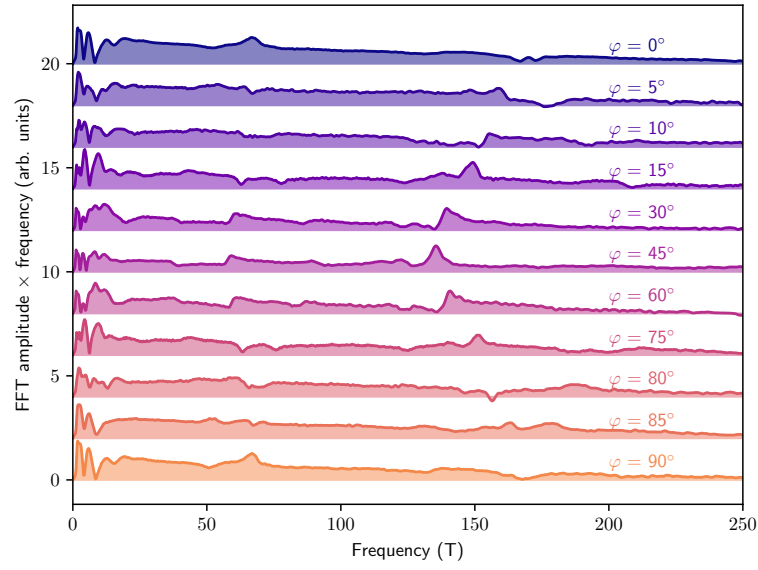
FIGURE 3.23: Zooming in on higher frequency peaks visible for in-plane rotations of the magnetic field.
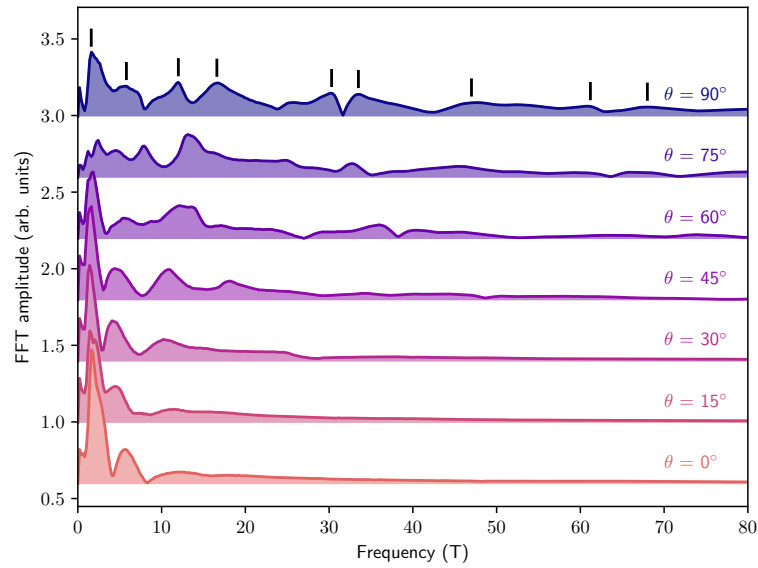
FIGURE 3.24: Plots of FFT amplitude multiplied by frequency to accentuate high frequencies for out-of-plane rotations.

Note that the different research groups with which we will compare our data have used different conventions for labeling the oscillations frequencies and Fermi pockets. These research groups have relied DFT calculations to identify the observed

frequencies. We will compare with 4 different groups whose labelling conventions are described as follows:

- Klotz *et al.* [28] carried out SdH measurements and Schindler et al. [47], as mentioned in the previous section, carried out ultrasound measurements. These two groups have used the same labelling convention: a Greek letter and a subscript. The subscript refers to the Weyl pocket and the Greek letter refers to one of the possible orbits of that pocket. For example α_1 signifies the α orbit of Weyl pocket number 1.

- Wang *et al.* [29] have carried out SdH and dHvA measurements, as well as Nernst and Seebeck effect measurements. Here we will quote their SdH and dHvA results. In their labelling convention, frequency F0 comes from the Weyl pocket 1 that they have named W1. This pocket in fact corresponds to Weyl pocket number 2 for other research groups. Conversely, frequencies F1 and F2 are associated with the Weyl pocket that they have named W2 but this is Weyl pocket number 1 for other researchers. The frequency F3 is associated with a trivial hole pocket.

- Sergelius *et al.* [27] carried out dHvA measurements. They have simply labelled their frequencies with Greek letters from α to θ. Sergelius *et al.* have also reported harmonics of certain peaks which are presented here (eg. 2δ, 2θ).

We will start with the magnetic field parallel to the *c*-axis, since this is the most commonly used configuration in the literature. A comparison of our frequencies with those of other groups is shown in Table 3.2. Here we show correspondence between certain measured frequencies by placing them on the same rows. Several frequencies appear to be well matched between multiple research groups, including ours. We can clearly associate several of our measured frequencies with the α_2, α_1 and γ_1 orbits. Other frequencies that we have measured match less well, but are not too far off either. It is likely we can attribute our frequency at 12 T to the β_1 orbit, and our 47 T peak to the δ_1 orbit. If we follow Wang et al. [29],

the 61.2 T peak is likely resulting from a trivial hole pocket. The peak at 1.6 T is not very well matched to other groups whose lowest frequency is around 0.9 T. Nonetheless, it is tempting to attribute the 1.6 T peak to the β_2 orbit. Finally, our measured peaks at 16.6 T and 68 T do not seem to correspond to any frequencies measured by other research groups and remain somewhat mysterious. Some peaks are attributed to harmonics by Sergelius *et al.* but to distinct orbits by other groups. For example a frequency around 12-14 T is attributed to the β_1 orbit by Klotz *et al.* [28] but is simply considered to be a second harmonic of the η orbit identified by Sergelius *et al.* [27] whose fundamental frequency is 6.6 T.

In Table 3.3 we show the same comparison for $\vec{B}//[100]$, that is $\theta = 0$, $\phi = 45°$. The sparsity of this table demonstrates the surprising lack of agreement between research groups for this field orientation. Our two lowest frequencies (1.24 and 2.2 T) might correspond to the β and γ orbits of Sergelius *et al.* [27], obtained using the dHvA technique. However the agreement is far from excellent. It appears that our 58.6 T peak likely equates to the F1a orbit of Wang *et al.*. They attribute this to Weyl node 2, which is considered Weyl node 1 by other research groups like Klotz *et al.*. The only truly convincing agreement, between our measurements and two other groups, is for our 135.3 T frequency which has been attributed to a trivial hole pocket (orbit F3b) by Wang *et al.*.

It is far from clear to us what is causing such poor agreement between measurements. It seems clear that the ultrasound measurements are particularly sensitive to lower frequency oscillations (the high frequency oscillations have orders of magnitude smaller signal). Meanwhile, the SdH technique seems (for this orientation of the sample) to only pick out rather high frequency oscillations (> 35 T). Evidently the dHvA technique is also quite sensitive to lower frequency oscillations. We would argue that the α frequency of Sergelius *et al.* is likely an artefact of the analysis as they do not appear to be covering a large enough range in $1/B$ to pick up such a low frequency. Some peaks may be harmonics. For example our 58.6 T peak might be a harmonic of the 31.7 T oscillation seen by Sergelius *et al.*. It seems surprising to not observe the fundamental, though Sergelius *et al.* do see a larger peak at the second harmonic.

TABLE 3.2: Comparison of oscillation frequencies for $B//[001]$ from our work (using sound velocity) from Klotz et al. [28] and Wang et al. [29] using the Shubnikov-de Haas (SdH) technique and from Sergelius et al. [27] using the de Haas-van Alphen (dHvA) technique. We have also included harmonics (2δ, 4δ) reported by Sergelius et al.. All frequencies are given in T.

Our work (Ultrasounds)		Schindler et al. (Ultrasounds)		Klotz et al. (SdH)		Wang et al. (SdH and dHvA)			Sergelius et al. (dHvA)	
Label	F (T)	Label	F (T)	Label	F (T)	Label	F (T) (SdH)	F (T) (dHvA)	Label	F (T)
β_2?	1.6(3)	β_2	0.9(1)						ξ	0.98
α_2	5.8(9)	α_2	6.81(7)	α_2	8.7	F0 (W1)	6.8	7.3	η	6.6
β_1?	12.0(2)	β_1	14.74(4)	β_1	14.6	F1 (W2)	13.9	12.3	2η	13.06
	16.6(7)									
α_1	30.3(2)	α_1	30.89(5)	α_1	32.1	F2 (W2)	31.8	31.0	θ	31.25
γ_1	33.5(4)	γ_1	31.7(5)							
δ_1?	47(1)	δ_1	42(1)	δ_1	39.6					
Hole	61.2(4)					F3 (Hole)	64.4	62	2θ	63.5
	68(1)									

TABLE 3.3: Comparison of oscillation frequencies for $B//[100]$ from our work (using sound velocity) from Klotz *et al.* [28] and Wang *et al.* [29] using the Shubnikov-de Haas (SdH) technique and from Sergelius *et al.* [27] using the de Haas-van Alphen (dHvA) technique. Each research group has adopted their own labelling convention. We have also included harmonics (2δ, 4δ) reported by Sergelius *et al.*

Our work		Sergelius		Wang		Klotz	
Label	F (T)	Label	F (T)	Label	F (T)	Label	F (T)
		α	0.16				
	1.24(5)	β	0.8				
	2.2(1)	γ	2.5				
	3.5(1)						
	6.3(3)						
	8.0(4)						
	11.5(6)						
		δ	31.7	F0 (W1)	35		
	58.6(5)	2δ	60.4	F1a (W2)	57		
				F1b (W2)	71		
						δ_2'	97
		4δ	119	F2 (W2)	117		
	135.3(5)	ϵ	137.6	F3b (H)	136		
						δ_1''	324

3.3.6 Phase analysis

As mentioned in Section 1.3.4, the phase of quantum oscillations may provide information about the topology of the band structure and might allow us to distinguish Weyl pockets from trivial hole pockets. Given that the phase analysis has proven inconsistent in the SdH and dHvA measurements, it is interesting to explore how well it could apply in ultrasound velocity measurements. It is possible to obtain more information about our sample by further analyzing the Fourier transforms of the above data. Here we use the phase-analysis method of Luk'yanchuk [21] which was used to distinguish different types of Fermi surfaces in graphite. We define the phase-shift function as $K(\phi, \nu) = \text{Re}\{e^{i\phi}\chi(\nu)\}$ where $\chi(\nu)$ is the complex-valued Fourier transform, with frequency ν in units of Tesla and ϕ is the phase. This function can be visualized with a contour plot as a function of ϕ and ν. It presents maxima at the same value of ν seen in the modulus of the Fourier transform $|\chi(\nu)|$. Additionally, the position of the maxima along the ϕ-axis provides

the phase of the corresponding oscillations. K also presents minima at points π out of phase with the maximum. However, in our analysis we have suppressed all negative values of K to simplify the contour plots.

This analysis is shown in Fig. 3.25 for field along [100] and in Fig. 3.26 for field along [001]. We have not performed this analysis for all frequencies in the data since for some there appears to be a large background in the FFT around the peaks and this makes it difficult to extract the phase. The presented peaks appear to be relatively free of background signal. For each orientation of the field, we present the real part, imaginary part and modulus of the Fourier transform in the upper panels, and contour plots of the positive part of $K(\phi, \nu)$ in the lower panels.
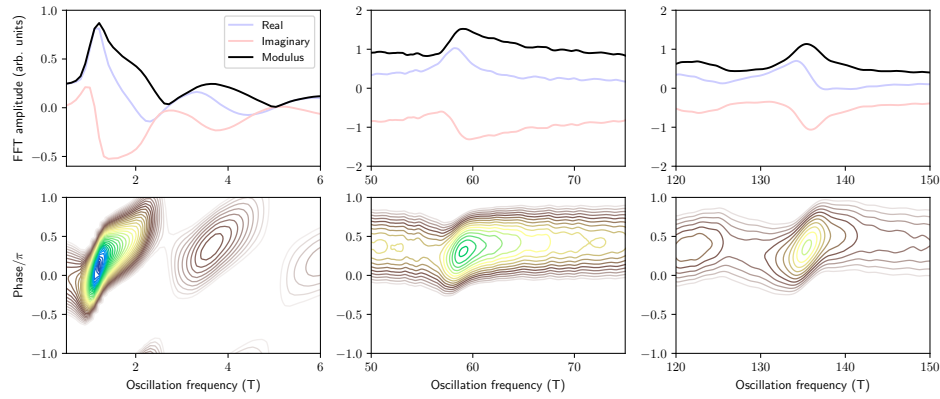

FIGURE 3.25: Phase analysis of several oscillation frequencies for in-plane field along [100]. In the upper panels the real part, imaginary part and modulus of the FFT amplitude is plotted (arbitrarily scaled each time). In lower panels, the corresponding phase is shown in a contour plot with a method described in the text.
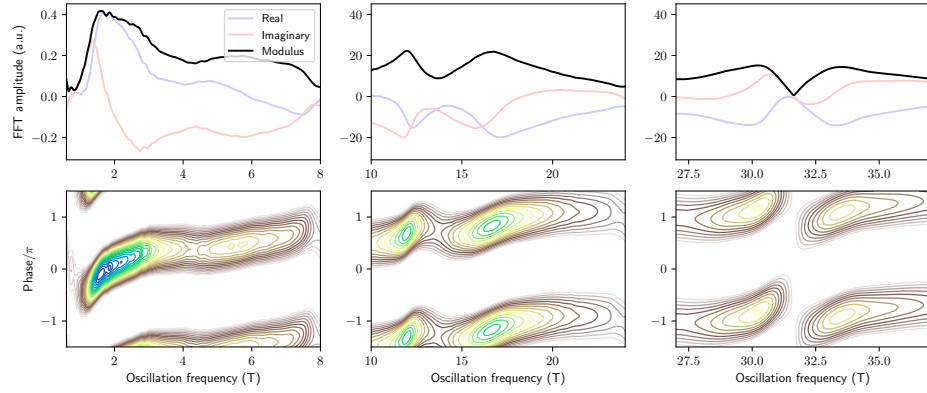
FIGURE 3.26: Phase analysis of several oscillation frequencies for magnetic field along [001]. In the upper panels the real part, imaginary part and modulus of the FFT amplitude is plotted (arbitrarily scaled each time). In lower panels, the corresponding phase is shown in a contour plot with a method described in the text.

TABLE 3.4: Summary of phase analysis results. Here we present just the frequencies for which it was possible to reliably determine the phase and the tentative labels that were assigned in the previous section.

	$\vec{B}//\hat{c}$			$\vec{B}//\hat{a}$	
Label	F (T)	Phase/π	Label	F (T)	Phase/π
β_2?	1.6(3)	-0.08(5)	?	1.24(5)	0.1(3)
α_2	5.8(9)	0.49(5)	?	3.5(1)	0.37(5)
β_1?	12.0(3)	0.69(5)	?	58.6(5)	0.31(4)
?	16.6(7)	0.84(5)	?	135.3(5)	0.37(4)
α_1	30.3(2)	1.15(10)			
γ_1	33.5(4)	1.09(10)			

The results are summarized in Table 3.4. Clear differences in phase are observed for the various oscillations. This is particularly true for $\vec{B}//\hat{c}$. However, our naïve expectations regarding the phase are not met. That is, we would normally expect the oscillations to fall into two categories: topological (Weyl) pockets and topologically trivial pockets. These two categories would be separated by a difference of π in phase, resulting from a trivial Berry phase of 0, or a topological Berry phase of π. There could also be smaller variations of the order of $\pi/4$ resulting from the concavity or convexity of the Fermi surfaces, for example. This is clearly not what is observed here. For $\vec{B}//\hat{c}$ we see a mostly progressive increase in phase

from -0.08(5)π at low frequency to 1.09(10)π at high frequency. In the case of $\vec{B}//\hat{a}$, there are perhaps two categories of oscillations, with the lowest frequency oscillation giving a phase near to 0 and the others giving phases of 0.31π to 0.37π. However, this is clearly not a difference of π.

Hence, it seems that the phase analysis here is either not particularly reliable, or else it is too simplistic to expect the phase to fall into two categories with a phase difference of roughly π and that the theory of quantum oscillations in Weyl semimetals is in fact more complicated.

Chapter 4

Transport Measurements

The transport measurements presented in the following chapter are intended to be used primarily as a sample characterization tool. Plenty of researchers have already done a complete analysis of NbP using transport measurements, making it redundant to redo all of these measurements. The main purpose of these measurements is to see if the same quantum oscillations are visible in both ultrasound and transport measurements using samples that were produced from the same batch. This will help determine the mechanism that allows us to observe quantum oscillations in ultrasound measurements. It was seen in Chapter 3 that the frequencies observed in ultrasounds are not the same as the ones seen for transport measurements done by other research groups. It is important to verify these comparisons with samples procured from the same batch since samples from different batches could have a slightly different Fermi energy and therefore have a smaller or larger Fermi surfaces with different oscillation frequencies. Furthermore, it is interesting to show that transport measurements can be quite sensitive to extrinsic effects like current jetting and compare this with controlled and reproducible ultrasound measurements.

4.1 Experimental Method
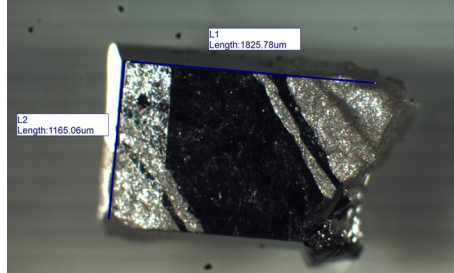
4.1.1 Sample Preparation

FIGURE 4.1: Sample used for transport measurements

The NbP samples used for transport measurements had a smaller thickness and flatter surfaces than the one that was used for sound velocity measurements (Figure 4.1). Samples were first cleaned using acetone and water. Next the contacts were applied using silver paint so as to impose a current along the [110] direction (Figure 4.2). Silver wires were then glued onto the contacts using more silver paint. Wires with a diameter of 50 μm were used for the I_+ and I_- contacts, and silver wires with a diameter of 25 μm were used for the voltage contacts (seen in Figure 4.2). The samples were placed on sample boards using vacuum grease. The samples were placed on different boards depending on the types of measurements taken (in-plane or out-of-plane) and the wires were soldered onto their respective pins on the sample board. Each connection is then verified to check for short circuits. When taking out-of-plane measurements, we found that one contact had a poor connection. In order to fix this problem we sent a current shock through the wire which strengthened the connection.
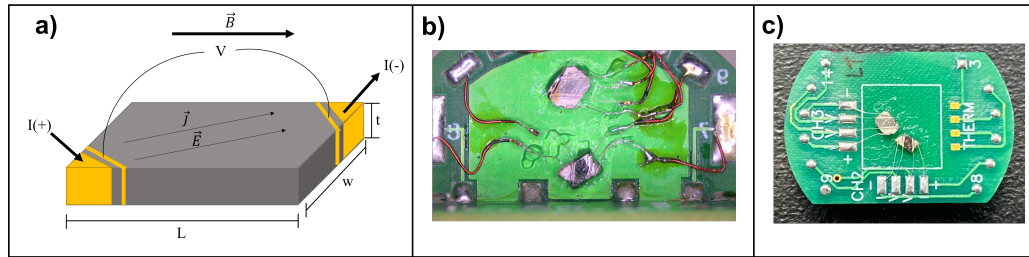
FIGURE 4.2: **a)**Schematic of the sample contacts on the NbP samples prepared for transport measurements. **b)**NbP samples on the sample board for in-plane measurements. **c)**NbP samples on the sample board for out-of-plane measurements.

4.1.2 Physical Property Measurement System (PPMS)

All transport measurements were done on a QuantumDesign Dynacool Physical Property Measurement System (PPMS) located in the Quantum Fab Lab (QFL) of the Institut Quantique. The PPMS is an automated low-temperature and magnet system that allows for the measurement of various material properties. Properties that it can in principle measure include specific heat, magnetic AC and DC susceptibility and electrical and thermal transport properties. This device is paired with a superconducting magnet with a field reaching 14 T and can cover temperatures ranging from 1.9 K to 400 K. DC transport measurements were taken using the DC Resistivity Option for the PPMS, using a resistivity puck (Figure 4.3).

Measurements were taken at a variety of different angles in order to observe the angular dependence of the electrical resistance. In order to take these measurements, a horizontal rotator was used. This horizontal rotator allows a sample to be rotated over 360° while in the presence of an applied magnetic field. The device has an automated indexing procedure and encoder that ensures that the angular positions are accurate [48]. Various sample boards allow for measurements with the field either parallel or perpendicular to the plane of the sample. When transport measurements are taken with the magnetic field B in-plane, the sample board used is the one seen in Figure 4.3b). When transport measurements are taken with the magnetic field out-of-plane, the sample board used is the one seen in Figure 4.3c).
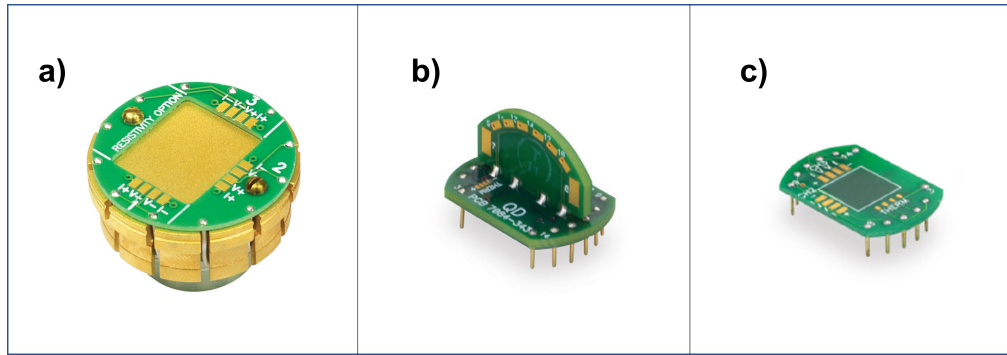
FIGURE 4.3: **a)** Resistivity puck used for AC and DC resistance measurements. **b)** Sample board used for measurements with the magnetic field in plane. **c)** Sample board used for transport measurements with the magnetic field out-of-plane.

4.1.3   Current Jetting and Non-Ideal Contact Geometry

Various inconsistencies can be seen in the results obtained in this chapter, most of which can be explained by the current jetting effect. The current jetting effect occurs when current contacts are smaller than the cross-section of the sample being analyzed. It is characterized by a highly non-uniform current distribution within the sample and can lead to a negative magnetoresistance which makes observing effects like the chiral anomaly very difficult. The current jetting effect is a well documented problem that can be seen in materials like NbP [49].

The current jetting effect tends to hide any signs of the chiral anomaly. It might be possible to separate both effects, however it would require detailed knowledge and modelling of the current jetting. Since the main purpose of the transport measurements in this research is to compare the results with those obtained in ultrasound, current jetting should not have a large effect on our results. We expect that the current jetting will not change the overall frequencies or the temperature dependence of the quantum oscillations for sufficiently small variations in background.

The sample contacts were painted onto the sample by hand leading to some imperfect contact geometries. Due to these imperfect contacts, it is possible that the results could be slightly affected. For example, it is possible that this could lead

to the mixing of the Hall effect into our resistance measurements. In some cases it appears even to lead to a negative resistance, which is clearly artificial.
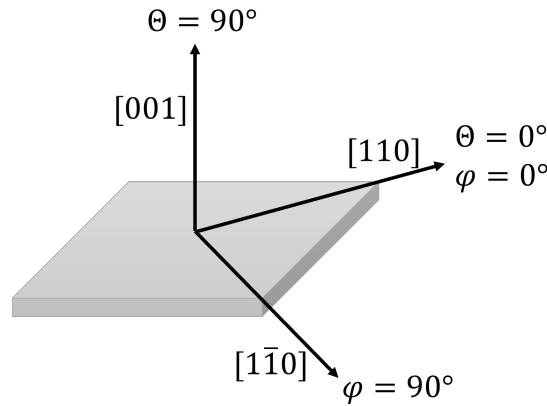
4.2   Results (Field In-Plane)

FIGURE 4.4: Definition of the various orientations of the sample. θ represents the angle definitions in-plane and φ represents the angle definitions out-of-plane.

As mentioned in Chapter 1, niobium phosphide has many Fermi surfaces. Each of these Fermi surfaces will have a contribution to the results that will be seen in transport measurements. In order to see these different contributions, it is necessary to take measurements at a variety of angles. As was done with the ultrasound experiments, we have done series of measurements either rotating in the *ab*-plane (varying the angle φ), or between the plane and the *c*-axis (varying the angle θ). The first measurements that were taken were with the magnetic field staying in the plane of our niobium phosphide samples. The sample starts with the field parallel to the current in the [110] direction (corresponding to $\varphi = 0°$) and is then rotated in order to have the field perpendicular to the current in the [1$\bar{1}$0] direction (corresponding to $\varphi = 90°$) (Figure 4.4). Figure 4.5 shows the cross sections of the different Fermi surfaces that can be observed for in-plane measurements. The Fermi surface schematic used for our analysis is that of Wang *et al.* [29]. This is because the oscillation frequencies found in our transport data correspond almost perfectly with those found by Wang *et al.*.
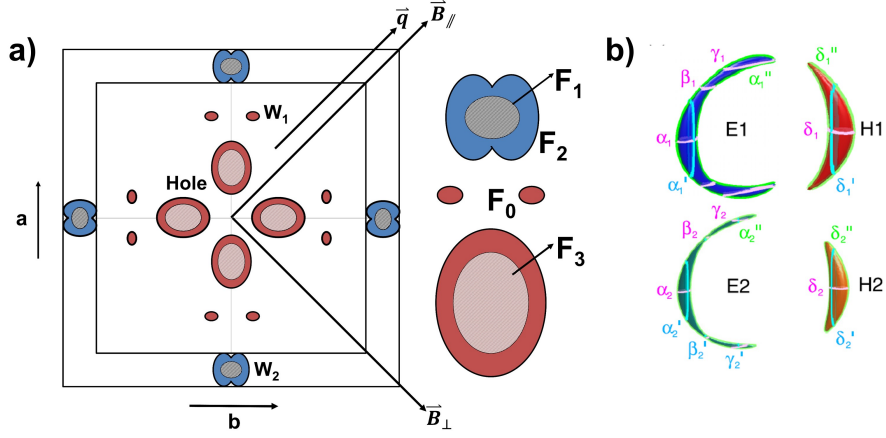
FIGURE 4.5: **a)**Schematic of the Fermi surface cross-sections for the different pockets of NbP[29]. **b)** Schematic of the Fermi surfaces of NbP as depicted by Klotz *et al.* [28]

The raw data obtained from transport measurements is composed of two different contributions: the resistivity and the Hall effect. Figure 4.6 shows a simple schematic of these two components, in an ideal configuration. The oscillation frequencies of niobium phosphide are found by taking the Fourier transform of the resistivity. It is therefore necessary to separate the resistivity from the Hall effect. It is important to note that when the contacts are not perfectly aligned parallel and perpendicular to the current, there will be a cross-contamination of the two signals. We can therefore expect some cross-contamination in our measurements since the contacts are not perfectly aligned. The Hall effect is not a component that we were aiming to measure, but it feeds into the longitudinal resistivity measurement because of the imperfect sample and contact geometries. This is done by symmetrizing and anti-symmetrizing the results using the following equations:

$$\rho = \frac{f(-B) + f(+B)}{2} \tag{4.1}$$

$$H = \frac{f(-B) - f(+B)}{2} \tag{4.2}$$

where ρ is the resistivity, H is the Hall effect, $f(-B)$ is the data from -14T to 0T, and $f(+B)$ is the data from 0T to 14T. By using equations 4.1 and 4.2, we obtain the results seen in Figure 4.7.
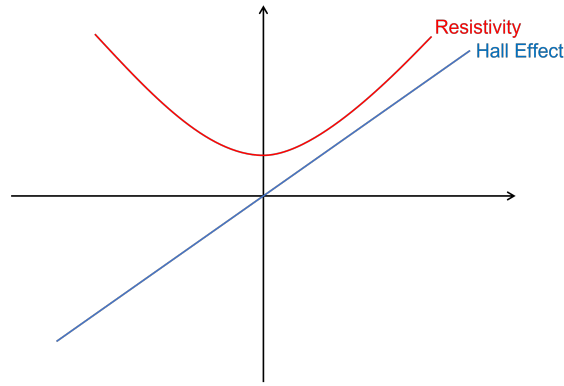
FIGURE 4.6: Simple schematic of the Hall effect component and the resistivity component in transport measurements.
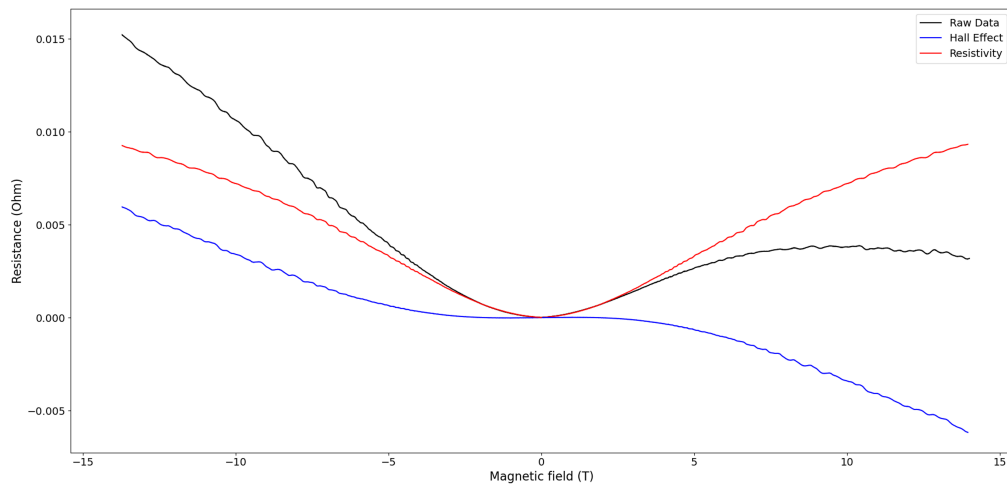

FIGURE 4.7: Hall effect and resistivity components of the raw transport data with the field oriented at $\varphi = 45°$ from the current.

Next we must subtract the background magnetoresistance from the data. This is done by fitting a fifth order polynomial curve to the resistivity curve (this gives the best fit to the data). This gives us an equation for the background noise. The polynomial is then subtracted from the resistivity, giving clean data that can then be used to calculate the Fourier transform. In Figure 4.8 we can see this background subtraction take place. It is important to note that every set of raw data was taken with the field sweeping up (-14 T to 14 T) and down (14 T to -14 T). These two sets of data are then averaged to obtain the final results. By averaging the curves we are avoiding any hysteresis in the applied magnetic field

that could cause problems with the periodicity of the oscillations as a function of 1/B.
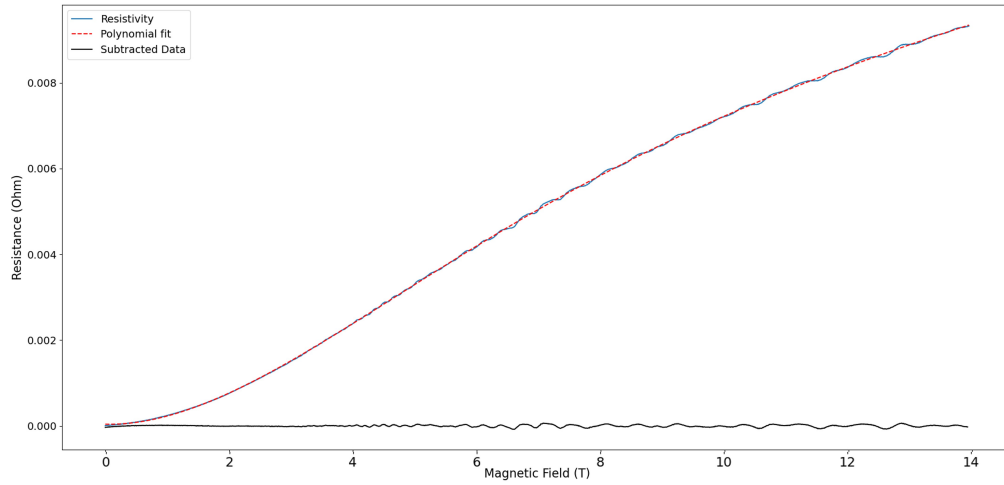

FIGURE 4.8: Background subtraction of the resistivity with the field at 45° to the current

Finally the Fourier transform is taken. Both the modulus and the apodized modulus were taken. The apodized data is used to reduce the residual background at low field that gives rise to a big peak at F=0. In order to apodize the data, the data is multiplied by a Gaussian function of $1/B$ which gradually suppresses the data at high inverse field, which reduces noise in the Fourier transform. However, since the data points at high inverse field are still there, they will still contribute to the Fourier transform and the density of points in the Fourier transform will remain high. When analyzing the data, if one uses a sharp cut-off in $1/B$ to filter the data, the resulting Fourier transform peaks will be modulated with a sinc function. This leads to additional peaks and data that is very difficult to interpret.
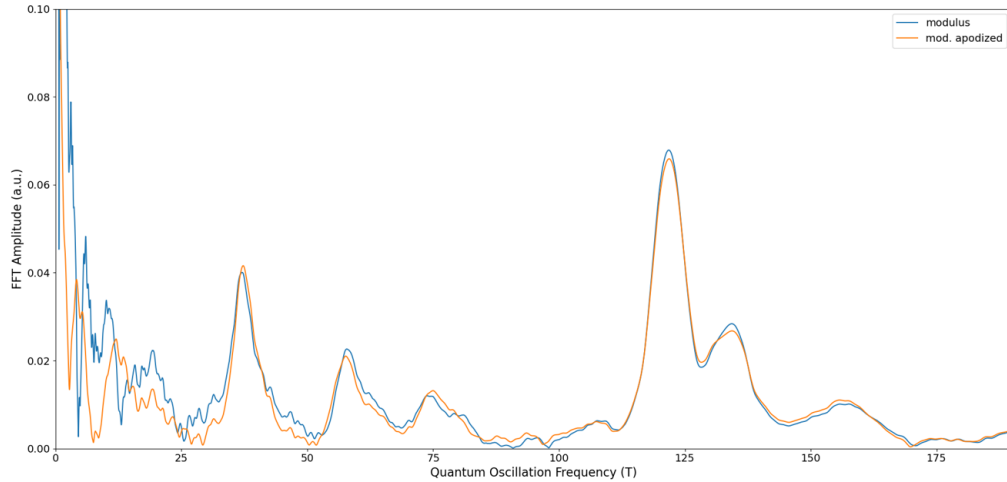
FIGURE 4.9: The Fourier transform of the transport measurements with the field at 45° to the current.

4.2.1   Angle Sweeps

In order to determine the orientation of the sample, measurements were taken at a fixed field and temperature with the sample rotating from -10° to 360° (the PPMS rotator covers a much larger range of angles than the ultrasound rotator probe). From the results observed in Figure 4.10, we can see that there does not seem to be a point of high symmetry that clearly indicates the position of $\varphi = 0$, unlike what will be presented in Section 4.3. This lack of C4 and C2 symmetry could be due to a number of factors. The current distribution will depend intricately on the sample and contact geometry relative to the field direction. Therefore, our imperfect contacts could explain this lack of symmetry. It is also possible that this is caused by the current jetting effect or the chiral anomaly. In order to determine the value of φ=0, a picture of the sample was taken and lines were drawn along the edge of the sample and the edge of the sample board. This allowed us to estimate the orientation of the sample. This method is not as precise as the method used for ultrasound measurements and can therefore lead to a less precise measurement of the sample orientation. The value of φ=0 was found to be located at approximately 78°. It is possible that the missing symmetry point is caused by the sample geometry or by current jetting. This shows that the angular

dependence is more complicated than looking at the angle between the magnetic field and crystallographic axes, being there is also the orientation of the current and voltage contacts and the possible inhomogeneities of the conductivity within the sample. This is an indication that the transport measurements are less reliable than the ultrasound measurements.
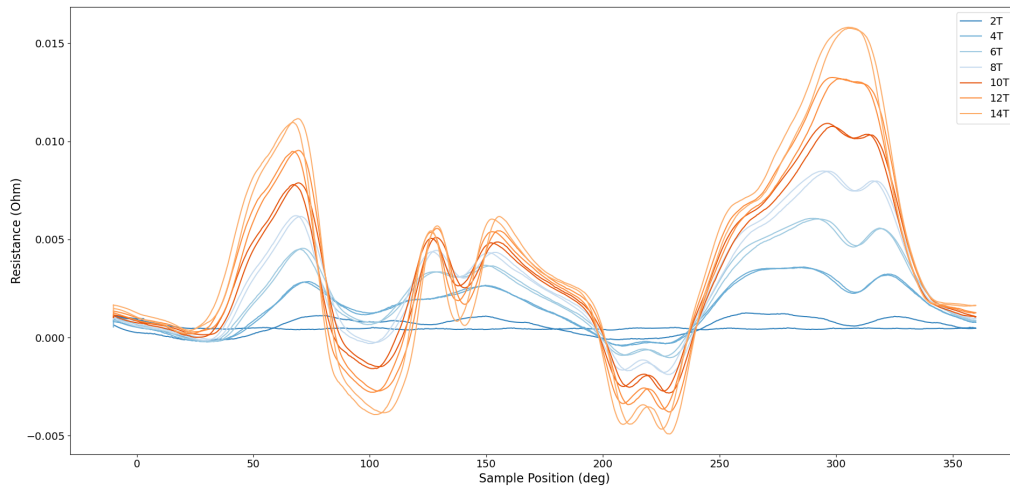

FIGURE 4.10: The variation of the resistance as a function of the sample position measured by the rotator for measurements with the magnetic field in-plane

4.2.2 Field Sweeps

Field sweep measurements were taken at various angles to observe how the quantum oscillations change at different orientations of the sample. We can see that at -45° and -40° the resistivity is negative. However for all other orientations, the resistivity stays positive. It is also possible to observe that the Hall effect switches signs at our symmetry point(0°) and at 90°. These results are not what we would expect from these kind of measurements. When current jetting is present in transport measurements, it is possible to see a distorted electric potential profile within the sample that can give strange counter intuitive results. The data also seems to show that there is a large amount of Hall effect going into the longitudinal resistance measurements. Once again, this is a result of the current jetting effect. For the purpose of this research, we are not very concerned with the current jetting that occurs since this is an issue that has already been tackled by other researchers

[41, 42]. These effects should not have an effect on the frequencies of quantum oscillations. They should however make it impossible to correctly determine the phase of oscillations. This is an issue that can easily be avoided when taking ultrasound measurements where there is no reason to expect current jetting to occur.
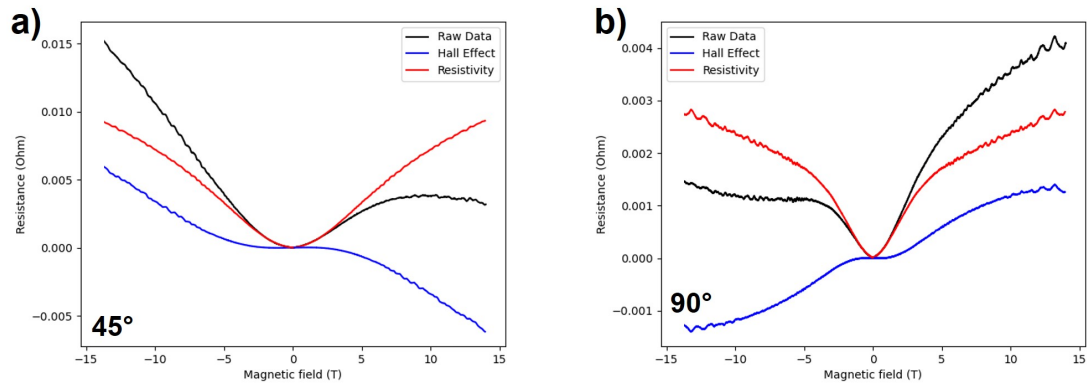

FIGURE 4.11: Resistance as a function of the magnetic field on NbP at various angles. **a)**φ=45° from the current. **b)**Measurements perpendicular to the current (φ=90).

Fourier transforms of the resistivity can be found in Figure 4.12 and present a number of peaks that can be compared with those of Wang et al [29]. They are identified as F_0, F_1, F_2 and F_3 the different Fermi surface cross-sections seen in Figure 4.5.
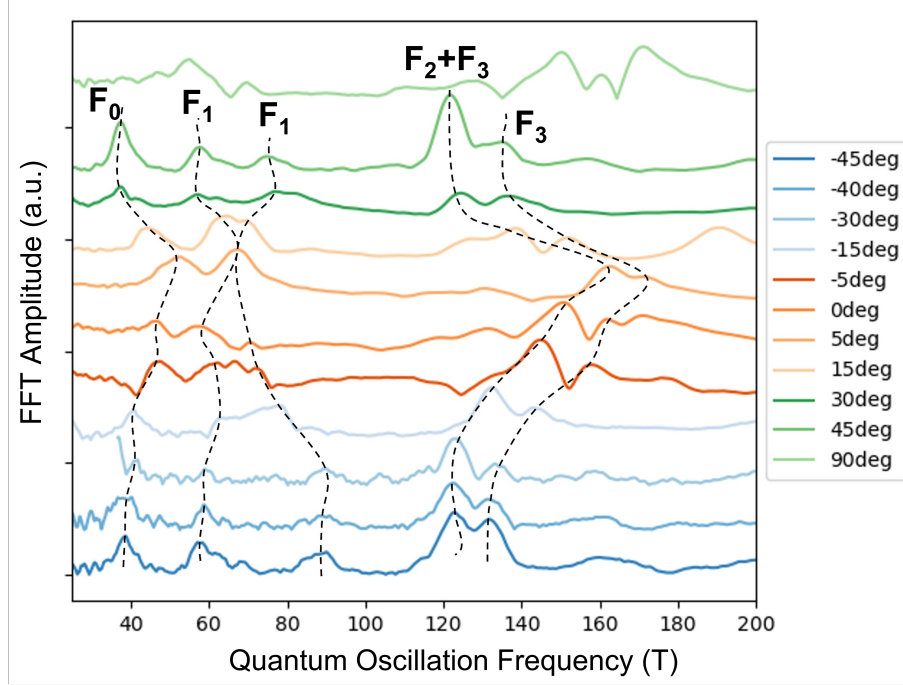
FIGURE 4.12: Transport measurements of the evolution of F_0, F_1, F_2 and F_3 as a function of φ after a polynomial background subtraction and Fourier transform

Figure 4.12 shows the angle dependence of the Shubnikov-de Haas (SdH) oscillations in NbP. The different oscillation peaks represent the different Fermi surface cross-sections that are found in-plane. In order to determine which peaks correspond to which pocket, reference [29] was used as a reference guide. In this paper, transport measurements were done on NbP. Measurements start in-plane and the field is then rotated out-of-plane. When the field is at 90° in this paper, it corresponds to the oscillations we see when our sample is at $\varphi=45°$ from the current. By comparing these two spectra, we can then determine which peaks correspond to which Fermi surface at $\varphi=45°$. From these peaks, we can then follow how the peaks shift as the orientation of the magnetic field is changed. In Wang *et al.* the peaks found at our alignmnemnt of $\varphi = 45°$ are F_0=35 T, F_1=60 T, F_1=70 T, $F_2 + F_3$=118 T and F_3=135 T. These values match our values almost perfectly where we obtain F_0=37 T, F_1=57 T, F_1=74 T, $F_2 + F_3$=121 T and F_3=135 T.

From observing Figure 4.12, we can see that some peaks have larger angle dependence than others. For example, the F_2 peak shifts from $F = 162$ T to $F = 122$ T where as F_0 shifts from $F = 52$ T to $F = 37$ T. We can also see from the data

that the largest value of F$_3$ is found at φ=5° and not at φ=0°. This could just be due to a misalignment of the sample on the sample holder. Something interesting to observe is that certain peaks split as the field is rotated. This is typical for ellipsoid-shaped Fermi surfaces of parabolic energy bands[29]. We can also see that as the field is rotated in-plane, the F$_2$ and the first F$_3$ peaks are merged together to form one large peak. When rotating the field out-of-plane this is not the case. As seen in Figure A.7 in Appendix A, we can see that low oscillation frequencies cannot be observed for in-plane transport measurements due to the large amount of noise visible at low frequencies. This is the opposite of what we see in ultrasound measurements where it is primarily the low oscillation frequencies that are visible.

4.2.3 Temperature Dependence

As expected, the quantum oscillations that we see in our measurements decrease as we increase the temperature of the sample. All temperature measurements were done with the sample positioned at φ=0. As previously mentioned, the oscillations decrease in amplitude as the temperature is increased. Once at 20 K, the oscillations completely disappear. These measurements can be used to perform mass calculations on our data.
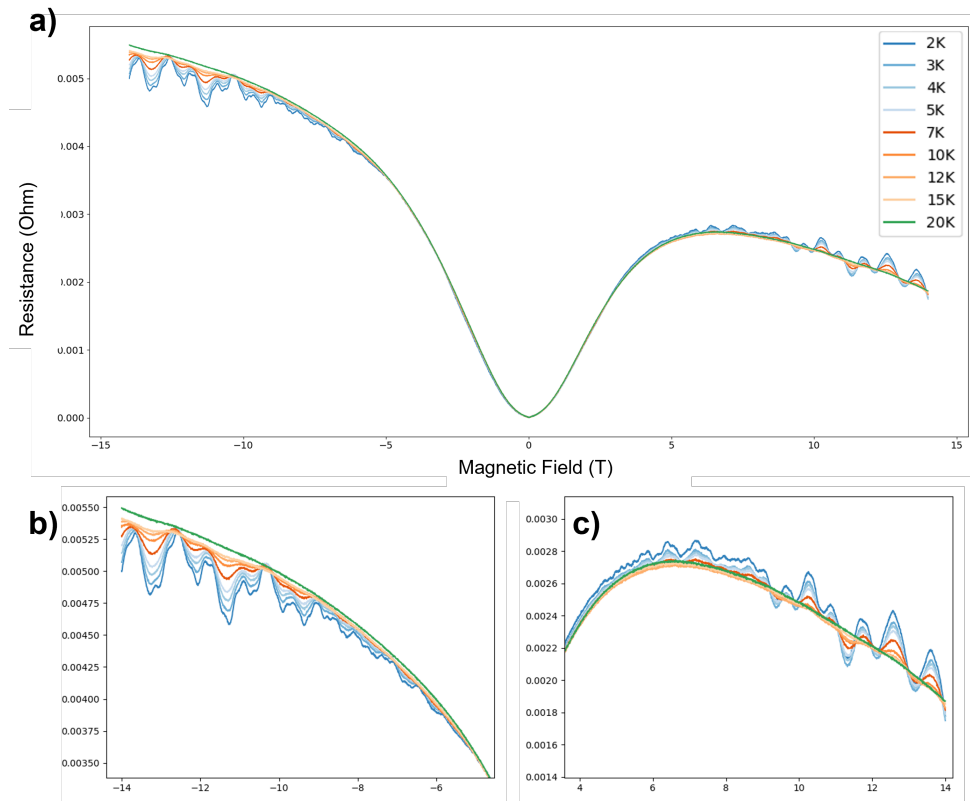
FIGURE 4.13: **a)**Field sweeps from -14T to 14T at various temperatures. The oscillations decrease in amplitude as the temperature increases. **b)**A zoom of the oscillations at negative fields to properly show the change in amplitude of the oscillations. **c)**A zoom of the oscillations at positive fields

Next the Fourier transform of these oscillations were taken in order to see the evolution of the oscillations frequencies as the temperature is increased.
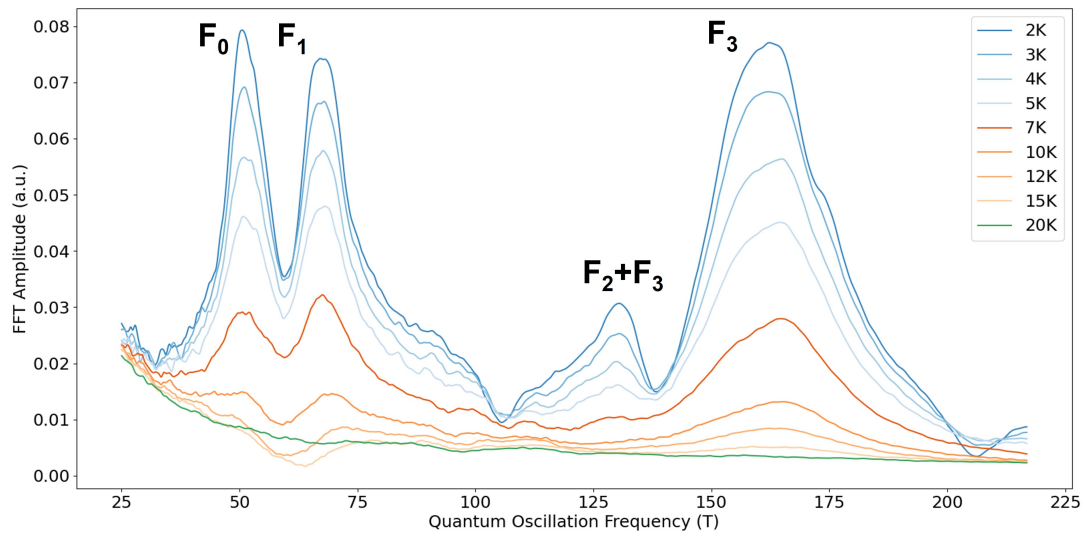
FIGURE 4.14: The temperature dependent SdH oscillations when the magnetic field is parallel to the current.

Figure 4.14 shows the decay of the different oscillation peaks as the temperature is increased. We can see that at a temperature of 10K the oscillation peaks F_0 and F_2+F_3 are almost completely indiscernible whereas the oscillation peaks F_1 and F_3 are still present. This could be related to the fact that F_0 and F_2 are Weyl semimetal pockets, whereas F_1 and F_3 are trivial pockets.

Using the method explained in Section 1.3.3 it is possible to calculate the effective mass of the carriers in the measured Fermi surfaces. These measurements are done on the resistivity measurements without a Fourier transform. This is because each peak in the Fourier transform does not have a well defined magnetic field value (since it is taken from an analysis of a broad range of magnetic fields), making the peak useless in equation 1.17. It is more straightforward to follow the oscillation amplitude at a particular field value for $\rho(B)$.
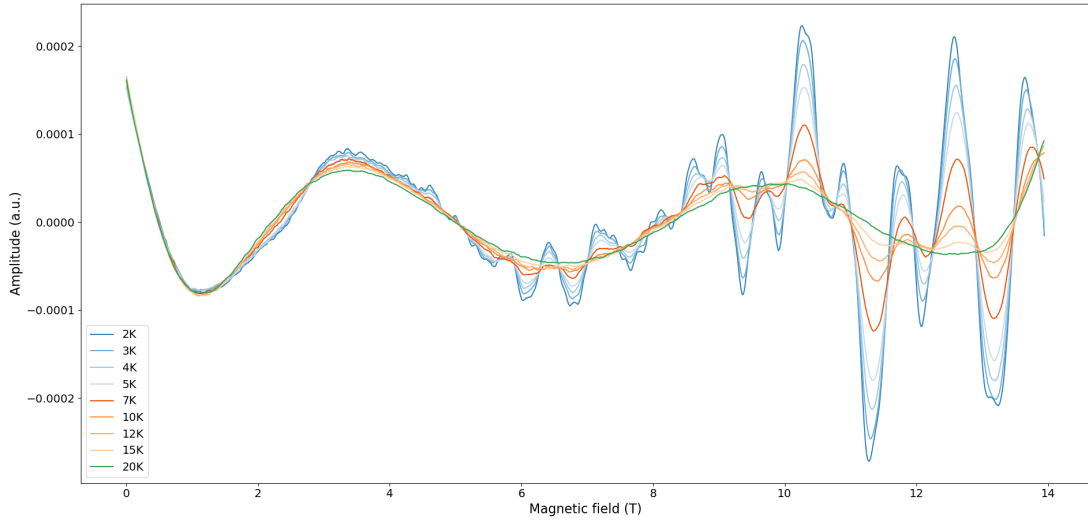
FIGURE 4.15: Temperature dependence of the quantum oscillations after a background subtraction.

In order to determine the effective mass, the height of the oscillation located at 12.5 T was noted at each temperature. The $H = 12.5$ T peak was chosen because it has a flatter background and has the clearest oscillation. The height of the peak as a function of the temperature was then plotted out and was fitted with equation 1.17. Because the background subtraction was not perfect, an offset was added to the thermal factor to properly fit the curve. By fitting the thermal damping factor, the effective mass was found to be $m^* = 0.309m_e$. Effective mass calculations on NbP were done by Wang *et al.* [29], however the measurements were done with $H = 13.4$ T and at a different field orientation. The values found by Wang *et al.* ranged from $m^*=0.1m_e$ to $m^*=0.47m_e$. Therefore the value found for the effective mass from our data seems to be consistent with what is found in the literature. We were unable to find other papers that calculated the effective mass of NbP at the same orientation as our research.
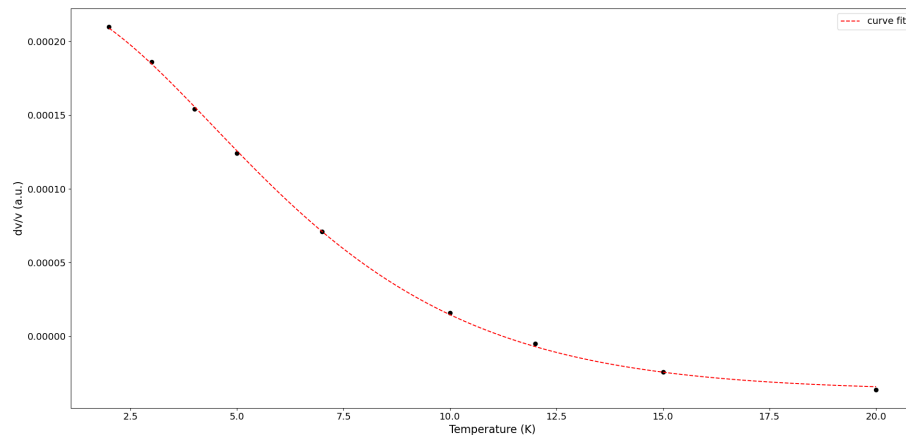
FIGURE 4.16: Temperature dependence of the height of the quantum oscillation located at H=12.5 T. The red dotted line represents the fit of equation 1.17 where $m^* = 0.309m_e$.

4.3   Results (Field Out-of-Plane)

Transport measurements were taken with the magnetic field rotating out of the plane of the sample. The same samples were used for the out-of-plane measurements as the in-plane measurements with the current along the [110] direction. The magnetic field was rotated from [110] to [001] where [110] corresponds to $\Theta = 0°$ and [001] corresponds to $\Theta = 90°$ for the results seen in this section (Figure 4.4). The samples were placed on a sample board like the one seen in Figure 4.3c) using vacuum grease. The data analysis in the section is the same as the analysis technique explained in Section 4.2.

4.3.1   Angle Sweeps

As done for the in-plane measurements, an angle sweep of the sample was done at various fields to try and find the symmetry point of the sample. With the sample rotating from -10° to 175° and the field varying from 2T to 16T, a symmetry point was found at around 95° (Figure 4.17). The absolute value of 0° is therefore located at 95°. This differs from our results found in Section 4.2.1, where there was no evident point of high symmetry.
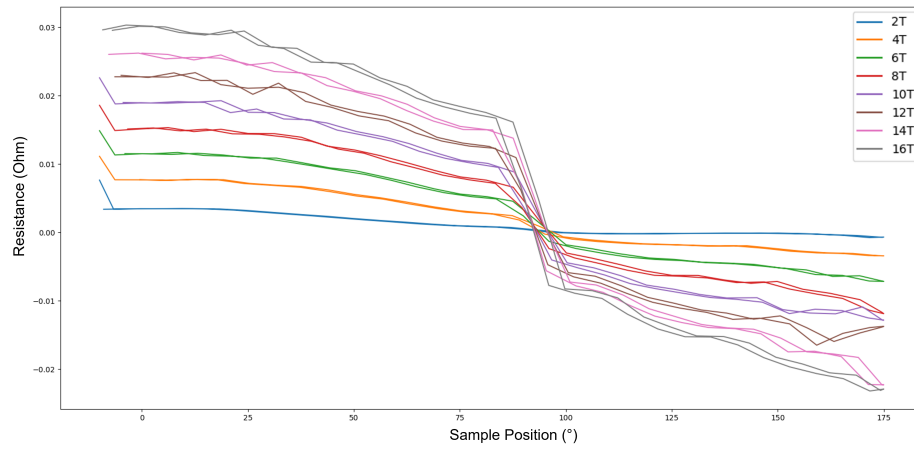
FIGURE 4.17: The variation of the resistance as a function of the orientation of the sample for measurements with the field rotating out-of-plane. The sample position corresponds to the angle as defined by the rotating PPMS probe.
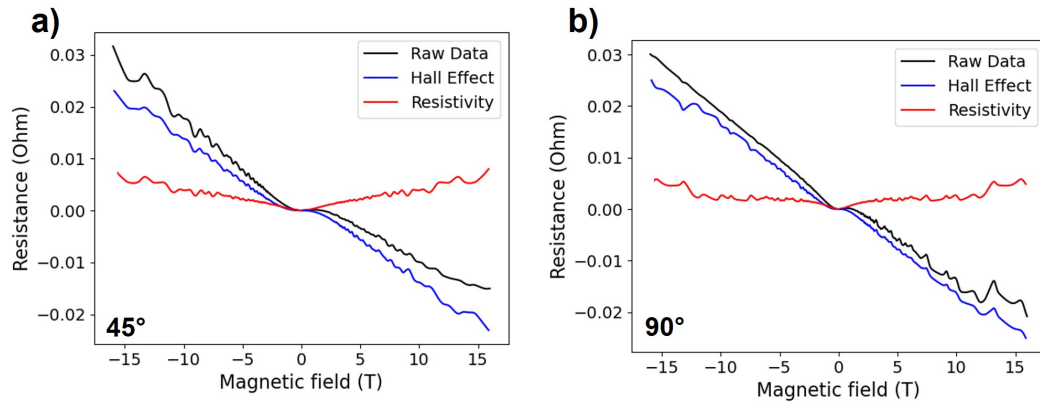
4.3.2 Field Sweeps

FIGURE 4.18: Resistance as a function of the magnetic field on NbP at various angles. **a)**Out-of-plane measurements done at $\Theta=45°$ from the current and **b)**$\Theta=90°$ from the current.

Unlike what was seen for the in-plane measurements, the resistivity does not switch signs for out-of-plane measurements. This could be linked to the current jetting effect. Similarly to Section 4.2.2, we want to take the Fourier transform of the curves seen in Figures A.5 and A.6 in order to obtain information about the Fermi surface of NbP. These Fourier transforms can be seen in Figure 4.19.
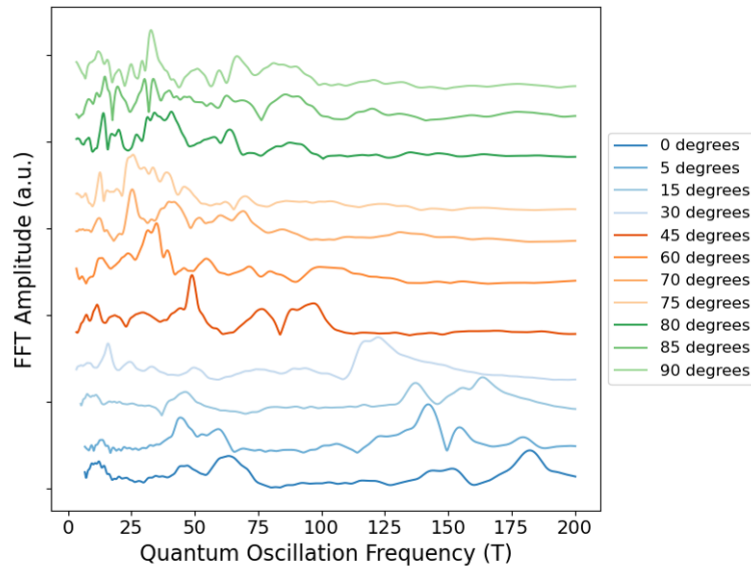
FIGURE 4.19: Transport measurements of the evolution of the Fermi surfaces of NbP as a function of Θ after a polynomial background subtraction and Fourier transform.

These curves are much more complex than those seen for the in-plane measurements. The many oscillations seen are a combination of the Fermi surface oscillation frequencies and of the harmonics of these peaks. Taking a closer look at the measurements taken with the field perpendicular to the current (i.e. $\theta = 90°$) allows us to compare with the literature and identify these different peaks.
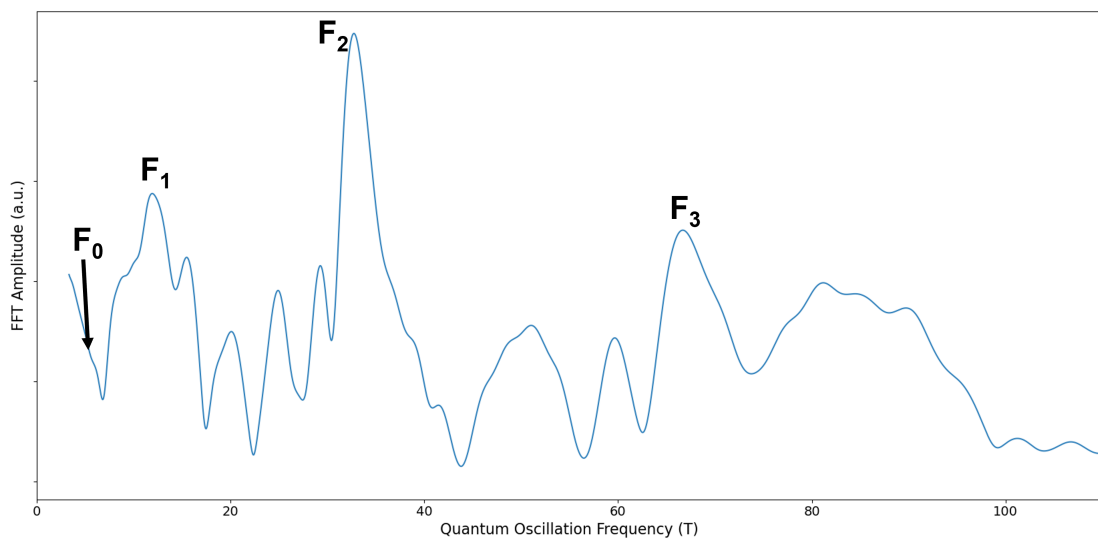

FIGURE 4.20: Fermi surfaces F_0, F_1, F_2 and F_3 when the magnetic field is perpendicular to the current.

As in the previous section for in-plane measurements, the peaks F_0, F_1, F_2 and F_3 were identified using the reference [29]. The oscillation frequencies determined in reference [29] are quite close to the peaks shown in our data in Figure 4.20. More precisely, peaks were found at $F_0 = 5.8$ T, $F_1 = 12.0$ T, $F_2 = 32.5$ T and $F_3 = 66.4$ T. The various other peaks that can be found in Figure 4.20 are likely higher harmonics of the frequencies F_0, F_1, F_2 and F_3. These can be identified as harmonics because they are evenly spaced, multiples of the fundamental frequencies and have smaller intensities than the fundamental peaks.
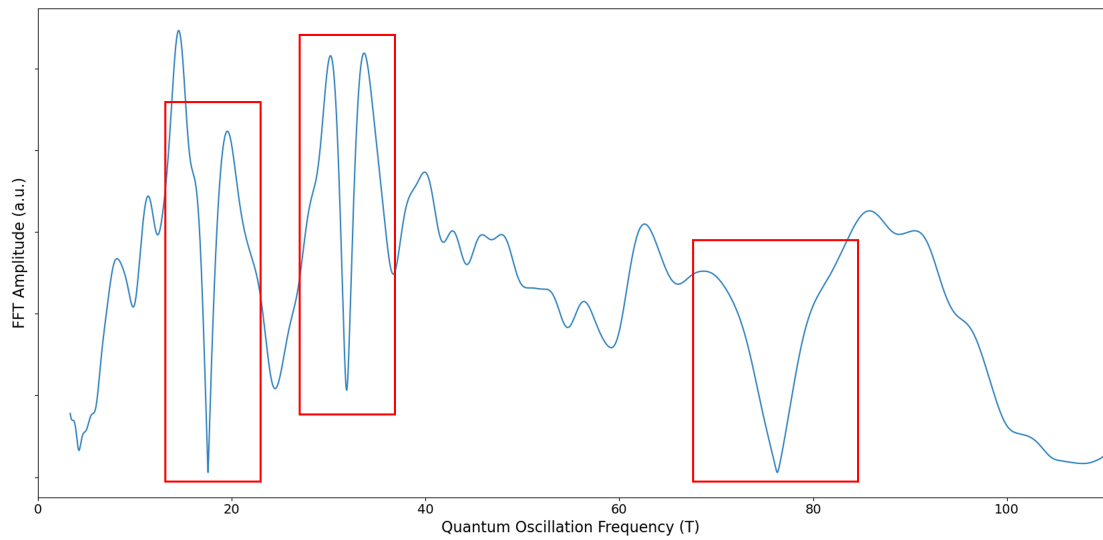

FIGURE 4.21: FFT amplitude as a function of the quantum oscillation frequency when the magnetic field is at 85° from the current. The red rectangles represent the different areas where there are two frequencies nearly out of phase.

There are additional features that can be seen in the curves that cannot be attributed to higher harmonics. These features can be seen in Figure 4.21. When the field is at 85° from the current, sharp dips in the frequencies can be observed. These dips occur at approximately 17 T, 32 T and at 76 T. These dips can be created by two frequencies that are nearly out of phase.
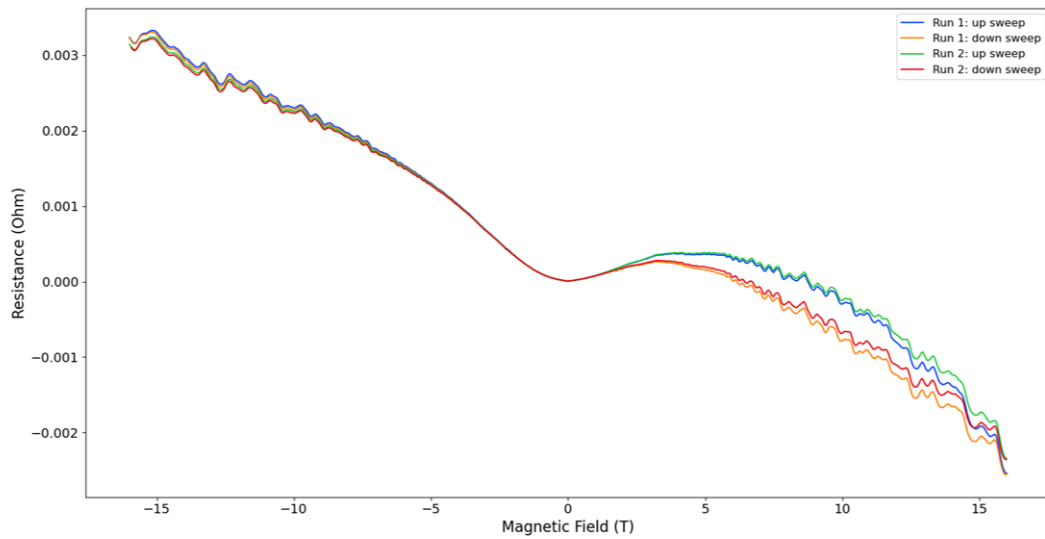
FIGURE 4.22: Asymmetry seen in the up and down sweeps of the magnetic field when the field is parallel to the current.

It is important to note that an abnormality was seen in the data collected when the magnetic field was at an angle of 0°. Hysteresis is visible, that is a difference between the data that was taken with the magnetic field sweeping up and the data with the magnetic field sweeping down. This gap is only seen at positive magnetic fields and can only be seen at Θ=0°. In order to confirm that these results were true, a second set of measurements were taken with the same parameters. These results can be seen in Figure 4.22 and the same gap can be seen in the second set of measurements. Despite the hysteresis to the background magnetoresistance, up and down sweeps both have the same oscillation frequencies. These results might be a mechanical hysteresis resulting from an unstable or multi-stable rotator at specific angles that shifts under an applied field.

4.3.3 Temperature Sweeps

As it was seen for the in-plane measurements, the quantum oscillations decrease in amplitude as the temperature is increased. All temperature measurements were done with the magnetic field perpendicular to the current. The magnetic field was swept from -16 T to 16 T.
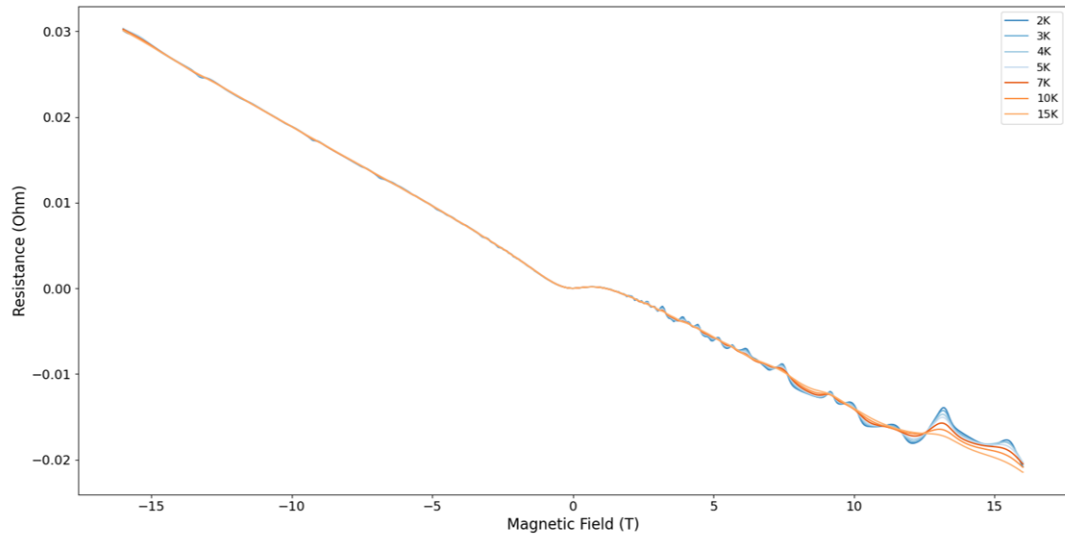
FIGURE 4.23: Field sweeps from -16 T to 16 T at various temperatures. The oscillations decrease in amplitude as the temperature increases.

The Fourier transform of the quantum oscillations was taken for each temperature measurement in order to properly observe the revolution of the oscillation frequencies.
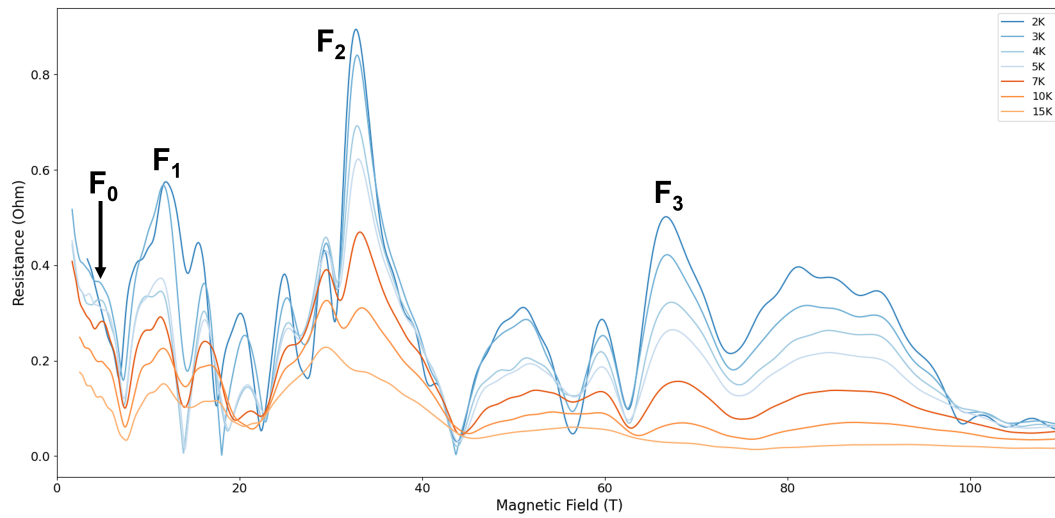

FIGURE 4.24: Temperature dependent SdH oscillations when the magnetic field is perpendicular to the current

From Figure 4.24, the decay of the different oscillation peaks can be observed as the temperature is increased. We can see that the F_3 peak is almost completely

gone when a temperature of 15 K is reached, whereas peaks F_0 and F_2 are still very discernible. We would expect F_1 to behave similarly to F_3 because they are both trivial pockets. It is possible that this difference is caused the the visible harmonics. These harmonics could be mixing with the F_1 peak, making it appear larger than it truly is.

Effective mass calculations were performed using the same method described in Section 4.2.3. The oscillation peaks located at 7.5 T and 13.4 T were chosen for effective mass measurements. These peaks had the clearest oscillations allowing us to properly calculate the effective mass.
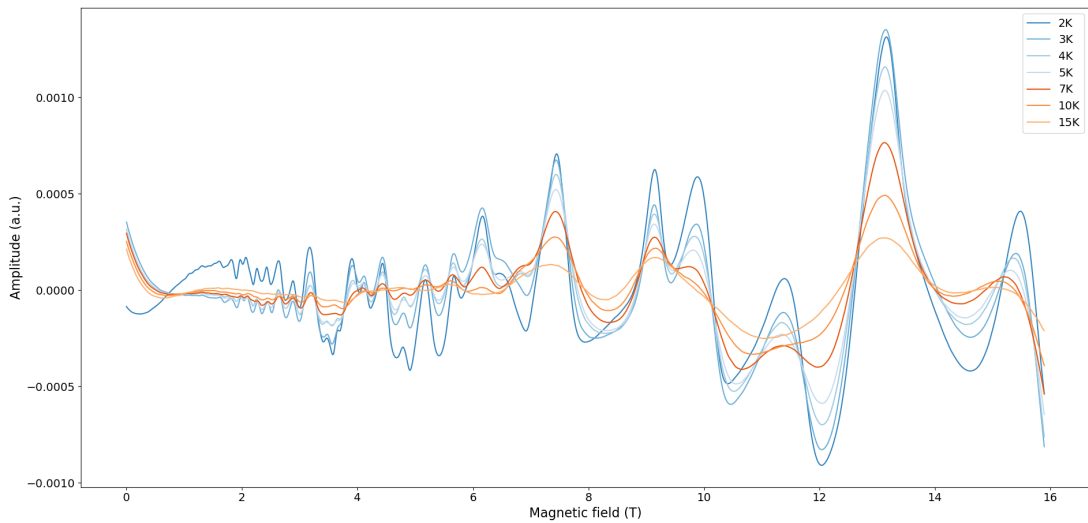

FIGURE 4.25: Temperature dependence of the quantum oscillations after a background subtraction for out-of-plane measurements.

The height dependence of the peaks as a function of the temperature was plotted and the thermal damping factor was fit to the data to obtain the effective mass with an offset to account for the background. The effective mass at H=7.5 T was found to be $m^* = 0.160m_e$ and the effective mass at H=13.4T was found to be $m^* = 0.292m_e$. Klotz *et al.* performed effective mass calculation on NbP as well at similar magnetic fields [28]. They found $m^* = 0.05m_e$ for H=9 T and $m^* = 0.120m_e$ for H=13 T. The difference between our results could be because we have a different contact geometry than what Klotz *et al.* have. This shows that the exact value of the effective mass changes according to the magnetic field

chosen. This could be because different Fermi surfaces contribute at each field and we are therefore measuring the effective mass of different Weyl nodes. An ideal analysis would likely need to consider the amplitude of a particular peak in the Fourier transform, but would also have to take into account the width of the peak. This is because the damping factors have a field-dependence which leads to to a faster decay of the oscillations as a function of $1/B$ as temperature is increased, leading to a broadening of the Fourier transform peaks.
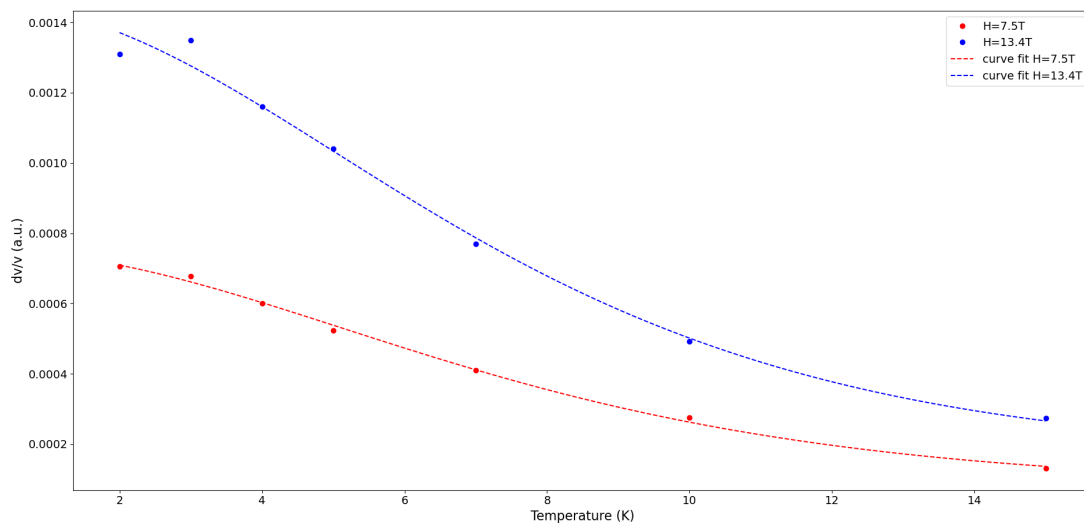

FIGURE 4.26: Temperature dependence of the height of the quantum oscillations located at H=7.5T and H=13.4T with $m^* = 0.160m_e$ and $m^* = 0.292m_e$ respectively.

4.4   Discussion

Despite the likely presence of current jetting and a non-ideal sample and contact geometry, these transport measurements showed clear quantum oscillations and these could be compared with those measured by other groups in the literature. In particular, the oscillation frequencies that we observed were found to be quite consistent with the measurements of Wang *et al.* This shows that our samples are of comparable quality to theirs and have a similar Fermi energy.

Moreover, the transport measurements we carried out on our samples have allowed us to confirm that sound velocity and electrical transport give rather different

results. Most importantly, sound velocity can be seen to be highly sensitive to lower-frequency oscillations that are almost completely invisible in the resistivity results. When comparing the results obtained using each method, we can see that ultrasound measurements detect certain oscillation frequencies that transport measurements cannot. For example, ultrasound measurements detect oscillation frequencies at 1.7 T, 5.4 T, 12 T and 20 T when measuring at $\varphi=0°$ when transport measurements cannot. Sound velocity measurements also detect frequencies at 1.5 T and 5.5 T when $\theta=90°$, which cannot be seen in transport measurements.

The transport measurements also show the risks of current jetting and the difficulty of obtaining a reliable measurement of a longitudinal negative magnetoresistance brought on by the chiral anomaly. For example, one could be tempted to proclaim evidence for a chiral anomaly-induced negative magnetoresistance in the high-field downturn of the curve measured at 5° presented in Figure A.4. However, it can be seen that this effect is absent in the 0° curve in Figure A.3, implying that it is most likely a result of current-jetting. This emphasizes our claim that sound velocity is a more reliable method to look for the chiral anomaly, even if the previous chapter shows that it is either not present or too small to be observed in NbP. It is also likely that the phase of quantum oscillations is particularly difficult to extract reliably from the transport measurements.

Finally, the significant differences between transport and sound velocity show that we likely cannot attribute changes in sound velocity as a function of magnetic field to changes in conductivity of the sample (resulting from screening of the piezoelectric effect caused by sound waves propagating in the sample). The large background (slowly varying) magnetoresistance that is seen in transport measurements is simply not present in the sound velocity measurements, which are instead dominated by the quantum oscillations.

Chapter 5

Conclusion and Outlook

Within this thesis, we have managed to analyse a number of results on the Weyl semimetal NbP obtained using both sound velocity measurements and transport measurements. These results have allowed us to determine the differences between the quantum oscillations of each measurement technique. The ultrasound measurements have allowed for a more precise determination of the quantum oscillation frequencies, especially when observing low oscillation frequencies.

A careful analysis of angular variations of the sound velocity show no significant evidence of the chiral anomaly, in contrast with what was seen in previous research performed on TaAs. This indicates that further work must be done on NbP to try and observe the chiral anomaly or else explain why it is not observable.

This research has helped solidify the importance of using sound velocity measurements as an analysis technique for detecting quantum oscillations. As previously stated, ultrasound measurements were better at detecting lower oscillation frequencies. They are also much more reliable than transport measurements, as they are not affected by effects such as the current jetting effect and a slowly-varying background magnetoresistance that make transport measurements particularly difficult to analyse and interpret.

There is still more work that can be done to continue this project. It would be important to perform more measurements on TaAs to confirm that the previous

observations of the chiral anomaly in the sample are correct. It would also be pertinent to carry out more measurements on NbP at higher magnetic fields to see if it would reveal the chiral anomaly. More research needs to be done to better understand how sound velocity is coupled to different Fermi surfaces in Weyl semimetals. Our initial, naïve expectation that decreases in sound velocity are related to increases in conductivity appears to be false. This assumption would imply that the sound velocity and transport measurements would be equally sensitive to all quantum oscillation frequencies, which is evidently not what we observe. To better understand the results obtained in this thesis, it would be extremely valuable to launch a discussion with theorists to consider how the various Fermi surfaces ought to be coupled to strain in the sample.

It also remains difficult to identify certain oscillations, particularly those at very low frequencies, and in this regard we could also benefit from a collaboration with researchers who have an expertise in *ab initio* electronic structure calculations. Even Subnikov-de Haas oscillations between different groups do not agree very well regarding certain oscillation frequencies in NbP and these discrepencies probably call for further theoretical work on this material's complex Fermi surface and the possible effects of sample disorder.

Finally, the qualitative disagreement between our work and that of Schindler *et al.* [47] needs to be resolved. It would be worth remeasuring their sample with our apparatus, or vice versa to verify that the origin of the difference is not experimental error and indeed comes from the sample.

Meanwhile, the family of Weyl semimetals of various types has grown considerably in recent years and we feel that sound velocity measurements on many of these materials could bring important contributions to this research area. So far only TaAs and NbP have been studied with sound velocity. Two other members of this family, TaP and NbAs, could easily be studied, not to mention rather different Type-II Weyl semimetals like $MoTe_2$ and WTe_2.

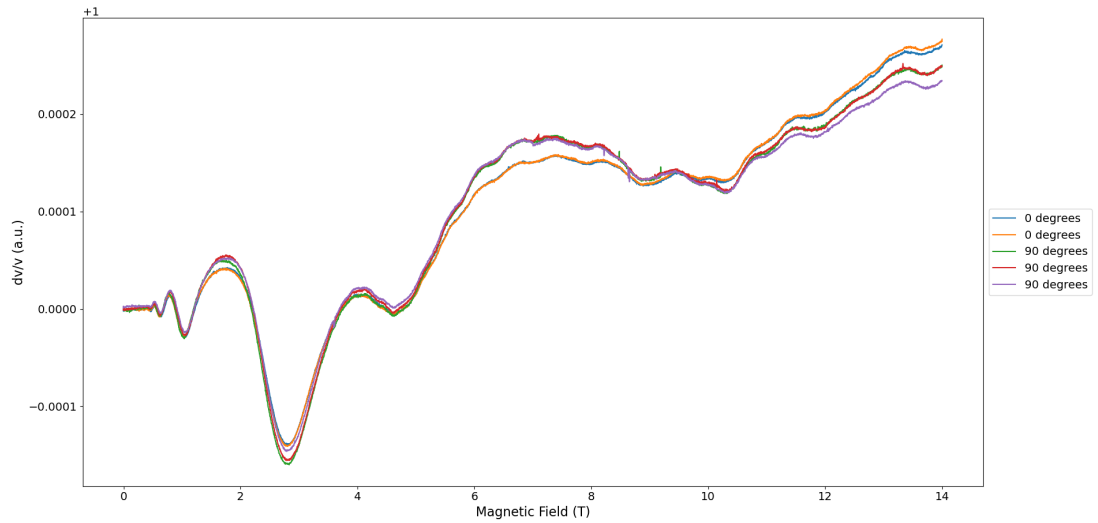# Appendix A

Supplementary Plots

A.1 Sound Velocity

FIGURE A.1: Comparison between the measurements taken at 0° and 90°. The difference between the curves at each angle is largely reproducible, but there are some small discrepancies visible for 90° above roughly 11 T.
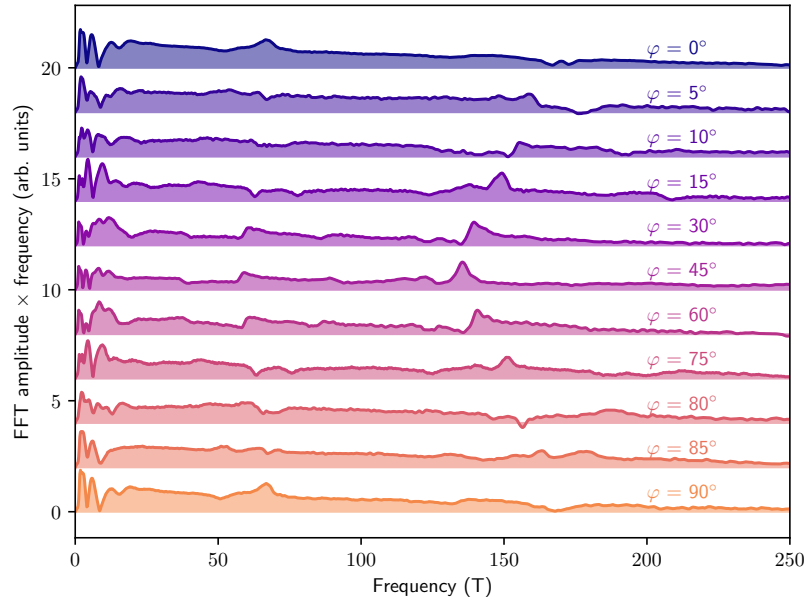
FIGURE A.2: Evolution of the quantum oscillation frequencies at various orientations of NbP for in-plane measurements at higher oscillation frequencies. The FFT amplitude is multiplied by the frequency to better expose small peaks at higher frequencies.

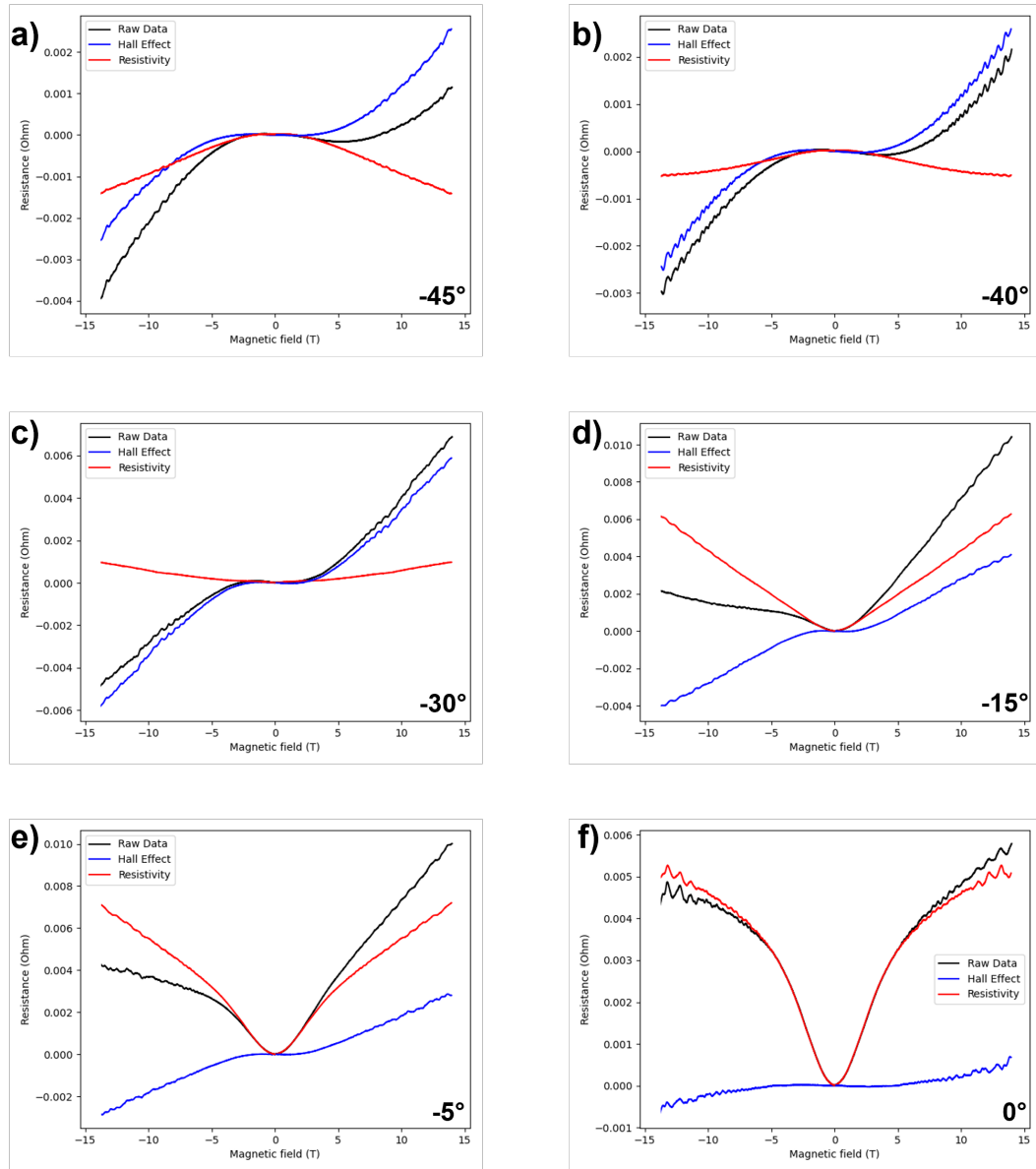## A.2 Raw Transport Measurement Results

FIGURE A.3: Resistance as a function of the magnetic field on NbP at various angles. **a)**In-plane measurements done at φ=-45° from the current. **b)**φ=-40° from the current. **c)**φ=-30° from the current. **d)**φ=-15° from the current. **e)**φ=-5° from the current. **f)**Measurements parallel to the current (φ=0).
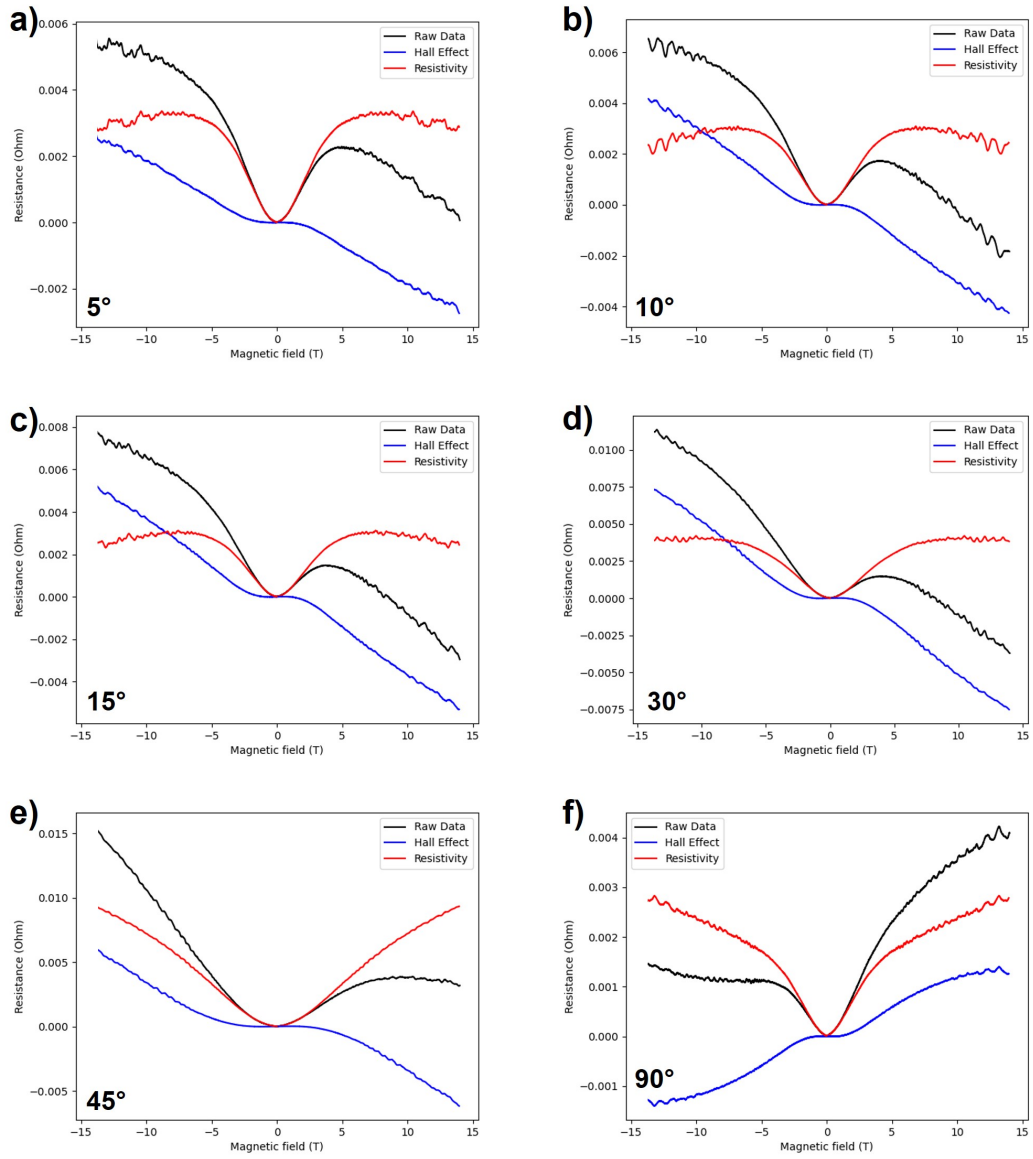
FIGURE A.4: Resistance as a function of the magnetic field on NbP at various angles. **a)**In-plane measurements done at $\varphi=5°$ from the current. **b)**$\varphi=10°$ from the current. **c)**$\varphi=15°$ from the current. **d)**$\varphi=30°$ from the current. **e)**$\varphi=45°$ from the current. **f)**Measurements perpendicular to the current($\varphi=90$).

FIGURE A.5: Resistance as a function of the magnetic field on NbP at various angles. **a)**Out-of-plane measurements done at Θ=0° from the current. **b)**Θ=5° from the current. **c)**Θ=15° from the current. **d)**Θ=30° from the current. **e)**Θ=45° from the current. **f)**Θ=60° from the current.
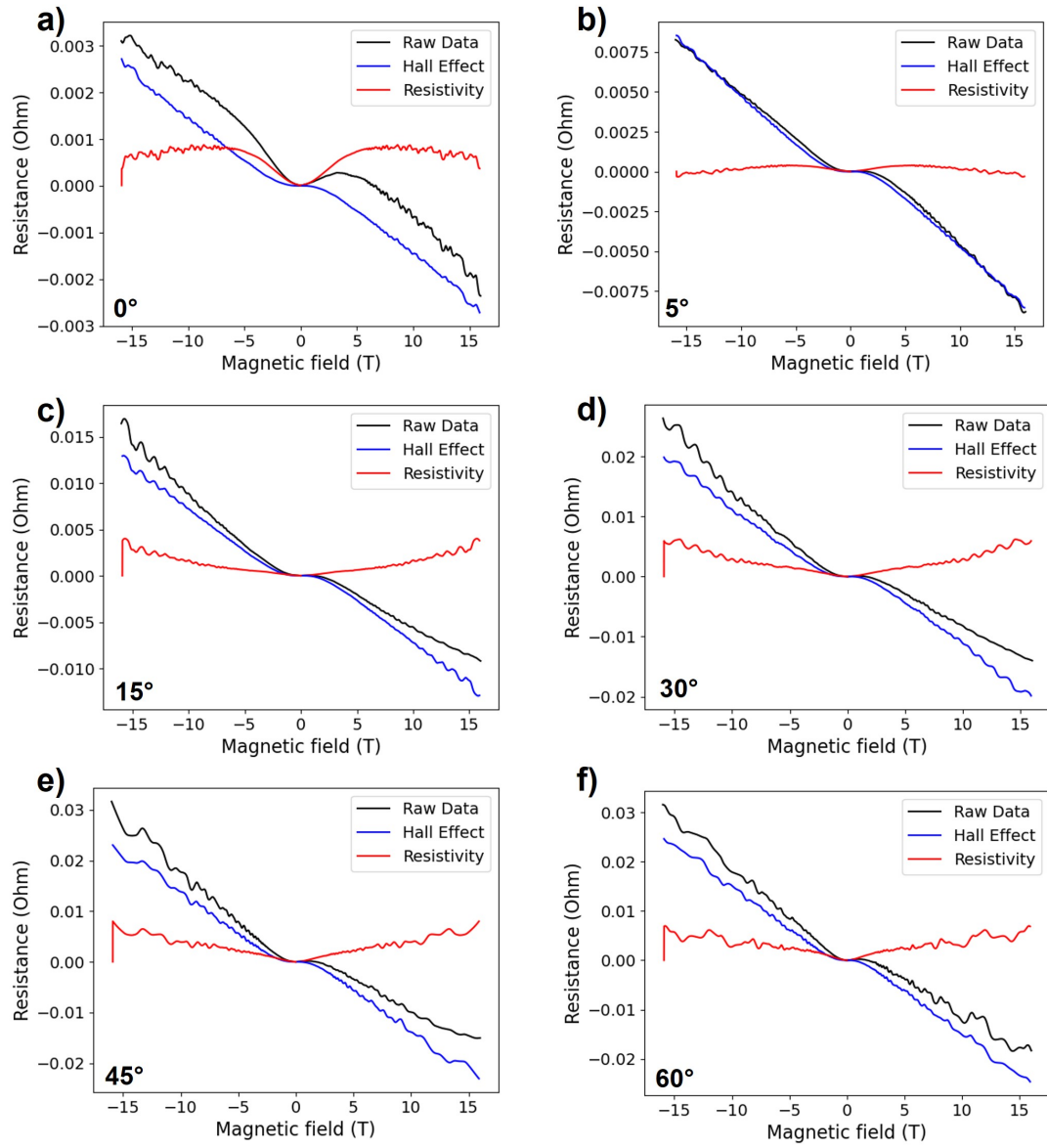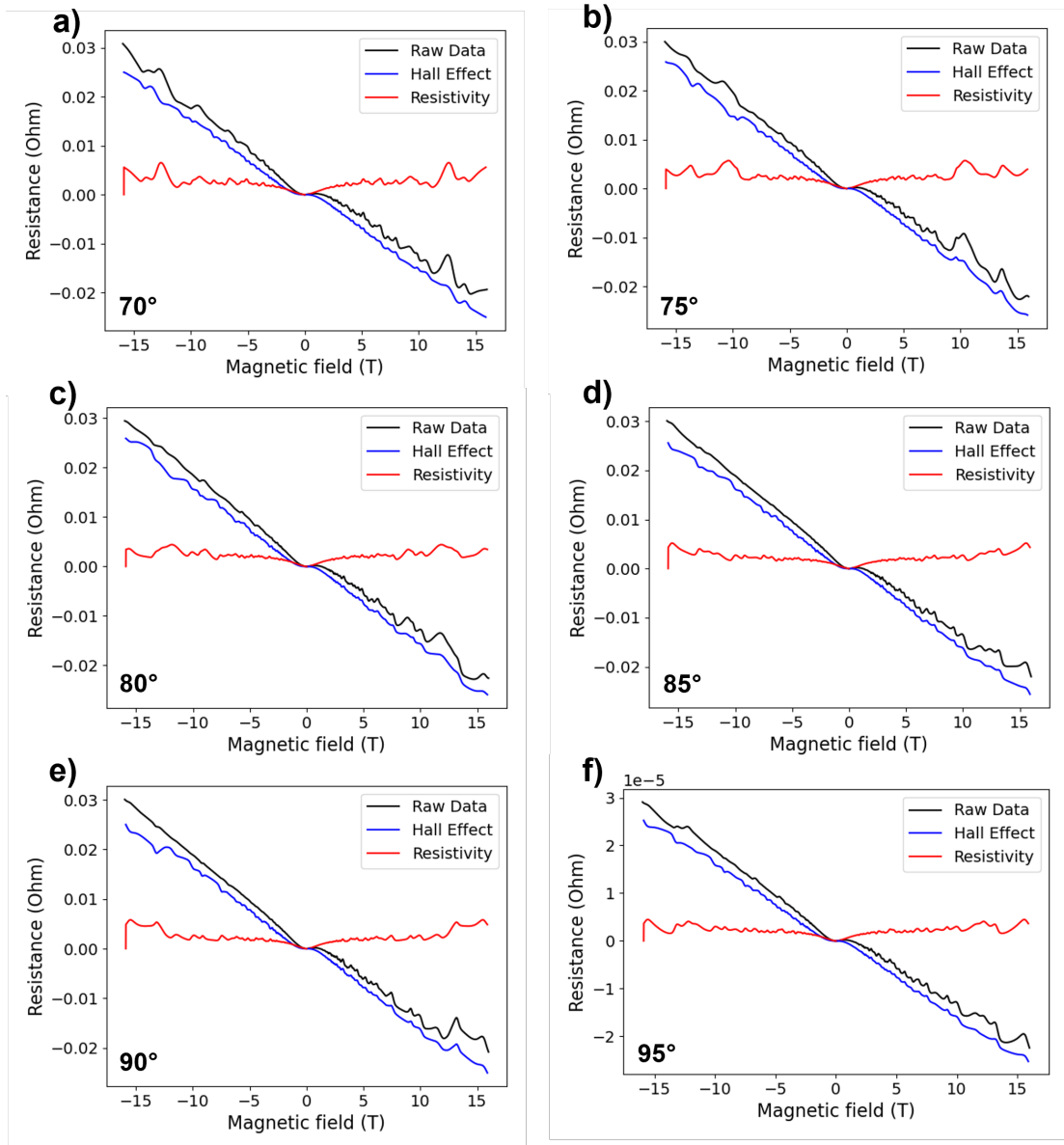
FIGURE A.6: Resistance as a function of the magnetic field on NbP at various angles. **a)**Out-of-plane measurements done at Θ=70° from the current. **b)**Θ=75° from the current. **c)**Θ=80° from the current. **d)**Θ=85° from the current. **e)**Θ=90° from the current. **f)**Θ=95° from the current.

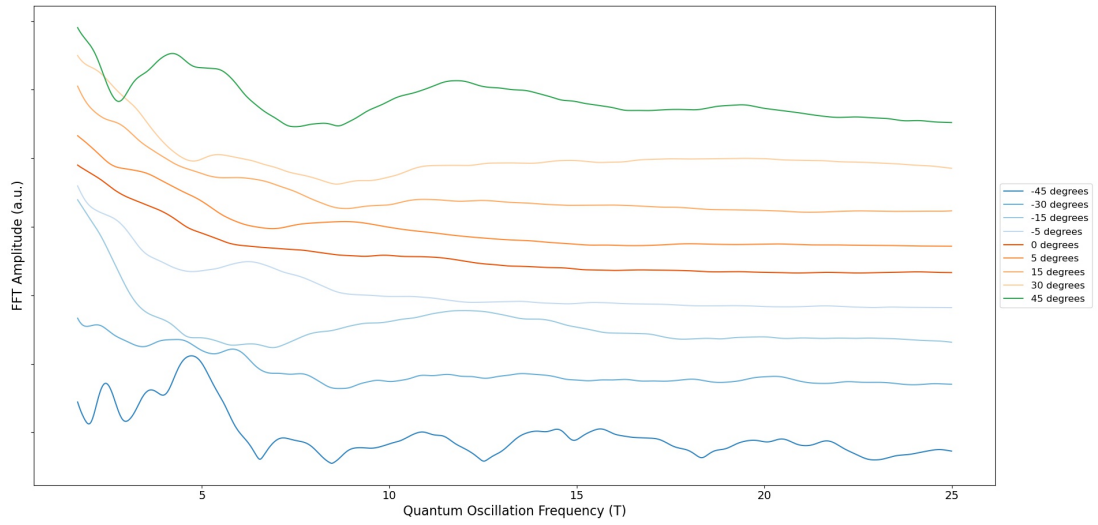## A.3 Lower Frequency Oscillations From Transport

FIGURE A.7: FFT of the in-plane transport measurements as a function of φ after a polynomial background subtraction at low oscillation frequencies.

Bibliography

[1] Tian, W., Yu, W., Shi, J., and Wang, Y. *Materials* **10**(7) (2017).

[2] Moore, J. E. *Nature* **464**(7286), 194–198 (2010).

[3] Krieger, J. A., Pertsova, A., Giblin, S. R., Döbeli, M., Prokscha, T., Schneider, C. W., Suter, A., Hesjedal, T., Balatsky, A. V., and Salman, Z. *Phys. Rev. Lett.* **125**, 026802 Jul (2020).

[4] Qi, Y., Naumov, P. G., Ali, M. N., Rajamathi, C. R., Schnelle, W., Barkalov, O., Hanfland, M., Wu, S.-C., Shekhar, C., Sun, Y., Süß, V., Schmidt, M., Schwarz, U., Pippel, E., Werner, P., Hillebrand, R., Förster, T., Kampert, E., Parkin, S., Cava, R. J., Felser, C., Yan, B., and Medvedev, S. A. *Nature Communications* **7**(1), 11038 (2016).

[5] Castelvecchi, D. *Nature* **547**(7663), 272–274 (2017).

[6] Yan, B. and Felser, C. *Annu. Rev. Condens. Matter Phys.* **8**(1), 337–354 March (2017).

[7] Moore, J. E. *IEEE Spectrum* **48**(7), 38–57 (2011).

[8] Weyl, H. *Proceedings of the National Academy of Sciences* **15**(4), 323–334 (1929).

[9] Burkov, A. A. *Annu. Rev. Condens. Matter Phys.* **9**(1), 359–378 March (2018).

[10] Rylands, C., Parhizkar, A., Burkov, A. A., and Galitski, V. *Phys. Rev. Lett.* **126**, 185303 May (2021).

[11] Yuan, X., Zhang, C., Zhang, Y., Yan, Z., Lyu, T., Zhang, M., Li, Z., Song, C., Zhao, M., Leng, P., Ozerov, M., Chen, X., Wang, N., Shi, Y., Yan, H., and Xiu, F. *Nature Communications* **11**(1), 1259 (2020).

[12] Zhang, C.-L., Xu, S.-Y., Belopolski, I., Yuan, Z., Lin, Z., Tong, B., Bian, G., Alidoust, N., Lee, C.-C., Huang, S.-M., Chang, T.-R., Chang, G., Hsu, C.-H., Jeng, H.-T., Neupane, M., Sanchez, D. S., Zheng, H., Wang, J., Lin, H., Zhang, C., Lu, H.-Z., Shen, S.-Q., Neupert, T., Zahid Hasan, M., and Jia, S. *Nature Communications* **7**(1), 10735 (2016).

[13] Kim, P., Ryoo, J. H., and Park, C.-H. *Phys. Rev. Lett.* **119**, 266401 Dec (2017).

[14] Son, D. T. and Spivak, B. Z. *PRB* **88**(10), 104412 September (2013).

[15] Arnold, F., Naumann, M., Wu, S.-C., Sun, Y., Schmidt, M., Borrmann, H., Felser, C., Yan, B., and Hassinger, E. *Phys. Rev. Lett.* **117**, 146401 Sep (2016).

[16] Lee, C.-C., Xu, S.-Y., Huang, S.-M., Sanchez, D. S., Belopolski, I., Chang, G., Bian, G., Alidoust, N., Zheng, H., Neupane, M., Wang, B., Bansil, A., Hasan, M. Z., and Lin, H. *PRB* **92**(23), 235104 December (2015).

[17] Grassano, D., Pulci, O., Mosca Conte, A., and Bechstedt, F. *Scientific Reports* **8**(1), 3534 (2018).

[18] Singleton, J., Bassani, F., Liedl, G. L., and Wyder, P. In *Encyclopedia of Condensed Matter Physics*, 343–355. Elsevier, Oxford (2005).

[19] Goerbig, M. O. (2009).

[20] Bernier, G. and Quilliam, J. *Protocole de travaux pratiques avancés, Université de Sherbrooke* .

[21] Luk'yanchuk, I. A. and Kopelevich, Y. *Phys. Rev. Lett.* **93**, 166402 Oct (2004).

[22] Shoenberg, D. D. *Magnetic oscillations in metals.* Cambridge monographs on physics. Cambridge University Press, Cambridge [Cambridgeshire] ;, (1984).

[23] Doiron-Leyraud, N., Szkopek, T., Pereg-Barnea, T., Proust, C., and Gervais, G. *Physical Review B* **91**(24) jun (2015).

[24] Mikitik, G. P. and Sharlai, Y. V. *Phys. Rev. Lett.* **82**, 2147–2150 Mar (1999).

[25] Zhang, Y., Tan, Y.-W., Stormer, H. L., and Kim, P. *Nature* **438**, 201–4 Nov (2005).

[26] Laliberté, F., Bélanger, F., Nair, N. L., Analytis, J. G., Boulanger, M.-E., Dion, M., Taillefer, L., and Quilliam, J. A. *Phys. Rev. B* **102**, 125104 Sep (2020).

[27] Sergelius, P., Gooth, J., Bäßler, S., Zierold, R., Wiegand, C., Niemann, A., Reith, H., Shekhar, C., Felser, C., Yan, B., and Nielsch, K. *Scientific Reports* **6**(1), 33859 (2016).

[28] Klotz, J., Wu, S.-C., Shekhar, C., Sun, Y., Schmidt, M., Nicklas, M., Baenitz, M., Uhlarz, M., Wosnitza, J., Felser, C., and Yan, B. *Phys. Rev. B* **93**, 121105 Mar (2016).

[29] Wang, Z., Zheng, Y., Shen, Z., Lu, Y., Fang, H., Sheng, F., Zhou, Y., Yang, X., Li, Y., Feng, C., and Xu, Z.-A. *PRB* **93**(12), 121112 March (2016).

[30] Sudesh, Kumar, P., Neha, P., Das, T., and Patnaik, S. *Scientific Reports* **7**(1), 46062 (2017).

[31] Potter, A. C., Kimchi, I., and Vishwanath, A. *Nature Communications* **5**(1), 5161 (2014).

[32] Nair, N. L., Boulanger, M.-E., Laliberté, F., Griffin, S., Channa, S., Legros, A., Tabis, W., Proust, C., Neaton, J., Taillefer, L., and Analytis, J. G. *Phys. Rev. B* **102**, 075402 Aug (2020).

[33] Luthi, B. B. *Physical acoustics in the solid state.* Springer series in solid-state sciences, 148. Springer, Berlin, 2nd printing of the 1st ed. edition, (2007).

[34] Royer, D. and Dieulesaint, E. *Elastic waves in solids.* Advanced texts in physics. Springer, Berlin ;, (2000).

[35] Jaeken, J. W. and Cottenier, S. *Computer Physics Communications* **207**, 445–451 (2016).

[36] Leisure, R. G. *Ultrasonic Spectroscopy: Applications in Condensed Matter Physics and Materials Science.* Cambridge University Press, Cambridge, (2017).

[37] Hirschberger, M., Kushwaha, S., Wang, Z., Gibson, Q., Liang, S., Belvin, C. A., Bernevig, B. A., Cava, R. J., and Ong, N. P. *Nature materials* **15**, 1161–1165 Nov (2016).

[38] Huang, X., Zhao, L., Long, Y., Wang, P., Chen, D., Yang, Z., Liang, H., Xue, M., Weng, H., Fang, Z., Dai, X., and Chen, G. *Phys. Rev. X* **5**, 031023 Aug (2015).

[39] Niemann, A. C., Gooth, J., Wu, S.-C., Bäßler, S., Sergelius, P., Hühne, R., Rellinghaus, B., Shekhar, C., Süß, V., Schmidt, M., Felser, C., Yan, B., and Nielsch, K. *Scientific Reports* **7**(1), 43394 (2017).

[40] Arnold, F., Shekhar, C., Wu, S.-C., Sun, Y., dos Reis, R. D., Kumar, N., Naumann, M., Ajeesh, M. O., Schmidt, M., Grushin, A. G., Bardarson, J. H., Baenitz, M., Sokolov, D., Borrmann, H., Nicklas, M., Felser, C., Hassinger, E., and Yan, B. *Nature Communications* **7**(1), 11615 (2016).

[41] dos Reis, R. D., Ajeesh, M. O., Kumar, N., Arnold, F., Shekhar, C., Naumann, M., Schmidt, M., Nicklas, M., and Hassinger, E. *New Journal of Physics* **18**(8), 085006 aug (2016).

[42] Ramshaw, B. J., Modic, K. A., Shekhter, A., Zhang, Y., Kim, E.-A., Moll, P. J. W., Bachmann, M. D., Chan, M. K., Betts, J. B., Balakirev, F., Migliori, A., Ghimire, N. J., Bauer, E. D., Ronning, F., and McDonald, R. D. *Nature Communications* **9**(1), 2217 (2018).

[43] Rinkel, P., Lopes, P. L. S., and Garate, I. *Phys. Rev. B* **99**, 144301 Apr (2019).

[44] Hutson, A. R. and White, D. L. *Journal of Applied Physics* **33**(1), 40–47 January (1962).

[45] Pobell, F. and Pobell, F. In *Matter and Methods at Low Temperatures*, 115–138. Springer Berlin Heidelberg, Berlin, Heidelberg (2007).

[46] Liu, L., Wang, Z.-Q., Hu, C.-E., Cheng, Y., and Ji, G.-F. *Solid State Communications* **263**, 10–18 (2017).

[47] Schindler, C., Gorbunov, D., Zherlitsyn, S., Galeski, S., Schmidt, M., Wosnitza, J., and Gooth, J. *Phys. Rev. B* **102**, 165156 Oct (2020).

[48] QuantumDesign. *PPMS Platform Measurement Options*.

[49] Reis, R. D. d., Ajeesh, M. O., Kumar, N., Arnold, F., Shekhar, C., Naumann, M., Schmidt, M., Nicklas, M., and Hassinger, E. *New journal of physics* **18**(8), 85006– (2016).